Research on fatigue damage and dilatancy properties for salt rock under discontinuous cyclic loading

Jinyang Fan

To cite this version:

Jinyang Fan. Research on fatigue damage and dilatancy properties for salt rock under discontinuous cyclic loading. Earth Sciences. Université Côte d'Azur, 2017. English. NNT : 2017AZUR4030 . tel-01674225v1

HAL Id: tel-01674225
https://theses.hal.science/tel-01674225v1

Submitted on 2 Jan 2018 (v1), last revised 2 Jan 2018 (v2)

L'école doctorale en ED SFA
Doctorat sciences de la planete et de l'univers

Thèse de doctorat

Présentée en vue de l'obtention du
grade de docteur en Discipline
de
l'UNIVERSITE COTE D'AZUR

par

Jinyang FAN

Research on fatigue damage and dilatancy properties for salt rock under discontinuous cyclic loading

Dirigée par Prof Alexandre Chemenda
Prof Deyi Jiang

Soutenue le 19 May 2017
Devant le jury composé de : « *par ordre alphabétique des membres* »

Alexandre	Chemenda	Professor	University of Nice-Sophia Antipolis	Directeur de thèse
Lei	Zhou	Professor	Chongqing University	Examinateur
Xiaoming	Sun	Professor	China University of Mining & Technology	Rapporteur
Yang	Ju	Professor	China University of Mining & Technology	Président du jury
Yuanxue	Liu	Professor	Logistic Engineering University	Rapporteur

ABSTRACT

Non-occupied underground salt caverns resulting from production of salt induce a number of environment and surface safety problems. With such properties as low permeability and rheological behavior as well as the ability of self-healing for cracks, they could be used as ideal safe and stable store sites for gas or liquid hydrocarbon resource (such as natural gas, oil, compressed air). Since the salt storage caverns of natural gas or compressed air play a critical role in ensuring the energy supply and adjusting the seasonal imbalance, China government has been constructing many new storage caverns in recent years.

According to the variations of the energy market demand, the stored natural gas or compressed air are released at peak demand and stored (added) at low demand. Consequently, the pressure inside the storages changes cyclically with the market demand. Under the repeated loading/unloading effect, the storage volume progressively shrinks with the evolution of fatigue damage caused by cyclic loading. As the fatigue damage accumulates, the volume loss of storage increases. Moreover, the mechanical instability or gas leakage may occur. Therefore, the investigation of the fatigue of salt under cyclic loading is of great importance to the safe operation of underground salt caverns storages.

Considering the specific characteristics of salt formation (including the burial depth, thickness, ground temperature, etc.), we perform the uniaxial, triaxial, cyclic continuous and discontinuous loading tests in order to investigate the salt mechanical response and the related damage mechanisms defining relation between plastic deformation, dilatancy and damage. Based on this, we constrain a constitutive model for future numerical experimentation.

More specifically the thesis addresses the following issues:

① Definition of the basic mechanical parameters, the uniaxial compression strength and the elastic moduli from uniaxial compression tests. Constraining the evolution of inelastic deformation and damage from uniaxial and triaxial tests. Development of the constitutive relationships for salt rock under monotonic continuous loading.

② Design and performing of the conventional fatigue tests on salt with various upper and lower stress limits, temperature, and loading rate, considering the geological conditions, underground temperature and the speed of gas filling/recovery.

③ Development of a fatigue life model to interpret the ability of salt to endure the cyclic loading-unloading. During the cyclic loading-unloading, salt was shown to significantly harden (strengthen). Constitutive model is developed for the fatigue behavior of salt with the yield surface evolving with the inelastic deformation .

④ The loading intervals were shown to strongly affect the fatigue properties of salt. A series of discontinuous fatigue tests were carried out based on the practical data from a running storage. The coupled effect of ratcheting and intervals was studied.

⑤ The salt plastic flow and dilatancy were addressed from the perspective of dislocation theory and fracture mechanics by introducing the weakening parameter to describe the periodic change of the yield surface during the loading intervals. A new constitutive relationship for salt rock under discontinuous cyclic loading has been developed.

Keywords: salt rock, rock testing, rock mechanics, discontinuous fatigue, gas storage, constitutive behavior, plastic flow

Category

1 Introduction

1.1 Research Background

1.1.1 Mass construction of underground salt cavern storages

Underground salt caverns, as ideal energy (crude oil, natural gas etc.) storage place, have favorable impermeability and economic efficiency benefited from the method of water dissolving (Fig 1.1) [1-4]. Many developed countries (such as, US, Japan, UK, France, German) have built their national storage systems of strategic energy in recent 20 years [5,6]. In China, a crude oil external dependence exceeded 60% in 2016, as reported from the data by China's national bureau of statistics in end of last year. The objective of China crude oil strategic reservation being built is to satisfy 100 days consumption demand. According to the IEA (international energy agency) suggestion that the amount of oil strategic reservation is roughly equivalent to 90 days imports, China need to reserve 540~600 million barrels of crude oil. However, China's reserved oil only could sustain 29 days in 2015. In the near feature, China will build massive oil storages.

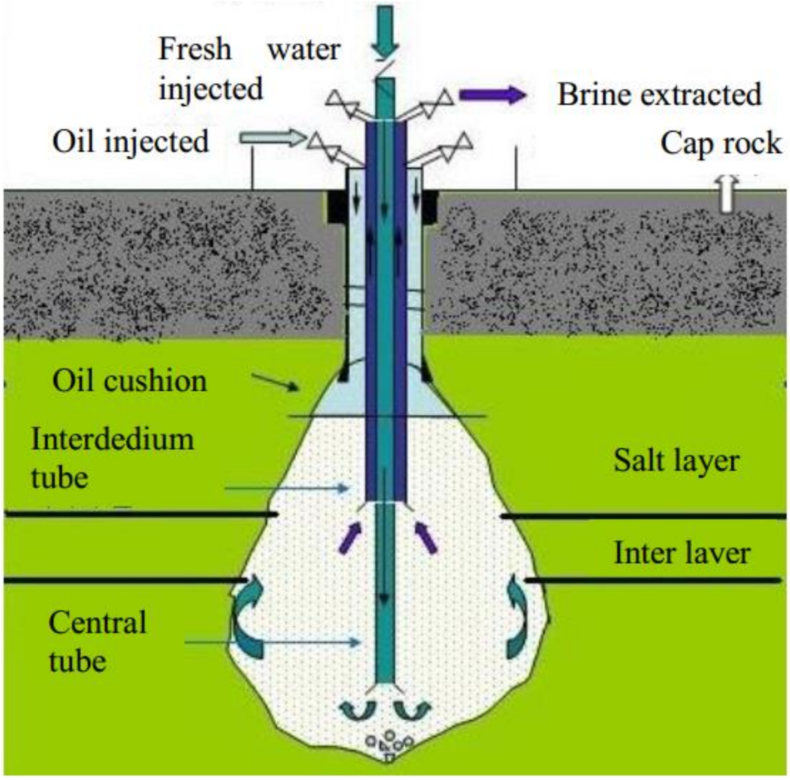

Fig.1.1 Salt rock cavity water dissolving mining schematic

There are 630 underground natural gas storages in operation, having 358.8 billion cubic meters of service capacity, especially in North America, Russia, Europe and Ukraine, where the natural gas market is relatively mature. So far, US owns 419 underground gas storage (around 60% of quantity of global operating underground gas storages) capable of supplying 1.2×10^{11} cubic meters of gas (around 33% of global gas amount, which could support 20 years consumption of gas). The gas volume of underground natural gas storage amounts to 10.3% of global consumption of natural gas by 2015. Predictablly, the demand for gas in China will reach 4.5 trillion cubic meters.

2015 China's gas production is 135 billion cubic metres, an increase of 5.6%; import is 61.4 billion cubic meters, a rise of 6.3%; consumption is 193.2 billion cubic meters, a growth of 5.7%. Gas external dependence soars to 32.3% from 2.0% in 2007 (see Fig. 1.2). Operational capacity of underground gas storage by far is unable to match the present consumption. The peak load regulating capacity of storages that have been already built only amounts to 1.7% of annual consumption, unpleasurable for the peak demand of gas in winter. The gas imports and external dependence are expected to reach 180 billion cubic meters, 40%, respectively, by 2030. According to the western developed country's experience, once the dependence exceeds 30%, the peak load regulating capacity must achieve 12% of annual consumption; once the dependence exceeds 50%, the peak load regulating capacity must achieve 15% of annual consumption, to make sure the correct balance of energy supply。

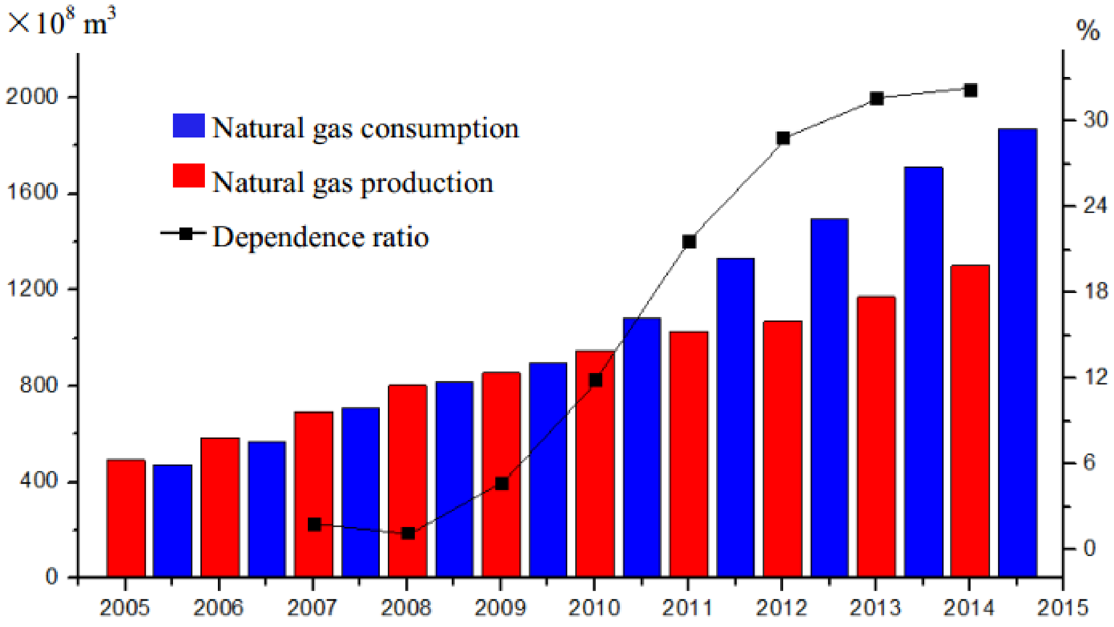

Fig.1.2 China natrual gas production, consumption and dependence ratio from 2005 to 2014

China’s supply ability for natural gas as a whole is sufficient, even redundant. Influenced by seasonal imbalance, gas supply has to suffer from the discrepancy between production compression at off season and short supply at peak season, because of the insufficiency of regulating capacity of gas storages. Underground salt cavern gas storage, flexible and capacious (high throughput) for production and injection, has been widely accepted by Europe and America. Therefore, in current strategy, China plan further construction of underground salt cavern storages to ensure the safety of energy supply and steady sustainable development of economy.

1.1.2 Compressed air energy storage(CAES)in the ascendant

CAES power plant construction is a good approach for comprehensive utilization of underground salt caverns [7,8]. On 28th Feb 2017, China smart grid demonstrative project of underground salt cavern CAES has passed through the technological verification, indicating that the CAES plant comes into a new stage in China. At present, the mismatch between the load regulation ability of State Grid Corporation of China and the development speed of renewable energy results in a massive waste of energy [9-12]. Since 2008, wind power generation develop strikingly, whose scale has reached an unprecedented state. However, wind power resource is rather unstable, difficult to be accepted by National Grid, which mainly runs with coal power in past decades. Fig. 1.3 shows the problem on the mismatch between the wind power distribution and market demand. Combined with the shortage of needful energy storage measures, the mismatch brings in the phenomenon of “Abandon the wind power brownouts” and this phenomenon is going worse [13]. 1.5 billion kW • h of wind power in 2011 was abandoned, equivalent to 12% of total wind power; 20.8 billion kW • h of wind power in 2012, equivalent to 20% of total wind power.

In order to improve the ability of grid in regulation and acceptance, developing the energy storage technology of high efficiency and large capacity should not only help to make full use of the imbalance wind and solar power, but also greatly improve the quality of power supply and echo the world supported policy of energy safety and energy conservation as well as emission reduction. In China’s Twelfth Five development strategy planning, energy storage development is one of the important directions. Underground salt cavern CAES technology will be the one caught more attention in electricity industry [14-16].

As a new energy storage technology, CAES is characterized by a low environmental pollution, speed dynamic response and high economy [14, 15]. CAES power plant uses redundant electricity to compresses air into underground cavern, storing air energy at low peak demand; At peak demand the compressed air is released, mixed with fuel gas and burn to generate electricity (Fig 1.4).

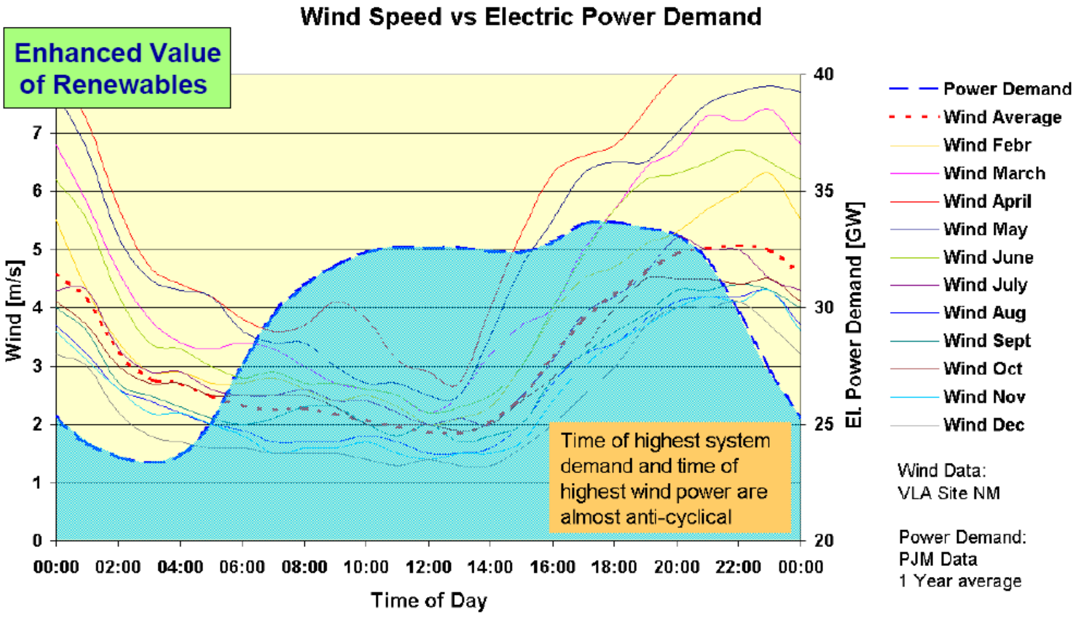

Fig. 1.3 Variation of wind resource and power demand in one day

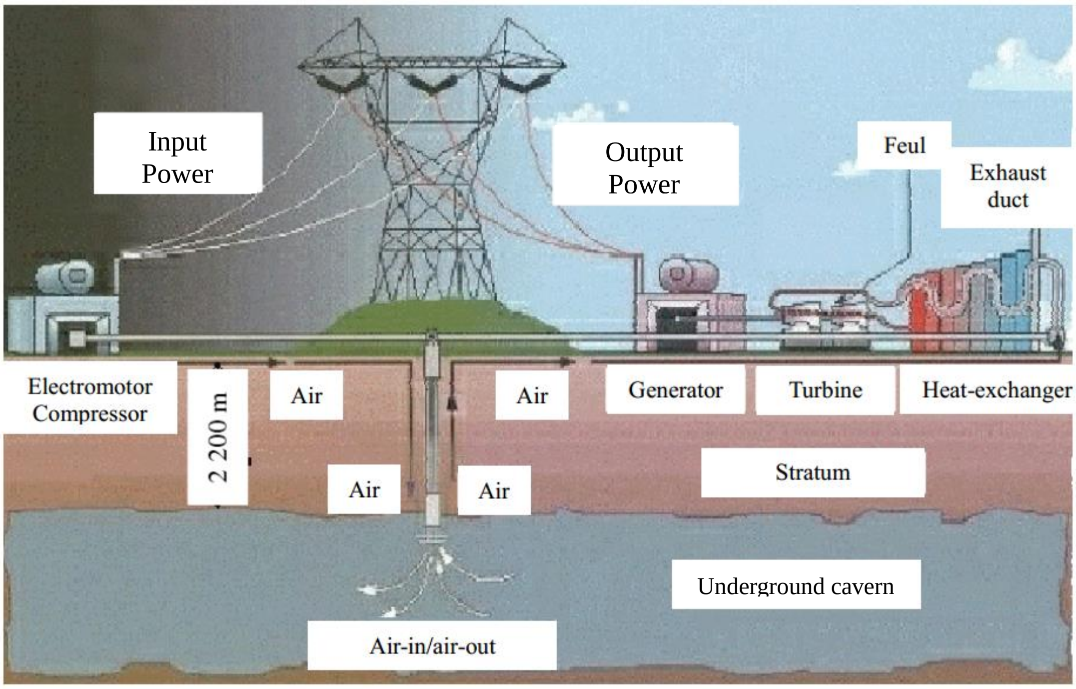

Fig.1.4 Sketch map of compressed air energy storage power generation

Normally, underground salt cavern or aquifer would serve as the airtight, stable and safe storage space for a CAES power plant [18]. Germany built the first CAES plant [19] (Fig. 1.5), Huntorf plant, whose power output is 290 MW. The energy storage chamber is an underground salt cavern, which afterwards was rebuilt to expand to 0.003 km^3 and served to supply fuel for gas turbine. Its thermal efficacy can reach 86%. The plant completes one cycle every day, charging 8 hours and discharging 2 hours. As the first CAES plant, Huntorf plant has gone through 20 years, during which there are around 7 times of thousand startups with the reliability more than 98%. The experience shows that the underground salt cavern CAES plant is viable, stable and reliable at operation. Japan, Italy, Russia, Israel and other countries, develop the research, trail, construction and application of CAES [20].

Fig.1.5 Huntorf CAES power plant in Germany

In a word, CAES owning such properties as geographical applicability and low demand for water is suitable for the drought but resourceful area, for example China Three North (North China, Northwest China and Northeast China). Wind, solar renewable resources are plentiful in China Three North area. CAES technology is the optimum way to exploit clean energy, reduce environmental pollution and develop smart power grid. However, CAES plants undergo discontinuous cyclic loading [21-24].

1.1.3 Effect of cyclic loading on engineering

The phenomenon that materials under cyclic load below the ultimate strength generate damage, initiate crack and progressively approach failure after the damage accumulates and cracks grow to some degree, is termed as fatigue. The maximum stress below which the material is able to endure an infinite amount of stress cycles is defined as fatigue strength or fatigue limit [14, 25]. Since in practice the number of cycles cannot be infinite, for nonferrous metal materials the maximal stress below which the materials is able to undergo 10^8 stress cycles without any apparent fracture is conventionally called the fatigue strength[26]. Statistic data shows that more than 80% failures of mechanical component are related to fatigue. No obvious deformation is usually detected before fatigue failure, thus inconspicuous and easy to cause tremendous accidents. Mechanism of fatigue fracture is different from the conventional failure forming in uniaxial or triaxial tests, is extremely complex, therefore, fatigue research is now one of hot topics in the engineering field.

Although there is no similar definition for geomaterials, cyclic load is always present in geo engineering-related situations and exerts influence on the stability and safety [27-31]. For example, the work face in underground mine incurs periodic weighting, the road and bridge bear the repeated traffic load and pedestrian load, the water level of dam always repeatedly rises and falls, side slope withstands the change in temperature (cycle of freezing and thawing), underground salt cavern storages and CAES operates with the cycles of production and injection. Therefore, the research of the fatigue properties of geomaterials is necessary

1.2 Research status of rock fatigue

Fatigue phenomenon was discovered in 1829, when German engineer Albert was studying the strength of hinge of winch. After that, the fatigue of materials became a subject of intense studies. Owing to the technological restriction, the earlier research was based on the experimentation and phenomenological theories used to describe experimental results and exploring the fatigue properties under different stress conditions, strain rate and temperature.

Until the start of 20th century, people gradually realized that the fatigue of a material can be caused by the dislocations that could cause the crack imitation and growth. In 1950~1960s, based on the research on crystallology, dislocation theory was put forward and promoted the fatigue research development towards the microcosmic field [32-36]. Invention of scanning electron microscope (SEM) and transmission electron microscope allowed revealing the micro-mechanisms of fatigue and associated fatigue damage. The fatigue damage in the materials is controlled by plastic deformation, which results in the irreversible change of material structure, always associated with the evolution of dislocation [37, 38]. Usually the crack nucleation occurs at the earlier stages of fatigue: the extrusions and invasions of molecular layers on the surface of mental crystals easily create the stress concentration, which could cause fatigue cracks. High-angle crystal boundaries in metal multicrystals could generate pile-up effect on dislocations within glide band. Manifold cyclic deformations intensify the stress concentration; thereby the fatigue cracks initiate and grow along the high-angle crystal boundary. Impurities and second phase particle are also contribute to deformation and fatigue crack during repeated cyclic deformation [39-44]. As the new methods develop and research goes deep, metal fatigue researches have been paving a broad road for fatigue research.

Fatigue research of geometrical started later. In this domain, due to the extensive application, concrete fatigue was studied relatively earlier [45-47]. In 1898, Considere and Dejoly started the fatigue research on mortar concrete. With the recent rapid development of traffic, transport, water conservancy and airline industry, concrete engineering has been intensively developed. At the same time the possibility of failure of concrete member were rising, attracting a great attention from international researchers [48]. Natural rocks, although having similarities in anisotropy, heterogeneity and discontinuity with concretes, have experienced complex tectonic loading and transformations during geological history and formed a large number of different sort of discontinues such as microfractures, grain boundaries, stratification with weak intercalated layer etc. This causes serious difficulties in describing the fatigue properties and explaining the fatigue mechanism in geomaterials. In spite of this, considerable progresses have been made in rock fatigue domain.

1.2.1 Research status of fatigue strength

Grover Dehlinger and McClure (1950) performed the first rock fatigue test. In 1963, Burdine discovered that the fatigue life of Berea sandstone could reach 1 million with the upper stress limit of 74% of compression strength. Haimson [34] compared two different marble, discovering when the upper stress limit is set at 50% of compression strength, Geogia marle could undergo 1 million cycles; Tennessee marble have the same life only if the upper stress limit is 75% of compression strength. The fatigue experiments revealed strain softening of rocks during cyclic loading, with the elasticity modulus decreasing with the stress cycles. Bagde and Petroš[49] studied the fatigue strength and dynamic axial stiffness of carbide sandstone. The results showed that the increase in the loading frequency and the stress amplitude could reduce both the fatigue strength and dynamic axial stiffness.

It has been shown that the dynamic fatigue strength depends on the quartz content, structure and texture of rock. The loading conditions effect rock's dynamic strength; the size and distribution of microcracks effect the fatigue failure and physical properties; average Young's modulus increases with the diminishing loading amplitude and frequency; The fatigue indexes (fatigue life and fatigue strength) of wet sandstones are smaller than those of dry sandstones. Singh[50] conducted the fatigue strength test on Graywacke to find out the relationship of particle size, compression strength and fatigue strength. The results showed that the both compression and fatigue strengths of sandstone increase with smaller with the reduction of the grain size. When the grain size decreases from 1.79mm, 1.35mm to 0.93mm, the fatigue strength rises from 87%, 88.25% to 89.1% of the initial strength of intact Graywacke. But the fatigue strength and the average compression strength showed the reverse tendency.

1.2.2 Research status of fatigue life

Singh[51] studied the strain hardening and fatigue properties of Australia greywacke. The results showed rock that the fatigue life increases logarithmically with the stress amplitude reduction; as the maximum stress keep constant, fatigue lives of the rock could go in the increase tendency with stress amplitude, loading rate and hardening rate. Ren Song et al[52] studied the Pakistan rock salt under different confining pressure and proposed an empirical model. Momeno et al[53] studied the influence of fatigue(cyclic) loading on the mechanical behavior of granite. They discovered that the fatigue life grows with increasing loading rate and decreasing maximal stress.

You-Liang Chen[54] conducted fatigue tests under different temperature. The temperature variation below 400℃ does not make any notable difference in fatigue life. The fatigue life decreases with temperature above 400℃. Hamid Reza Nejati and Abdolhadi Ghazvinian[55] conducted cyclic loading tests on three types of rock with different brittleness (onyx marble, sandstone, soft limestone). They have shown that the fatigue life of brittle rock (onyx marble) is lower than that of semi-brittle rock (sandstone) and soft rock (limestone). The fracture surface forming in dynamic loading is rougher.

1.2.3 Research status of fatigue crack and fatigue damage

Maria Migliazzaet et al. [56-58] determined the propagating mode, tensile strength, breaking tenacity and crack growth rate of Carara marble in three- and four-point bending test to evaluate the parameters of Paris model for marble mosaic plate. Jia-Liang Le et al [59] studied scale effect on dynamic fatigue properties of Berea sandstone and discovered that the fracture progress band under cyclic loading was broader than that under continuous loading. These authors proposed a new crack growth model by modifying Paris-Erdogan model. Yi Liu et al [60] studied the fracture mechanism for discontinuous joint rock under cyclic loading effect. Joint inclination, strength and porosity could exert significant influence on the dynamic fatigue properties. All the three fracture modes (splitting, shearing and hybrid) are related to the joint geometry. The difference lies in the number of fracture zones and the scale of stress.

Erarslan and Williams[61, 62] discovered that the fatigue damage can reduce rock’s fracture toughness in Brisbane tuff fatigue tests. Step fatigue loading can reduce fracture toughness by 46%; sine wave fatigue loading could reduce 29%. Fatigue damage in rocks was caused by decohesion of inner particle and trans-granular crack. Jianqing Xiao et al[63] studied rock fatigue damage model and proposed an “inverse S” model. Zhechao Wang et al[64, 65] divided fatigue behavior of granite into three phases (compression phase, dilatancy phase and strain softening phase). They thought of the fatigue strength as the demarcation point of compression and dilatancy. Moreover, after rock unloads from dilatancy zone to compression zone, there still exists fatigue phenomenon. N. Gatelier et al[66] conducted fatigue tests on porous sandstone along different principal stress direction to figure out the damage evolution before peak. At lower confining pressure, damage development was decided by pressure configuration and microcracks and showed prodigious difference because of the loading direction. At higher confining pressure, anisotropy is negligible.

Underground water level changes seasonally, causing the pore pressure to rise and to fall. Giona Preisig et al[67, 68] combined numerical simulation and field inspection in studying the Campo Vallemaggia landslide in terms of fatigue damage. Original internal permeable weak plane played a pivotal role. Through relative sliding along the natural fracture walls, rock bridges gradually became weak and local fatigue damage formed. Xuedong Luo et al[69] studied mechanical properties of granulite subjected to frequent

SHPB impacts. After several impacts, peak strain become larger, the velocity of longitudinal wave passing through the sample dropped. Mathieu Preteseille and Thomas Lenoir [70-75] studied the mechanical properties of lime and cement stable materials under fatigue loading as a reference for road traffic engineering. Aleksandr S. Voznesenskii et al[76-78] studied the effect of stress state and scale effect on rock (plaster, salt) acoustic signals and residual strength after fatigue loading. They established the method of predicting the residual strength using acoustic data.

1.3 Research status of rock fatigue constitutive model

Constitutive relations are developed to mathematically describe the macroscopic properties. To solve the boundary value problem, the initial and boundary conditions should be used along with the constitutive equations. Initial and boundary conditions are usually fixed. Therefore, establishing an accurate constitutive equation is a key to correctly solve the mechanical problem.

Characteristic large number of constitutive models has been proposed. Based on the fracture mechanics theory Giang D. Nguyen et al[79] developed a constitutive model, where the orientation and scale of shear compaction band were taken into account. X.S. Liu et al [80] introduced a compaction coefficient in a damage constitutive model, based on energy dissipation theory. During each cycle, the mechanical properties are changed to simulate the rock fatigue behavior. Angelo Amorosi et al [81] proposed a new constitutive model based on critical condition and used it to analyze the mechanical response of Naples yellow tuff in situ plate load test. The results showed that this model can accurately describe the plastic deformation caused by material degradation and isotropic strengthening.

Mas and Chemenda[82-84] found a relation between the internal friction and dilatancy coefficients and applied it in the their constitutive model for a wide range of confining pressure corresponding from brittleness to ductile rock behavior. Omid Pourhosseini and Mahdi Shabanimashcool et al[85] established a plastic potential function based on dilatancy angle to describe the elastoplastic behavior in static loading mode. After the peak, the yield surface gradually shrinks. The friction angle is constant, while the dilatancy angle is the function of the confining pressure, the friction angle and compressive strength. Maria Teresa Zandarin et al[86] developed a constitutive model for jointed rocks, considering suction effect and joint roughness. They studied the relation between shear strength, dilatancy, suction effect and roughness, finding that the joint degraded with the loading work in shear test.

H.W. Zhou et al[87] replaced the Newton's original by Abel dashpot in Nishihara model, establishing a creep constitutive model that includes time-dependent frictional derivatives. The higher the order of frictional derivatives, the higher the plastic strain rate and the lesser the proportion of stable creep in plastic strain. As the order is 1, the constitutive model is reduced to the Nishihara model. V. Navarro et al[88] developed a constitutive model to describe the mechanical response of porous rocks. This model takes into account the weakening effect of skeleton and capillary effect in unsaturated state. C.Y. Zhou and F.X. Zhu[89] established double yield surface elastoplasticity damage model for saturated soft rock, in which the damage variable is used to represent the evolution of micro-cracking.

Combined visco-plasticity consistency model of compression tests and anisotropy viscoplasticity consistency model of extension test, Timo Saksala and Adnan Ibrahimbegovic[90] developed a constitutive model to describe the transition from brittle to ductile deformation regimes. G. Grasselli and P. Egger[91] studied the direct shear test of 7 different jointed rocks and proposed a constitutive model. M.C. Weng et al[92-95] proposed an elastic-visco-plastic constitutive model to describe the rock dilatancy. Based on J integral, Zhennan Zhang and Kai Huang[96] established a double linear constitutive model to simulate the cracking in quasi-brittle rocks.

1.3.1 Strain softening model

For the ideal elastoplasticity model, the stress after yield is constant, while in reality, strain hardening or softening occurs. Omid Pourhosseini et al[85] introduced a softening coefficient η to represent the degradation of the rock strength after yield.

$$F\left(\sigma_{ij},\eta\right)=0 \tag{1.1}$$

F is yield function; σ_{ij} is stress tensor. In Mohr–Coulomb (MC) criterion, softening coefficient representing the cohension c reduces. It is usually believed that the friction coefficient is constant in some models. Thus,

$$f=\sigma_1-\frac{2c(\eta)cos\emptyset}{1-sin\emptyset}-\sigma_3\frac{1+sin\emptyset}{1-sin\emptyset} \tag{1.2}$$

η was defined as a function of the increment of plastic shear strain,

$$\eta=\gamma^p=\varepsilon_1^p-\varepsilon_3^p \tag{1.3}$$

And $\dot{\eta}=\frac{\partial\eta}{\partial t}$

In Flac3D code，the increment of plastic shear deformation $\Delta\varepsilon^{ps}$ is used to describe the isotropical softening.

$$\Delta\varepsilon^{ps}=\frac{1}{\sqrt{2}}\sqrt{\dot{\varepsilon}_1^p\dot{\varepsilon}_1^p+\dot{\varepsilon}_2^p\dot{\varepsilon}_2^p+\dot{\varepsilon}_3^p\dot{\varepsilon}_3^p} \tag{1.4}$$

Plastic strain rate is obtained from plastic potential $g(\sigma_{ij},\eta)$,

$$\dot{\varepsilon}_{ij}=\lambda\frac{\partial g}{\partial\sigma_{ij}} \tag{1.5}$$

It is typically assumed that the plastic potential is a function of the dilatancy angle

$$g=\sigma_1-\sigma_3 tan\varphi \tag{1.6}$$

The dilatancy reaches maximum at the peak of stress and then gradually reduces with the plastic strain。

$$g=\sigma_1-\sigma_3 tan[\varphi(\eta,\sigma_3)] \tag{1.7}$$

In the plastic domain, stress tensor obeys the consistency condition, $\mathrm{d}f=\frac{\partial f}{\partial\sigma}\mathrm{d}\sigma=0$, using which plastic factor λ can obtain

$$\lambda=\frac{1}{h}\frac{\partial f}{\partial\sigma}\dot{\sigma} \tag{1.8}$$

$$h=-\frac{1}{\sqrt{3}}\sqrt{(1+sin\emptyset)sin\varphi}\frac{\partial f}{\partial\eta} \tag{1.9}$$

Where *h* is hardening parameter.

1.3.2 Damage model based on energy dissipation theory

When rock undergoes a fatigue damage, the stress-strain curve in each cycle is different. X.S. Liu et al[80] defined damage variable *D* based on energy dissipation approach.

$$D=\frac{U^d}{U} \tag{1.10}$$

where U is total energy, U^d dissipated energy. During repeated loading/unloading, dissipated energy could be considered as the area encapsulated by strain axe and unloading curve in every circle. Thus,

$$D=\frac{U^d}{U}=\frac{U_i-U_i^e}{U} \tag{1.11}$$

U_i is the accumulated energy in *i* th loading cycle. U_i^e is the released energy in unloading process. Compacting factor K is introduced to describe the “compacting” degree in every loading procedure. K changes with strain ε as

$$K=\begin{cases} log_n\left[\frac{(n-1)\varepsilon}{\varepsilon_s}-1\right] & \varepsilon<\varepsilon_s \\ 1 & \varepsilon\geq\varepsilon_s \end{cases} \tag{1.12}$$

n is a constant, which could be obtained from tests, ε_s is the strain corresponding to yield point. Thus, the constitutive relation for damage is

$$\sigma=K(1-D)E\varepsilon \tag{1.13}$$

In the first loading, the equation (1.13) was employed. If the unloading is from point (ε_1,σ_1) to point $(\varepsilon^{p1},0)$, the unloading curve is described as：

$$\sigma = \begin{cases} \frac{\varepsilon-\varepsilon^{p1}}{\varepsilon_1-\varepsilon^{p1}} K_1(1-D_1)^{m1} E\varepsilon & \varepsilon^{p1} < \varepsilon < \varepsilon_1 \\ 0 & \varepsilon \leq \varepsilon^{p1} \end{cases} \tag{1.14}$$

Where K_i is the compacting factor in *i* th cycle, mi the fitting constant in *i* th cycle. In the reloading, the stress is

$$\sigma = \begin{cases} \frac{\varepsilon-\varepsilon^{p1}}{\varepsilon_1-\varepsilon^{p1}} K_2(1-D_1)^{m1} E\varepsilon & \varepsilon^{p1} < \varepsilon < \varepsilon_1 \\ K_2(1-D)^{m2} E\varepsilon & \varepsilon \geq \varepsilon_1 \end{cases} \tag{1.15}$$

In the *i* th cycle, loading, unloading stress-strain relations should be, respectively.

$$\sigma = \begin{cases} \frac{\varepsilon-\varepsilon^{pi-1}}{\varepsilon_1-\varepsilon^{p1}} K_{i-1}(1-D_1)^{mi-1} E\varepsilon & \varepsilon^{p1} < \varepsilon < \varepsilon_1 \\ 0 & \varepsilon \leq \varepsilon^{p1} \end{cases} \tag{1.16}$$

$$\sigma = \begin{cases} \frac{\varepsilon-\varepsilon^{pi-1}}{\varepsilon_1-\varepsilon^{pi-1}} K_2(1-D_1)^{mi-1} E\varepsilon & \varepsilon^{p1} < \varepsilon < \varepsilon_1 \\ K_i(1-D)^{i2} E\varepsilon & \varepsilon \geq \varepsilon_1 \end{cases} \tag{1.17}$$

1.3.3 Viscoplasticity model

①Viscoplasticity model with associated flow rule

M.C. Weng et al [92-95] studied Taiwan soft porous sandstone and found that the plastic flow vector is normal to the yield surface. Based on this fact, they developed a elasto-visco-plasticity model. The elastic part is

$$\varepsilon_{ij}^{e} = \frac{\partial \Omega}{\partial \sigma_{ij}} \tag{1.18}$$

Ω is the elastic energy density or elastic potential:

$$\Omega = b_1 I_1^{3/2} + b_2 I_1^{-1} J_2 + b_3 J_2 \tag{1.19}$$

where b_1, b_2, b_3 are material parameters; I_1 is the first stress invariant; J_2 is the second deviatoric stress invariant.

$$\varepsilon_{ij}^{e} = \frac{\partial \Omega}{\partial \sigma_{ij}} = \left(\frac{3}{2} b_1 I_1^{1/2} - b_2 I_1^{-2} J_2 + J_2\right) \delta_{ij} + (b_2 I_1^{-1} + b_3) s_{ij} \tag{1.20}$$

s_{ij} is the deviatoric stress tensor; δ_{ij} is the Kronecker matrix. The viscoplastic model adopted Cristescu model.

$$\dot{\varepsilon}^{I} = k \left\langle 1 - \frac{W(t)}{H(\boldsymbol{\sigma})} \right\rangle \frac{\partial F(\boldsymbol{\sigma})}{\partial \boldsymbol{\sigma}} \tag{1.21}$$

H is yield function; *W* is the hardening function representing the plastic work in unit volume; F is plastic potential function; k is viscosity coefficient. Angle brackets represent an operator whose result is zero when the inner bracket is negative; remain unchanged otherwise. If *H*=*W*, viscosity was activated, indicating the creep strain. Hardening parameter was introduced to describe the phenomenon of strain hardening and softening. Hydrostatic pressure $p = I_1/3$ casued the short-term plastic stress work W_h (obtained by fitting)

$$W_h(p) = h_0 p + h_1 p^2 \tag{1.22}$$

The short-term plastic work obtained through shear stress W_d is related to the hydrostatic pressure and shear stress, so it could be expressed as the function $W_d\left(p, \sqrt{J_2}\right)$

$$W_d\left(p, \sqrt{J_2}\right) = c(p)\sqrt{J_2} + d(p) ln\left[1 - \frac{\sqrt{J_2}}{\sqrt{J_{2f}}}\right] \tag{1.23}$$

$\sqrt{J_2}$ is defined as shear stress; $\sqrt{J_{2f}}$ is defined as shear strength. $c(p)$ and $d(p)$ are polynomial functions, obtained from data fitting. The plastic work due to creep W_c is

$$W_c\left(p, \sqrt{J_2}\right) = e(p)\sqrt{J_2} + f(p) ln\left[1 - \frac{\sqrt{J_2}}{\sqrt{J_{2f}}}\right] \tag{1.24}$$

Therefore the plastic potential is obtained. And substitute the equation (1.21),

$$\varepsilon_{ij}^{I}(t_1) = \frac{\langle H - W(t_0)\rangle \partial F/\partial \boldsymbol{\sigma_{ij}}}{(\partial F/\partial p)p + \left(\partial F/\partial\sqrt{J_2}\right)\sqrt{J_2}} \times \left\{1 - \exp\left[\frac{k}{H}\left(\left(\frac{\partial F}{\partial p}\right)p + \left(\frac{\partial F}{\partial\sqrt{J_2}}\right)\sqrt{J_2}\right)(t_0 - t_1)\right]\right\} \tag{1.25}$$

For the associated rule, the plastic potential, viscoplastic potential and yield function are the same

$$F\left(p, \sqrt{J_2}\right) = H\left(p, \sqrt{J_2}\right) = W\left(p, \sqrt{J_2}\right) = W(p) + W_d\left(p, \sqrt{J_2}\right) \tag{1.26}$$

In triaxial tests,

$$F = H = W(t_0) = W\left(pp, \sqrt{J_2}\right) \tag{1.27}$$

In creep tests,

$$F = H = W\left(p, \sqrt{J_2}\right) \tag{1.28}$$

$$W(t_0) = W_c\left(p, \sqrt{J_2}\right) \tag{1.29}$$

②Viscoplastic model under non-associated flow rule

Kavan Khaledi et al[102] adopt non-associated rule in the visco-plastic constitutive model. In elastic phase, linear Hooke’s law is applied

$$\dot{\varepsilon}_{ij}^{e} = \frac{1}{2G}\dot{s}_{ij} + \left(\frac{1}{9K} - \frac{1}{6G}\right)\dot{I}_{ij}\delta_{ij} \tag{1.30}$$

Visco-plastic model is the typical Perzyna model.

$$\dot{\varepsilon}_{ij}^{vp} = k\left\langle\frac{F^{vp}}{F_0}\right\rangle^{N}\frac{\partial Q^{vp}}{\partial\sigma_{ij}} \tag{1.31}$$

N is the fitting material parameter; k is viscosity coefficient; F_0 is a reference value in the unit of MPa^2. F^{vp}, Q^{vp} are the yield and potential functions:

$$F^{vp} = J_2 - (-\alpha I_1^n + \gamma I_1^2)[exp(\beta_1 I_1) - \beta cos(3\theta)]^m \tag{1.32}$$

$$Q^{vp} = J_2 - \left(-\alpha_q I_1^n + \gamma I_1^2\right)[exp(\beta_1 I_1) - \beta cos(3\theta)]^m \tag{1.33}$$

Where, γ, β_1, β, m are material parameters. Hardening parameters α and α_q are introduced to control the potential surface and yield surface. They evolve with the accumulated plastic strain.

$$\alpha = \frac{a_1}{\xi^{\eta}} \ , \ \xi = \int_0^t \sqrt{\dot{\varepsilon}_{ij}^{vp} : \dot{\varepsilon}_{ij}^{vp}} dt \tag{1.34}$$

$$\alpha_q = \alpha + a(\alpha_0 - \alpha)\left(1 - \frac{\xi_v}{\xi}\right) \tag{1.35}$$

a_1 and η are the material parameters. ξ_v is accumulated plastic volumetric strain. a is function of strain. At compression-dilatancy transition, volumetric strain rate is zero, so $\frac{\partial Q^{vp}}{\partial I_1} = 0$. Hence, the dilatancy boundary is

$$J_2 = \left(1 - \frac{2}{n}\right)\gamma I_1^2 [exp(\beta_1 I_1) - \beta cos(3\theta)]^m \times \left\{1 + \frac{m\beta_1 I_1 exp(\beta_1 I_1)}{n\left(exp(\beta_1 I_1) - \beta cos(3\theta)\right)}\right\} \tag{1.36}$$

The last term in this equation can be neglected, which yields

$$J_2 = \left(1 - \frac{2}{n}\right)\gamma I_1^2 [exp(\beta_1 I_1) - \beta cos(3\theta)]^m \tag{1.37}$$

1.3.4 Numerical simulation of constitutive models

The proposed constitutive models must be tested against the engineering experience and experimental data. We will test the model using two approaches. The first one uses industrial numerical software. In the second approach, the new constitutive models are written in computer language to realize the examination [103-110]. The second method uses the existing algorithm theory to compile calculation procedure [111-116]. The later method is of high requirement, more difficult in post-processing, therefore is used rarely. The former approach is relatively simple and practicable and could save a large amount of time and vigor by using mature software to do pretreatment and posttreatment work.

FLAC3D finite-difference code is one of the most popular in geoengineering. I will briefly introduce the stylized research with the second development interface of Flac3D software as followed. In FLAC3D, compiling a new constitutive model has three steps: modifying head file, modifying resource file, creating ".DLL" file.

① Modifying head file

Head file is to declare the functions and variables including the parameters and intermediate variables.

② Modifying resource file

Resource file is the main C++ program:

1) Modify Structure function. Structure function is to initiate the values of variables defined in head files and used in resource file. Normally, the initial values are zero.

2) Modify Properties() function. Properties() function is to name the parameters in

the model, usually in the form of character string. During the calculation with FLAC3D, computer assigns the parameters by identifying these characters, for example, bulk, shear, tension.

3) Modify GetProperty() and SetProperty(). The two functions are to implement the assignment.

4) Initialize() function is to re-initialize the parameters and the state of every elements and the private variables when executing the Cycle order or calibrating the large strain.

5) Run() is the main function of the model. In every timestep of the calculation, computer should invoke Run() function for every element to obtain the new state.

6) Modify SaveRestore() function. SaveRestore() function is to save the results of calculation.

③ Create ".DLL" file

This step is to generate the library files identifiable by the software.

1.4 Comprehensive utilization of salt cavern

China's underground salt resource is abundant and distributes widely with the burial depth from several to 4000 meters, having the material basis of constructing underground salt caverns [2, 5, 7, 117]. East China such as, JiangSu province, ZheJiang province, ShangDong province, is densely populated, economically developed and hugely energy-consuming, is appropriate to build salt cavern natural gas storages [118, 119]. In underpopulated western regions, such as Xinjiang province, there are also many large salt formations recently discovered, which could be the subterranean disposal site for nuclear waste. In Sichuan Zigong and Henan Pingdingshan, there are a large number of abandoned salt caverns after hundreds of year exploitation, posing big threats to environment. Caustic dross disposal medium or gas storages both are good ways to address this problem. Additionally, as stated in section 1.1.2, CAES is a promising direction for China to develop clean renewable power, solar, wind power. Finally, the premise of comprehensive utilization of salt cavern should take the consideration of the stability and impermeability under complex loading conditions.

1.5 Main research content (of the thesis) and technology roadmap

1.5.1 Main research content

This research funds comes from China’s key fundamental research developing plan, 973 program. To study the rock mechanical properties, the uniaxial and triaxial tests are necessary, in which the rock samples are subjected to a continuously increasing stress before failure. In engineering practice, rock salt is always subjected to a repeated discontinuous cyclic pressure. Therefore, conducting the discontinuous cyclic loading tests is indispensable for understanding the discontinuous fatigue properties, so that it is adapted to the mechanical response of underground salt cavern under discontinuous cyclic loading.

The research content includes the following parts:

① The basic properties are the premise of fatigue tests. SEM and X-ray diffraction spectrum are employed to identify the chemical composition and structure of salt. The compression strength (UCS), elastic modulus, Poisson ratio, friction angle and cohesion are calculated from triaxial compression tests data. Dilatancy effect causes the volume expansion and increase of permeability/porosity, growth of cracks, inducing the mechanical instability of engineering. The first part summarized the salt dilatancy general features and find out demarcation point of compression-dilatancy.

② Rock salt is a kind of strongly time-dependent rock material. In conventional loading test, it yields early during the loading, and then appears long-term strain hardening, generating large plastic deformation. Seizing the description of strain hardening is the key of the new constitutive model.

③In terms of the strength, the upper stress limit and lower stress limit are determined for the conventional fatigue test. Considering the effect of geothermal temperature, gas filling and the recovering velocity, the fatigue tests with different temperature and loading velocity were conducted.

④ Plasticity development is related to the loading history. After completing every cycle, the fatigue damage is increased and the mechanical properties change. Therefore, in the new model, the cyclic loading is taken into account.

⑤ Conducting discontinuous fatigue tests is aimed at studying the salt properties under discontinuous loading. The acoustic emission detection technology was applied to track the fatigue damage evolution.

⑥ Modify the fatigue constitutive model to correctively describe the behavior of salt under discontinuous loading. Based on the dislocation theory, explain the behavior shown in various loading path, providing reference for developing CAES or salt cavern gas storage.

1.5.2 Technological roadmap

The detailed roadmap is followed as in Fig. 1.6:

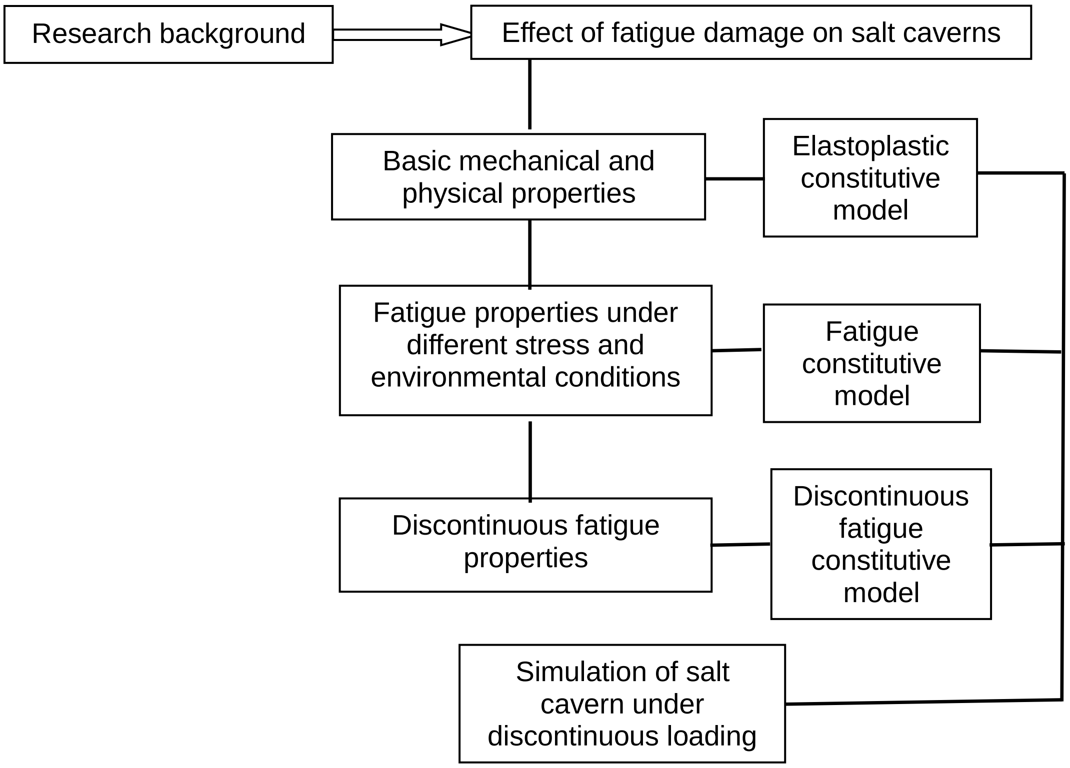

Fig.1.6 Roadmap of this research

2 Dilatancy properties of salt under monotonous compression and brief introduction into dislocation theory

Underground salt caverns form during exploiting NaCl sedimentary. NaCl crystal is isometric system hexoctahedron symmetry class. Monocrystal appears hexahedron, typical structure of AX type chemical compound, where negative ions are located in angular point and face center of cubic hail and close piling up and positive ions fill the hole inside the hexahedrons. Fresh surface of NaCl crystal appears metallic luster. NaCl crystal easily deliquesces and has full cube cleavage plane.

Fig.2.1 NaCl crystalline

Salt deposit is one kind of chemical sedimentary deposit forming by vaporizing and eliminating water in dry climate conditions during geological process. Deposition type of ore deposit occurs as bedded and contains impurities of mudstone in some situations. Because of the tectonic movement, rock salt layer flows upward, intrudes into overlaying rock or hog overlaying rock, forming salt domes. Most of rock salt layer have simple morphology and are bedded.

Salt cavern construction as the ideal reservation site of oil and natural gas and subterranean disposal site of highly active nuclear waste is exploited and utilized with various risk accompanied, such as, volume shrinkage of cavity, surface subsidence et al. In this chapter, investigation into the basic properties is performed to lay the foundation for the subsequent research presented in the following chapters.

2.1 Experimental conditions

2.1.1 Samples

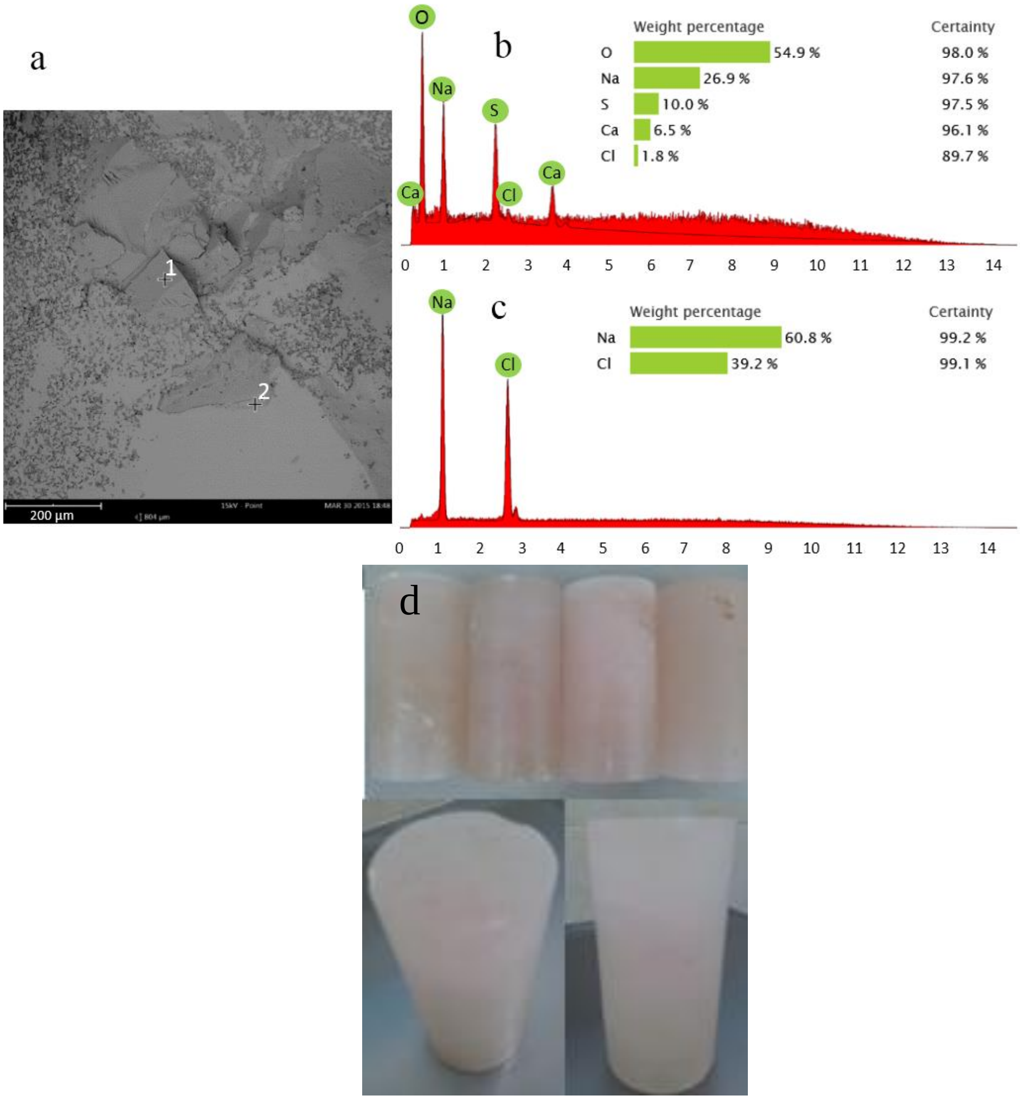

Fig.2.2 SEM image of the salt rock (a) and the chemical elements at the two indicated points detected by X-ray spectrum (b corresponding to point 1 and c corresponding to point 2). The salt rock samples (d).

Rock salt samples have been collected in the Himalaya Mountains in Pakistan from depth of 800~1000m. Salt surface appears light red or white. There are more than 96%

of NaCl and bits of K_2SO_3 and mud impurities in the salt. Fig. 2.2 shows the samples, the observed SEM images and the results of elemental analysis by X-ray diffraction under two indicated point. The host body of the sample is NaCl crystal as shown under point 2， while point 1 shows some impurities, Na_2SO_3 or Ca_2SO_3. The impurities are encompassed by the host crystal, but have relatively independent structure as a perfect crystal. Impurity crystal shapes to the main cube and have cleavage surface of cubic system.

The samples are prepared to have a standard cylindrical shape with 50mm diameter and 100mm height. Before the tests, the end faces of samples are polished to ensure the smoothness within ±0.02 mm.

2.1.2 Experimental equipment

The loading equipment is a triaxial rigid testing machine designed and developed in our state key laboratory (Fig. 2.3). The loading power is provided by a computer double servo hydraulic automatic control loading system. This machine is able to perform uniaxial compression tests, triaxial compression tests, fatigue tests and other complicated loading tests for geomaterials.

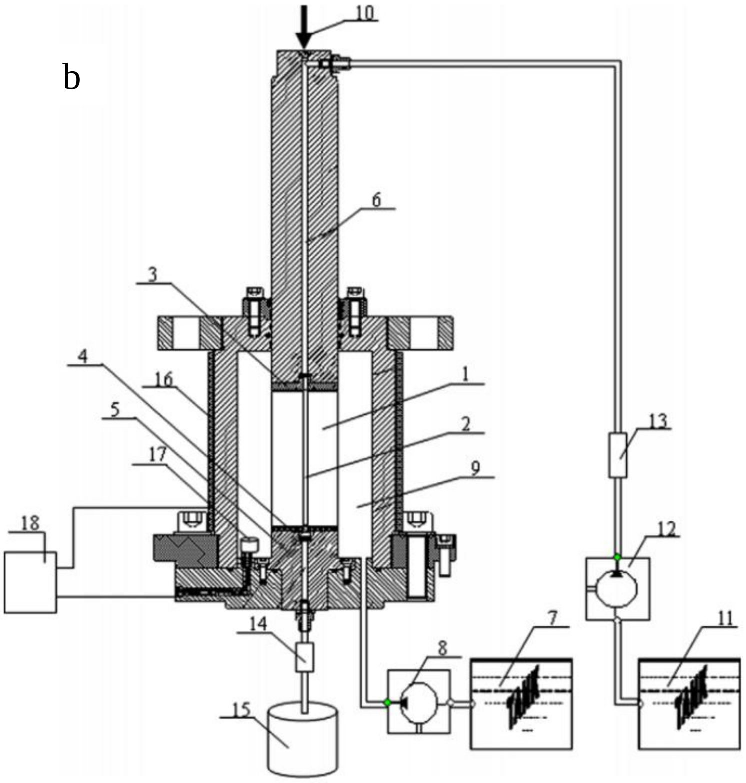

Fig.2.3 a. High temperature triaxial test machine. b. Structure of the loading machine. 1.salt rock sample; 2.limber; 3.compessiom plate; 4.compessiom plate; 5.engine base; 6-strut; 7.cylinder; 8-servo hydraulic station; 9-confning pressure chamber; 10-axial compression; 11.dissolved liquid cylinder; 12.brine pump; 13.flowmeter; 14.relief valve; 15.dissolved liquid container; 16-heat tape; 17.temperature sensor; 18-temperature controller.

This machine consists of dual servo hydraulic station, computer test and control system, mainframe and connecting lines. Dual servo hydraulic station independently supplies power to an axial loading system and confining pressure system. Via electro-hydraulic servo valve, computer could control the process of loading, and unloading, loading rate and loading target etc. Mainframe (Fig. 2.3b) is used to load the samples and to apply pressure and temperatures. This system is able to provide an axial load less than 40 tones and the confining pressure less than 30 MPa. The indicated accuracy of pressure measurements is ±0.8%.

Series of uniaxial and triaxial experiments are conducted with the constant loading velocity of v_S=0.02mm/s or v_F=0.2KN/s. At the ends of samples, polyester fiber mat layer and lubrication (Fig. 2.4) are used to avoid noise and reduce friction.

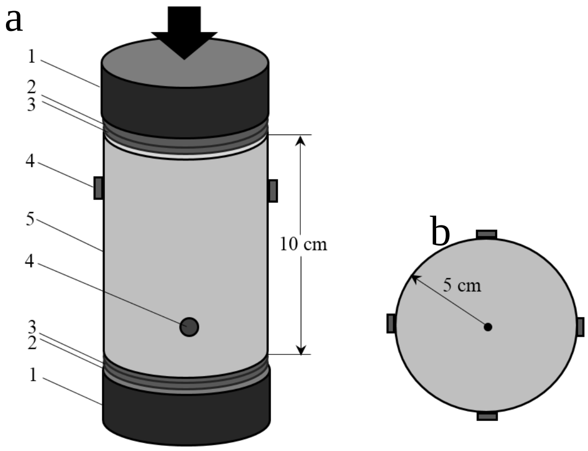

Fig.2.4 . Test setup (a); position of AE sensors, in front view (a) and top view (b); and a typical stress-strain curve (c) from uniaxial compression test. (1) Steel platen; (2) Teflon gasket; (3) lubricant; (4) AE sensor; (5) rock salt sample.

2.2 Dilatancy features in uniaxial tests

①Loading features

To keep in consistency with the subsequent experiments, uniaxial tests employed the stress control mode, with 0.2KN/s loading velocity. The loading continues until failure. Fig. 2.5 shows the load and displacement evolution under stress control mode: after the peak, sample loses the bearing capacity and stress drops rapidly. This also is the disadvantage of stress control mode: the rapid drop cannot give much time to obtain dense enough data. Since the upper and lower stress limits are fixed in fatigue tests, the stress control mode has to be applied.

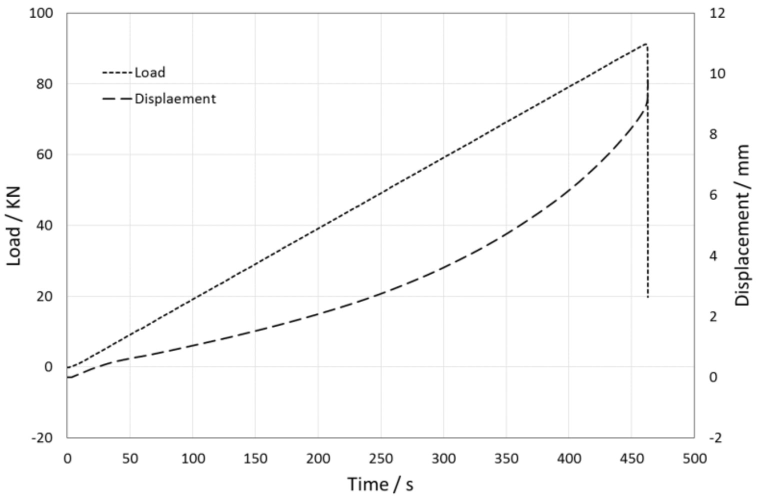

Fig.2.5 Load, displacement path in uniaxial test

The test results show that: the stress increases linearly, following the control of servo system. However, the displacement increases linearly with time only at early stages and the increase become exponential. The demarcation point between linear segment and exponential segment is ambiguous, indicating that elastic phase and plastic phase are mutually intricate.

②Volume expansion features

Volumetric strain is calculated as

$$\varepsilon_v = \varepsilon_1 + 2\varepsilon_3 \tag{2.1}$$

Fig. 2.6 shows the curve of axial stress-axial strain, lateral strain and volumetric strain. To avoid the superposition of radial deformation curve and volumetric deformation, the expansion of lateral strain is defined as positive (just applied in figures).

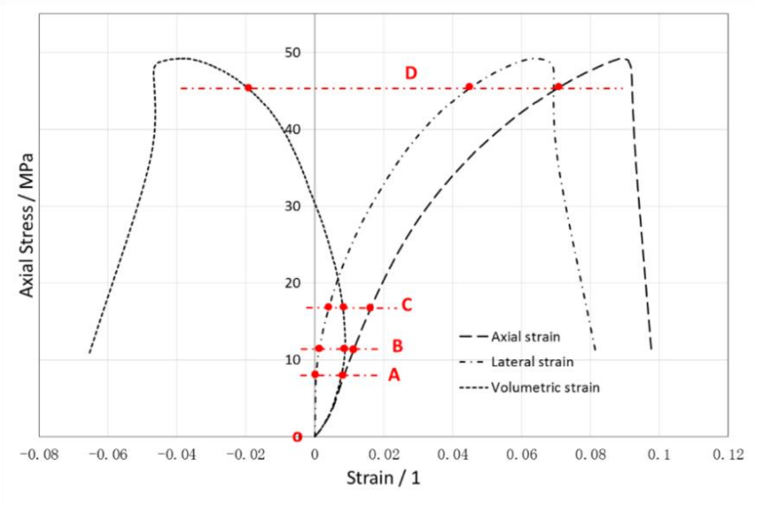

Fig.2.6 Axial strain, lateral strain and volumetric strain curves

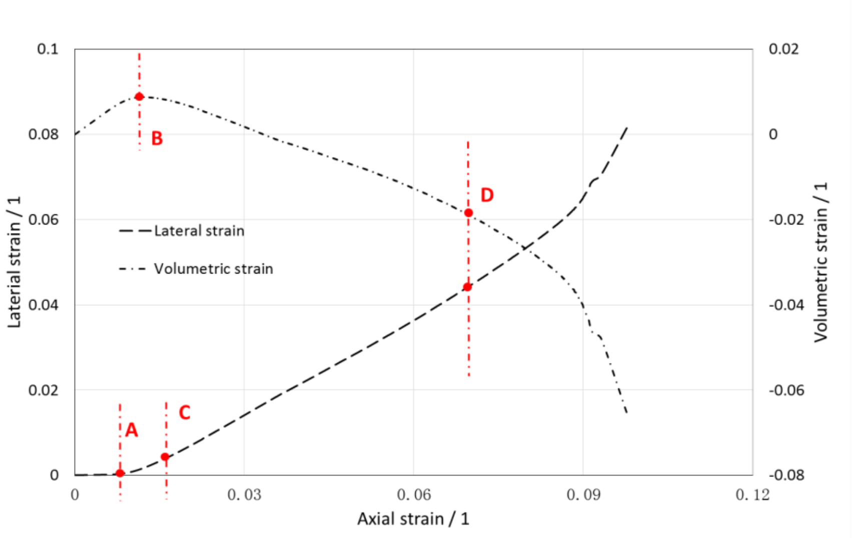

Fig.2.7 Lateral strain and volumetric strain as a function of axial strain

During the continuous loading the axial and radial strains increase all the time, while the volumetric strain decreases first and then increases. Three curves show the main features as follows:

Axial strain at the initial loading stage (OA segment), grows slowly, then experiences a short linear increase (AC segment). Usually the two stages were considered as compaction stage and elastic stage, respectively. Afterwards strain rate rises until failure as the stress increases.

Radial strain at the initial loading stage (OA segment), is hardly detectable, until the stress goes up to a certain value (~8MPa corresponding to A point). Thereafter, strain rate rapidly rises.

Volumetric strain goes down at the beginning, indicating that the sample as a whole is compacted. The reduction trend is transformed into an increase at ~11.5MPa (point B in Fig. 2.), where the demarcation point of compaction-dilatancy is located, indicating the volumetric reduction transformed into expansion. In dilatancy stage, volumetric strain increases.

In uniaxial test, there is no distinct elastic phase and elastoplastic phase. From the above description, the deformation stages can be summarized as follows.

Compaction stage. At the initial loading, sample experience a short compaction period from point O to point A, in which the axial strain develops with a slowing rate and the lateral strain is very small. Therefore, the volume reduces.

Composite stage. Following the compaction stage, the lateral strain increases. The sample experiences a combined effect of compaction and dilatancy, from A to C. Sample is completely compacted at point C. At this stage, the lateral strain accelerates with axial strain and stress. Since the elastic behavior of salt is linear, this stage is judged elastoplasticity which would cause dilatancy. It is the interaction of compaction and dilatancy that make the volumetric strain rate to be zero at point B, where the dilatancy point (demarcation point of compression and dilatancy) is.

Plastic stage. After complete compaction, the plastic deformation is totally due to dislocation mechanism, from point C to D. Because microcracks at this stage just finish nucleation and the scale is negligible, the lateral strain and volumetric strain develop linearly with axial strain.

Fracture stage. As the plastic strain accumulates, the connectivity of the microcracks develops which in turn influences the volumetric deformation. Cracks could produce more space inside the samples than dislocations; therefore the volumetric deformation develops faster and faster with axial strain. Once the thoroughgoing crack is formed, the failure occurs (from point D to failure).

One thing to note is that all through the deformation process is elastoplastic behavior, the elasticity and plasticity are intertwined, not mutually independent. Additionally, the segments points are distinguished by ocular estimates, in terms of the curve flatness, having strong subjectivity. The partition for every stage is not accurate, but the purpose is to understand the deformation mechanism in every stages.

③Elastic constants

Since the elasticity reflects the recovery properties, elastic constants are determined from unloading test. Jiang Deyi et al [43-46] found that the elastic modulus and Poisson’s ratio are not constant but vary with damage. As the loading proceeds in uniaxial compression test, elastic modulus increases from 6.3GPa to 6.7GPa with fluctuations of ±0.05GPa and Poisson’s ratio increases from 0.04 to 0.1. The reason for these changes is the degradation of inner particle structure. To facilitate the analysis, we assume the average values of the elastic parameters (2.2)

$$\begin{cases} E = 6.5\text{GPa} \\ \mu = 0.07 \end{cases} \tag{2.2}$$

E and μ are the Young’s modulus and the Poisson’s ratio, respectively. The shear modulus and bulk modulus can be obtained from

$$\begin{cases} G = \frac{E}{2(1+\mu)} = 3.04\text{GPa} \\ K = \frac{E}{3(1-2\mu)} = 2.52\text{GPa} \end{cases} \tag{2.3}$$

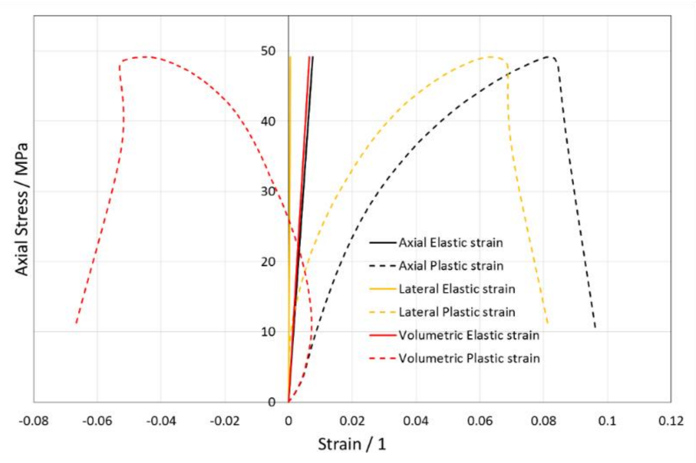

Fig.2.8 Elasticity and plasticity for uniaxial test

Plastic strains and elastic strain were calculated and are shown in Fig. 2.8. It is seen that the plastic curves are almost the same as in Fig. 2.6. Elastic strain is very small. This demonstrates that the plastic deformation has the overwhelming superiority among the deformation in rock salt. Therefore the description of the plasticity is fundamental for predicting the mechanical response of salt.

Dilatancy is the main mechanism causing in the volume increase. Here the generalized shear strain and shear stress are defined to obtain the parameters reflecting the dilatancy.

$$\begin{cases} \bar{\gamma} = 2\sqrt{J_2'} = \sqrt{2e_{ij}e_{ij}} = \sqrt{2\left(\varepsilon_{ij} - \frac{1}{3}\varepsilon_v\delta_{ij}\right)\left(\varepsilon_{ij} - \frac{1}{3}\varepsilon_v\delta_{ij}\right)} \\ \bar{\tau} = \sqrt{J_2} = \sqrt{s_{ij}s_{ij}} = \sqrt{(\sigma_{ij} - \sigma_m\delta_{ij})(\sigma_{ij} - \sigma_m\delta_{ij})} \end{cases} \tag{2.4}$$

e_{ij} and s_{ij} are the deviatoric strain and deviatoric stress tensors. ε_v and σ_m are volumetric strain and mean stress. δ_{ij} is Kronecker tensor. In uniaxial tests, generalized plastic shear strain and generalized shear stress are shown in Fig. 2.9.

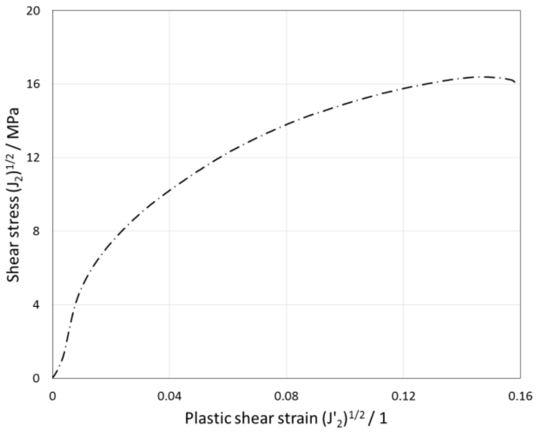

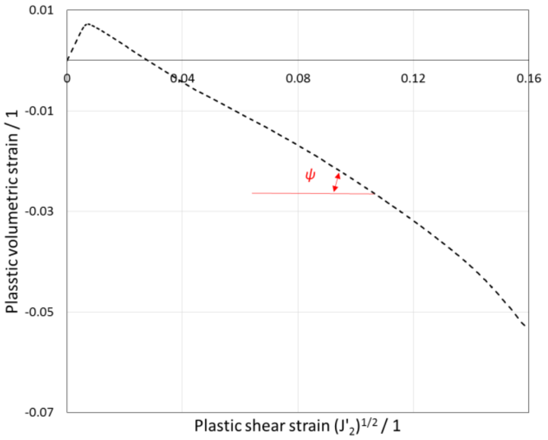

Fig.2.9 Shear stress-plastic *vs* shear strain

Fig.2.10 Plastic volumetric strain *vs* plastic shear strain

Dilatancy angle is defined as show in Fig. 2.10,

$$tan\psi = -\frac{\Delta\varepsilon_v^p}{\Delta\bar{\gamma}^p} = \beta \tag{2.5}$$

β is the dilatancy factor. Dilatancy angle initially is negative, indicating that the volume reduction then it becomes positive at point B and reaches a constant level around point C, after point D rises gradually with plastic shear strain.

④Rupture features

At the beginning of the loading (OA segment), nothing happens with the sample. In the AC segment, the some changes at the sample surface occur, normally light red color is changed white. This is caused by the grain reduction. The new-forming crystal boundaries and subboundaries block the light path for transmission. In CD segment, the sample surface does not change much. After point D, macrocrack appears on the surface and continuously grows up to cutting through the whole sample (Fig. 2.11).

Fig.2.11 Specimen failed in the uniaxial test

2.3 Dilatancy in triaxial compression test

Both in the salt cavern construction and underground excavation, the surrounding rock is in the 3-D stress state. Investigation of the properties of rocks under triaxial loading is more meaningful for engineering practice.

The same samples and loading equipment are used in triaxial compression tests. The processed samples are grouped to conduct the tests with different confining pressure. First the confining pressure is increased to the designed value with the velocity of 0.05MPa/s, and then the axial stress is increased with the velocity of 0.2KN/s. The tested confining pressure values are: 3MPa、5MPa、7MPa. Because the range of the device measuring the lateral elongation is limited, the deformation cannot be measured all through the test.

The stress-strain curves from triaxial compression tests are similar to those from uniaxial compression tests, showing the same (as previously) features shown in Fig. 2.12~ 2.17. This indicates the same mechanism behind the deformation, which would be explained in the dislocation section.

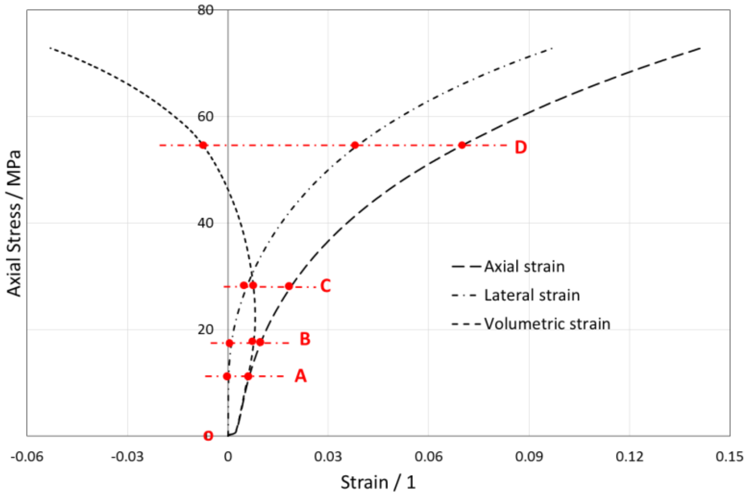

Fig.2.12 Axial strain, lateral strain and volumetric strain curves from a triaxial test with 3 MPa of confining pressure

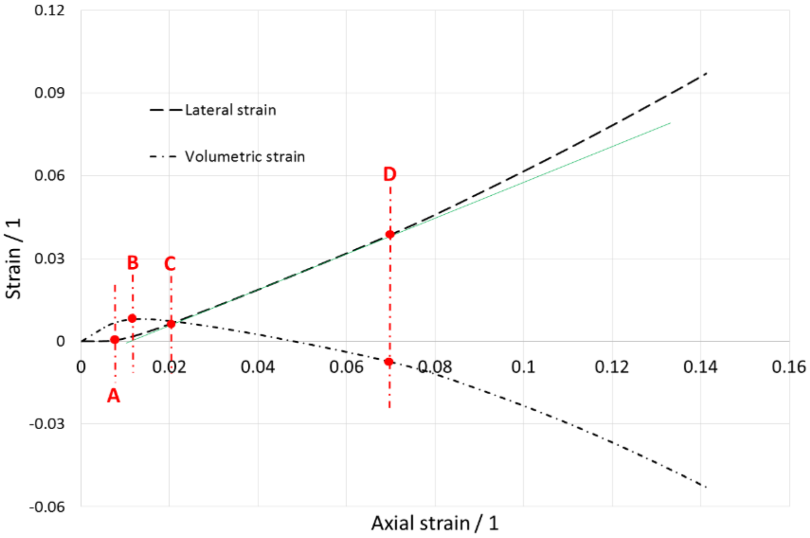

Fig.2.13 Lateral strain and volumetric strain as a function of axial strain from a triaxial test with 3 MPa of confining pressure

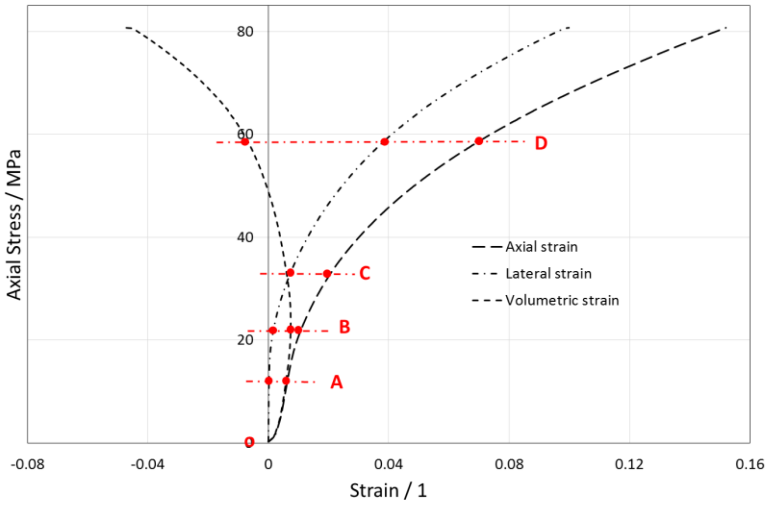

Fig.2.14 Axial strain, lateral strain and volumetric strain curves from a triaxial test with 5 MPa of confining pressure

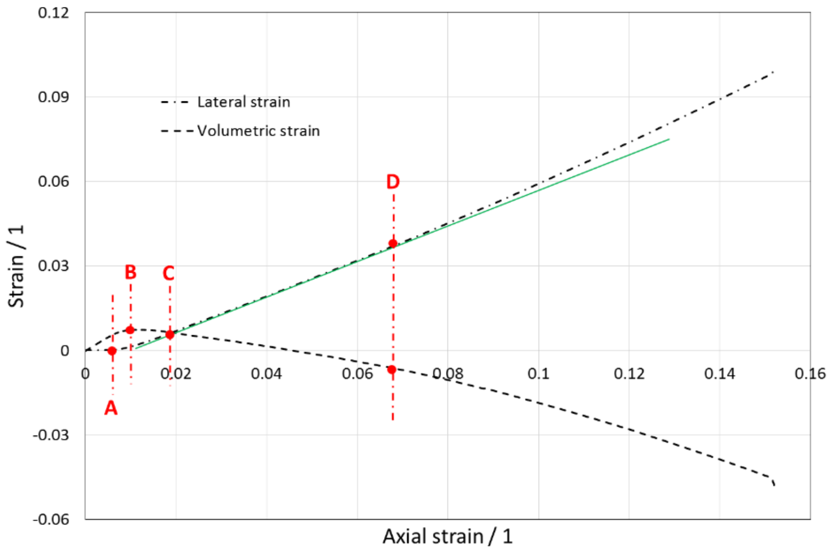

Fig.2.15 Lateral strain and volumetric strain as a function of axial strain from a triaxial test with 5 MPa of confining pressure

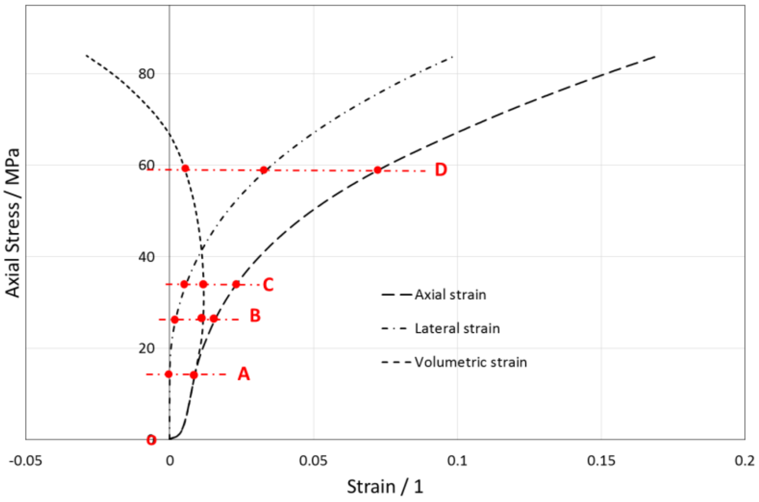

Fig.2.16 Axial strain, lateral strain and volumetric strain curves from a triaxial test with 7 MPa of confining pressure

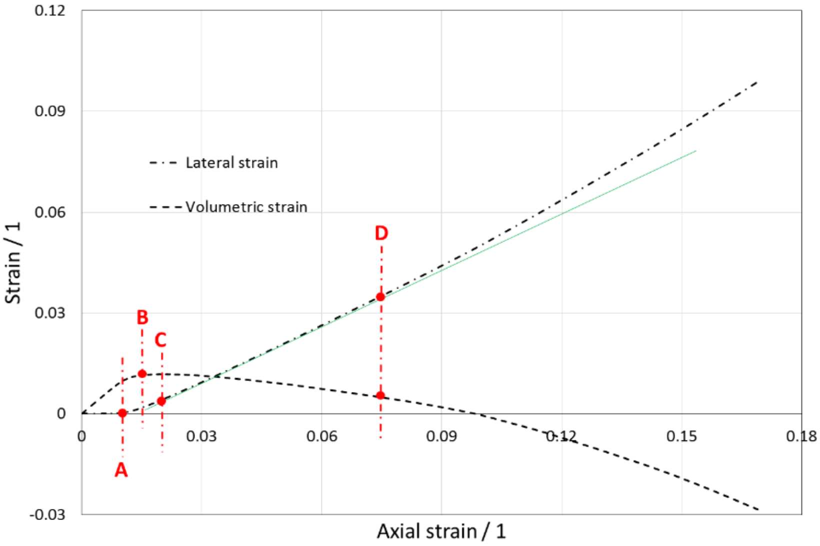

Fig.2.17 Lateral strain and volumetric strain as a function of axial strain from a triaxial test with 7MPa of confining pressure

The stress-strain curves have similar characteristics of stages. The axial strains corresponding to the indicated points (see table 2.1) are similar. Point A represents initial point of lateral strain, at around 0.75% of ε_1. Point C represents the complete compaction, at around 2% of ε_1. Point B represents the demarcation point of compression-dilatancy, where the strain rate is zero. Point D represents that the cracks run through, a new expansion mechanism, occurs 6.8~7.5% of ε_1.

Table 2.1 Axial strain corresponding to the turning points in different tests

Confining pressure σ_3 */ MPa*	*0*	*3*	*5*	*7*
Corresponding axial strain for A	0.79%	0.72%	0.77%	1.03%
Corresponding axial strain for B	1.17%	1.25%	1.02%	1.61%
Corresponding axial strain for C	1.76%	2.01%	1.86%	2.10%
Corresponding axial strain for D	6.95%	6.98%	6.78%	7.50%

With the increasing confining pressure, the constants change: both the elastic modulus and Poisson’s ratio increase; the compression strength has a remarkable rise. The axial strain corresponding to the peak stress also increases significantly (see table 2.2). All the data are obtained at room temperature 26-30℃ and with the loading velocity of 0.2KN/s.

Table 2.2 Variation of elastic parameter with confining pressure

Confining pressure σ_3 */ MPa*	*0*	*3*	*5*	*7*
Elastic Modulus E / GPa	6.50	7.40	8.10	8.65
Possion’s ratio μ	0.07	0.11	0.14	0.16
Compression strength σ_c / MPa	47.1	75.2	89.3	106
Axial strain corresponding to σ_c	8.92%	19.93%	25.3%	29.1%

Here, we defined the (shear-) dilatancy angle and axial-dilatancy. The tangents of them two are defined as the ratio of volumetric strain to shear strain, the ratio of volumetric strain to axial strain, respectively. Confining pressure also impacts the growth of plastic deformation: a larger confining pressure results in a smaller (shear-) dilatancy angle ψ, axial-dilatancy θ angle and greater plastic deformation.

Table 2.3 Variation of shear-dilatancy angle and axial-dilatancy angle with confining pressure

Confining pressure σ_3 */ MPa*	*0*	*3*	*5*	*7*
Shear-dilatancy angle $\tan\psi$	0.33	0.25	0.21	0.15
Axial-dilatancy angle $\tan\theta$	0.36	0.27	0.24	0.18

During AD segment, under the effect of compaction and dilatancy, the salt sample mainly deformed, without visible macrocracks on the surface (Fig. 2.18). After point D, the macrocracks initiate, propagate and connect, forming the cracks (Fig. 2.19).

Fig.2.18 Deformed salt rock specimen before D point from trial tests

Fig.2.19 Fractured salt rock specimen after D point from trial tests

2.4 Dislocation theory

2.4.1 Conceptual framework of dislocation

Rock salt is one kind of crystal structure, whose mechanical behavior is affected by the dislocation. As there is rarely application of dislocation theory in rock mechanics field, we briefly introduce the dislocation theory. In practice, various defects including point defect (impurity atom), planar defect, volume defect, exist in crystal and strongly change the properties of salt. Dislocation is actually a kind of line defect. There are two types of dislocations, edge dislocation and spiral dislocation. Mixed dislocation is the combination of the two.

Dislocation theory is proposed to explain the plastic deformation. Fig. 2.20 shows the deformation process of an intact crystal lattice overcoming slip resistance under the drive of shear stress.

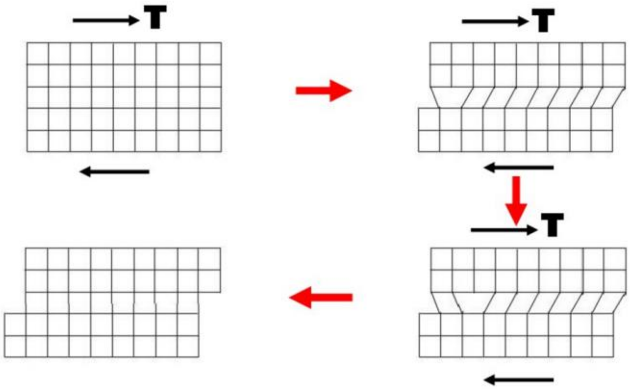

Fig.2.20 Sliding in the crystal lattice under shear stress

Edge dislocation is an extra half atomic planes during gliding process, typical of dislocation, as shown in Fig. 2.21. Two categories of edge dislocation are positive and negative.

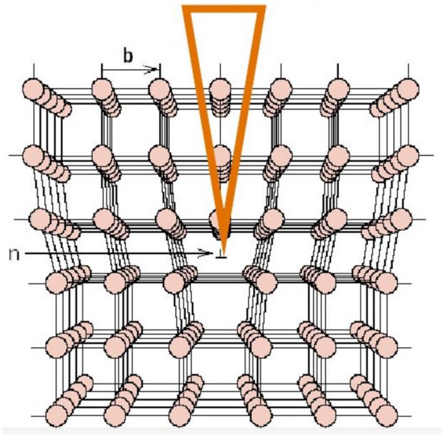

Fig.2.21 Edge dislocation

With an applied shear stress, a side face of simple cubic crystal generates a relative scrape edge of crystal under and below the glide plane, making unaligned phenomenon around the boundary between slip zone and non-slip zone, forming a spiral line surrounding the boundary. The original lattice plane cross by the boundary turns into spiral surface. This lattice imperfection is screw dislocation, as shown in Fig. 2.22. Two categories of screw dislocation are left and right.

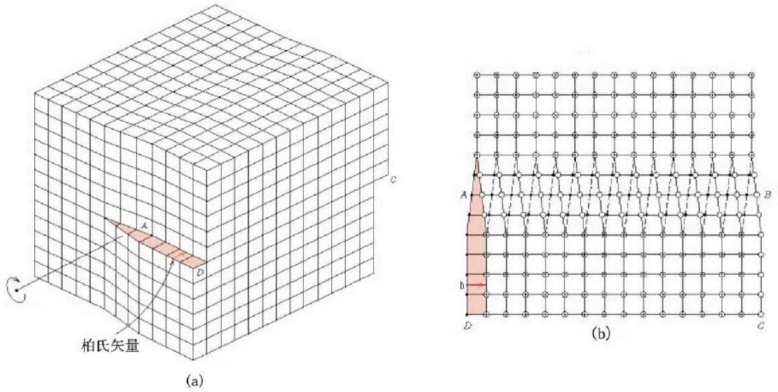

Fig.2.22Screw dislocation

As the dislocations exists in the crystal, the atoms around the dislocation line deviate from the normal position, causing the lattice distortion and generating stress field. The stress state of that area removed the center region could be solved through the elastic theory. Dislocations cause the lattice distortion, leading to energy rise. The energy increment belongs to the dislocation strain energy, including elastic energy and core energy at the dislocation core.

Some vacancy condensation could occur during crystallization, forming dislocation sources. Three mechanisms for dislocation formation are formed by homogeneous nucleation, grain boundary initiation, and interfaces the lattice and the surface, precipitates, dispersed phases, or reinforcing fibers. Under the stress, dislocation source in the stress concentration area would ceaselessly emit dislocations to the glide direction. Once encounting obstacles, such as impurity atom, crystal boundary and subboundary, dislocations are impeded and stop gliding. As the following dislocations come, dislocation would pile up and the stress field would add together. To continue the dislocation glide, larger stress needs to apply to surmount the added stress field of pile-up dislocations. Once the number of pile-up dislocations exceeds a certain value, the crack would initiate.

As dislocations are impeded and piled up, the external force has to increase to satisfy the force balance, appearing the strain hardening or strengthening. In terms of the mechanism, strengthening can be classified as: solution strengthening, dispersion (second phase) strengthening, refined crystalline strengthening, precipitation strengthening, strain strengthening and aging strengthening etc.

2.4.2 Dislocation behavior of salt under monotonous compression

Dislocations always form by slippage and moving of the lattice structure under shear stress. The dislocation slippage would normally leave a (set of) slip line(s). We used the same sample with the previous tests to observe the slip lines in salt. After subjected to shear stress, the sample surface was polished and then soaked in the glacial acetic acid 15 min. the observed slip lines are shown in Fig. 2.23.

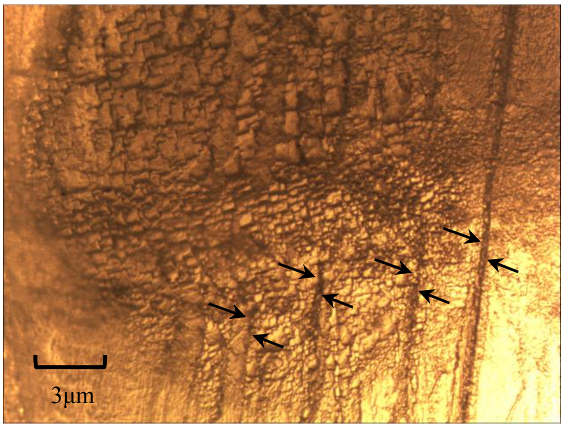

Fig.2.23 Dislocation slide lines in the salt materials

The process of loading on the samples actually is an interactive process between dislocations and external force. There are numerous pores and microcracks inside the natural rock salt. In the compaction stage, salt is subjected to the external force, the original cracks are compacted while the lateral strain does not occur, this corresponds to the nonlinear elasticity, since the lateral stress is fixed. In this phase, stress concentration usually occurs around the crack tips, where the dislocation sources are activated to emit dislocation, leading to irreversible deformation. Therefore the compaction is one kind of plastic behavior in some ways. This is the dislocation activities in OA segment.

In AC segment, as the stress increases, crystal structures gradually deform. Some of them are transformed into small size and a large amount of new subboundaries and boundaries form, leading to that the light-admitting quality reduces. The sample surface looks light red turning into white.

In CD segment, owing to the new crystal boundaries, the dislocations are impeded and piled up, resulting in the internal stress superposition. The impurity atoms also can block the slippage of dislocations. As the loading continues, these impediments increase external forces. Dislocation is one kind of lattice distortion leading to the volume increase. Because cracks are just in the stage of nucleation or propagate rather slowly, the dilatancy almost completely comes from dislocations, so the increment of volumetric strain is stable and linearly changes with the axial strain.

After point D, the number of plied-up dislocations comes to a critical limit. Cracks start to propagate and connect generating volume increase. In this stage, the volumetric strain increases rapidly in a geometric progression. As the lattice structures are distorted to a limit, some impurity atoms would separate out from the lattice, forming second phase. The second phase would further impede the dislocation and increase the internal stress. The cracks reduce the effective bearing area. When the average stress applied on the effective bearing area is large enough to destroy all the rest bearing element, the peak stress arrives. After peak, the cracks continue propagating and effective bear element continue reducing, resulting in a larger stress concentration.

As the salt samples are confined, crystal boundaries are protected better, needing more energy to open. More dislocations would traverse the crystal boundary. Therefore the plastic deformation is larger under larger confining pressure.

2.5 Chapter summary

In this chapter, the dislocation theory is used to explain the behavior of salt under continuous compression. In the uniaxial compression tests the deformation is mostly plastic, the elastic deformation being very small. The dilatancy behavior of salt could be understood considering three mechanisms and four stages.

Three mechanisms:

Compaction: at lower stress, the pores are compacted.

Dislocation: plastic deformation is induced by the dislocations causing the lattice structure distortion.

Crack: at higher stress, the cracks propagate and result in the increase of internal space.

Four stages:

Compaction stage: dislocations move around the tips of original pores/defects and the total volume reduces.

Composite stage: numerous dislocations at the stress concentration area slip and the compaction simultaneously continues. The volume development transforms from compaction to expansion.

Plastic stage: the microcracks are in the nucleation, but negligible to the volumetric increment. Dislocation slipping results in plastic volumetric increment, which is linear with axial strain.

Rupture stage: lattice structures distort to a critical limit. Crystal boundaries transform into cracks and greatly volume increase.

The process of loading on the salt actually is an interactive process between dislocations and external force (see section2.4.2). In triaxial compression tests, as the confining pressure increase,

①Elastic modulus and Poisson’s rate as well as the strength increase with the confining pressure P_c.

②Dilatancy difficulty increases and dilatancy angle decrease.

③Crystal boundaries are fortified and more dislocations could traverse the boundaries, leading to a larger plastic deformation at higher P_c.

3 Elastoplastic constitutive model considering the effect of hydrostatic pressure

Constitutive equations (models) mathematically describe the material behavior by defining relations between stresses and strains or their velocities Along with the universal laws (such as, mass conservation, momentum conservation, force balance), the constitutive laws are necessary to solve mechanical boundary value problems.

In previous chapter, we analyzed the elastoplastic deformation in conventional compression tests. It is known however, that the information obtained from the laboratory tests is limited and should be generalized by constitutive modeling.

3.1 Elastic framework

Elastic deformation is reversible, identified from unloading process. The unloading curve is found not a straight line and does not overlap with the previous loading curve, forming a hysteresis loop (Fig. 3.1). Compared to the total deformation, the hysteresis loop is small, the unloading curve is a line and overlaps with the previous loading curve. Therefore, the elastic behavior could be described by Hook's Law.

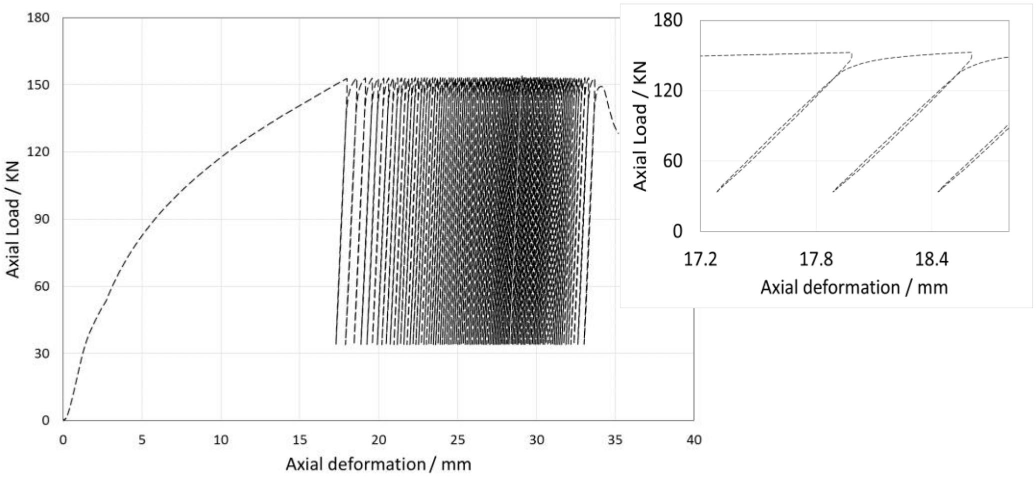

Fig.3.1 Axial Load versus axial deformation curve from cyclic loading triaxial test for $P_c = 5$ MPa

$$\sigma_{ij} = K\left(\varepsilon^e_{kk}\delta_{ij}\right) + 2G\left(\varepsilon^e_{ij} - \frac{1}{3}\varepsilon^e_{kk}\delta_{ij}\right) \tag{3.1}$$

σ_{ij} is the stress tensor; ε^e_{kk} is the elastic volumetric strain; ε^e_{ij} is elastic strain tensor. Bulk modulus K and shear modulus G could be calculated from Young's modulus and Poisson's rate. $\varepsilon_{kk}^{e}\delta_{ij}$ is spherical part of the stress tensor, while $\varepsilon_{ij}^{e}-\frac{1}{3}\varepsilon_{kk}^{e}\delta_{ij}$ is deviatoric part (denoted as e_{ij}^{e}). Hook's equations also could be decomposed into hydrostatic part and deviatoric part.

$$\begin{cases} K\left(\varepsilon_{kk}^{e}\delta_{ij}\right)=\sigma_{kk}^{e} \\ 2G\left(\varepsilon_{ij}^{e}-\frac{1}{3}\varepsilon_{kk}^{e}\delta_{ij}\right)=s_{ij} \end{cases} \tag{3.2}$$

3.2 Plastic framework

Plasticity of material could be caused by shear stress, creating volumetric expansion or contraction. Hydrostatic stress although cannot generates plastic strain, influences the development of plasticity, which must be taken into account in the elastoplastic constitutive model.

Geomaterials usually obey the non-associated flow rule (non-orthogonal flow rule), meaning that the inelastic incremental strain vector does not coincide with the normal to the yield surface. Increment constitutive relation in non-associated flow rule is

$$d\varepsilon_{ij}^{p}=d\lambda\frac{\partial Q}{\partial\sigma_{ij}} \tag{3.3}$$

where Q is the plastic potential function. Plastic strain increment could be decomposed into $d\varepsilon_{v}^{p}$ and $d\gamma^{p}$. Since the Lode angle (the 3rd stress tensor invariant is neglected, Equation (3.3) also can be rewritten as.

$$d\varepsilon_{ij}^{p}=d\lambda\left(\frac{\partial Q}{\partial\sigma_{m}}\frac{\partial\sigma_{m}}{\partial\sigma_{ij}}\delta_{ij}+\frac{\partial Q}{\partial\bar{\tau}}\frac{\partial\bar{\tau}}{\partial\sigma_{ij}}\right) \tag{3.4}$$

Where $\frac{\partial\sigma_{m}}{\partial\sigma_{ij}}=\frac{1}{3}\delta_{ij}$; $\frac{\partial J_{2}}{\partial\sigma_{ij}}=s_{ij}$,

$$\frac{\partial\bar{\tau}}{\partial\sigma_{ij}}=\frac{\partial\sqrt{J_{2}}}{\partial J_{2}}\frac{\partial J_{2}}{\partial\sigma_{ij}}=\frac{1}{2\sqrt{J_{2}}}s_{ij} \tag{3.5}$$

Then, the plastic strain increment is

$$d\varepsilon_{ij}^{p}=d\lambda\left(\frac{1}{3}\frac{\partial Q}{\partial\sigma_{m}}\delta_{ij}+\frac{1}{2\sqrt{J_{2}}}s_{ij}\frac{\partial Q}{\partial\bar{\tau}}\right) \tag{3.6}$$

Plastic volumetric strain increment $d\varepsilon_{v}^{p}=d\varepsilon_{ii}^{p}$

$$d\varepsilon_{v}^{p}=3d\lambda\frac{\partial Q}{\partial I_{1}} \tag{3.7}$$

Plastic shear strain increment,

$$d\bar{\gamma}^{p}=\sqrt{2de_{ij}^{p}de_{ij}^{p}};\ de_{ij}^{p}=d\varepsilon_{ij}^{p}-\frac{1}{3}d\varepsilon_{v}^{p}\delta_{ij}=d\lambda\frac{1}{2\sqrt{J_{2}}}s_{ij}\frac{\partial Q}{\partial\bar{\tau}}$$

$$d\bar{\gamma}^{p}=d\lambda\frac{\partial Q}{\partial\bar{\tau}} \tag{3.8}$$

To facilitate drawing, in figures $\bar{\tau}$ and $\bar{\gamma}^{p}$ are replaced with τ and γ^{p}, respectively.

3.3 Parameter determination

Plastic deformation development is influenced by hydrostatic pressure as well as loading history. The plastic potential Q and yield F functions are assumed to be functions of I_1 and plastic equivalent shear strain $\bar{\gamma}^p$ [82-84].

$$\begin{cases} Q = \bar{\tau} - Q_1(I_1, \bar{\gamma}^p) \\ F = \bar{\tau} - F_1(I_1, \bar{\gamma}^p) \end{cases} \tag{3.9}$$

The flow rule read then

$$d\bar{\gamma}^p = d\lambda \tag{3.10a}$$

$$d\varepsilon_v^p = 3d\lambda \frac{\partial Q_1}{\partial I_1} \tag{3.10b}$$

$d\lambda$ is plastic factor, a nonnegative scalar. Substitute equation 3.10a into 3.10b，

$$\beta = -\frac{d\varepsilon_v^p}{d\bar{\gamma}^p} = -3\frac{\partial Q_1}{\partial I_1} = g_1(I_1, \bar{\gamma}^p) \tag{3.11}$$

where β is the dilatancy factor (function). Positive dilatancy factor means volume increase, the negativefactor, means volume reduction or compaction.

3.3.1 Yield function

ε_{ax} and ε_{la} are axial strain and lateral strain. $\varepsilon_{ax} = \Delta L/L$; ΔL is the sample shortening measured during the tests, L is the length of the smaple. $\varepsilon_{la} = \Delta x/(2\pi R)$, Δx is the elongating of extensometer twining around the sample surface, R is the radius of the sample. Generilized shear strain and the plastic shear strain increment are calculated by

$$\bar{\gamma} = 2\sqrt{J'_2} = \frac{2}{\sqrt{3}}(\varepsilon_{ax} - \varepsilon_{la}) \tag{3.12}$$

$$d\bar{\gamma}^p = d\gamma - d\bar{\tau}/G \tag{3.13}$$

The strain hardening appears during the loading process. Yield stress changes with the hydrostatic stress and plastic shear strain. Taking the values of yield stress and hydrostatic stress at the same plastic shear strain, the relationship between yield stress and hydrostatic stress could be obtained. Then the (undetermined) coefficients in the different yield stress-hydrostatic stress relationships are written as the functions of plastic shear strain. Fig. 3.2 shows the relationships between yield stress and hydrostatic stress. Pure hydrostatic pressure also could yield rock. Therefore, the yield function does not take conventional linear form, but quadratic function.

$$\bar{\tau} = a(\bar{\gamma}^p){I_1}^2 + b(\bar{\gamma}^p)I_1 + c(\bar{\gamma}^p) \tag{3.14}$$

where，$a(\bar{\gamma}^p)$, $b(\bar{\gamma}^p)$ and $c(\bar{\gamma}^p)$ are functions related with $\bar{\gamma}^p$.

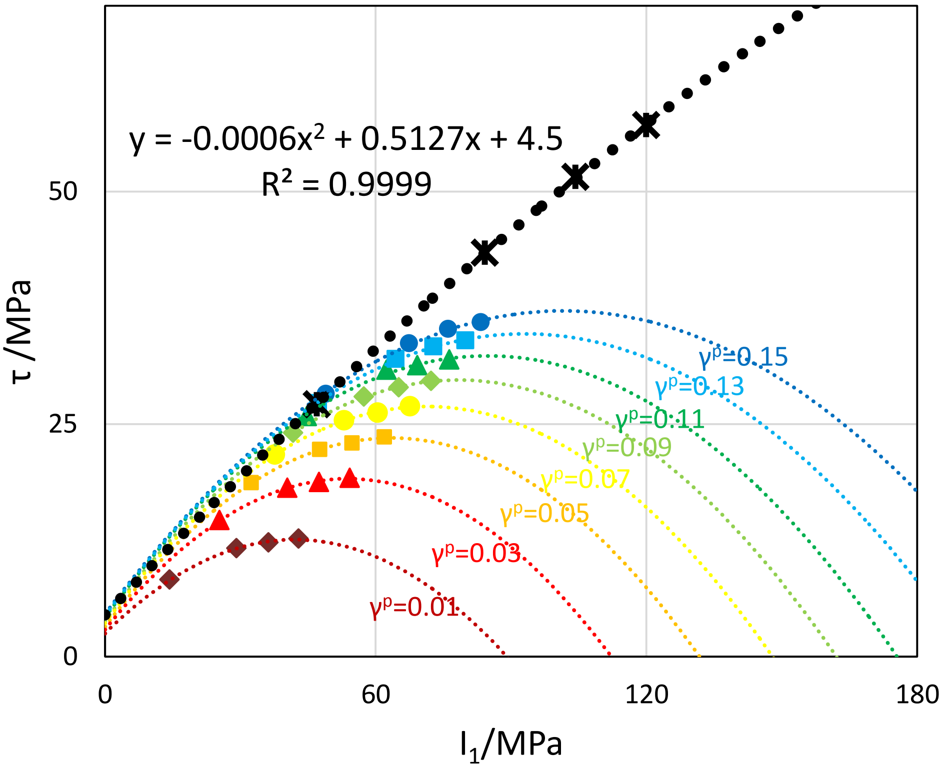

Fig.3.2 Relationship between yield stress and hydrostatic stress under different $\bar{\gamma}^p$. The quadratic function was employed in fitting the limited data from one uniaxial test and three triaxial tests, which has been shown in Section 2. The black cross represents the value where the samples fail.

$a(\bar{\gamma}^p)$, $b(\bar{\gamma}^p)$ and $c(\bar{\gamma}^p)$ take the values in Table 3.1。

Table3.1 Taking value for the functions $a(\bar{\gamma}^p)$, $b(\bar{\gamma}^p)$ and $c(\bar{\gamma}^p)$

$\bar{\gamma}^p$	$a(\bar{\gamma}^p)$	$b(\bar{\gamma}^p)$	$c(\bar{\gamma}^p)$
0.15	-0.0032	-0.6414	4.6
0.13	-0.0035	-0.6521	4.4
0.11	-0.0039	-0.6644	4.2
0.09	-0.0042	-0.6628	3.8
0.07	-0.0046	-0.6535	3.6
0.05	-0.005	-0.6401	3.2

$\bar{\gamma}^p$	$a(\bar{\gamma}^p)$	$b(\bar{\gamma}^p)$	$c(\bar{\gamma}^p)$
0.03	-0.0056	-0.6034	2.9
0.01	-0.0062	-0.4795	2.5

Fitting the values of $a(\bar{\gamma}^p)$, $b(\bar{\gamma}^p)$ and $c(\bar{\gamma}^p)$ to $\bar{\gamma}^p$, the functions are shown in Fig. 3.3.

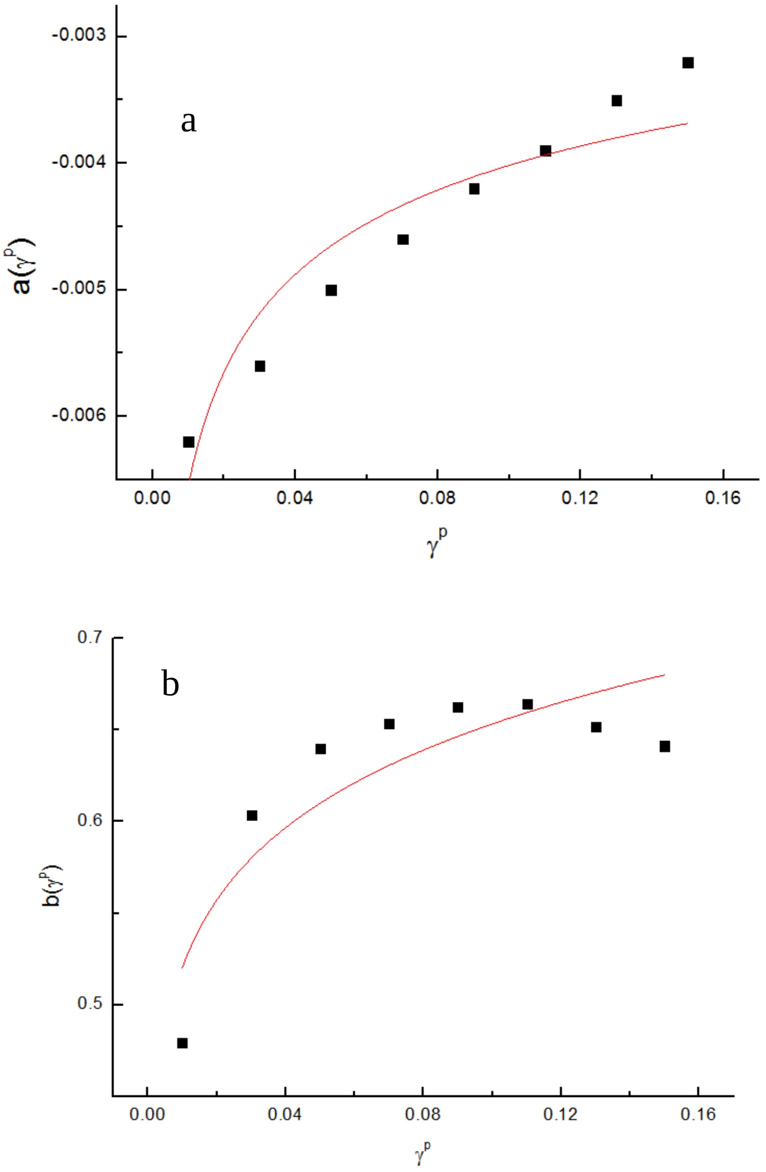

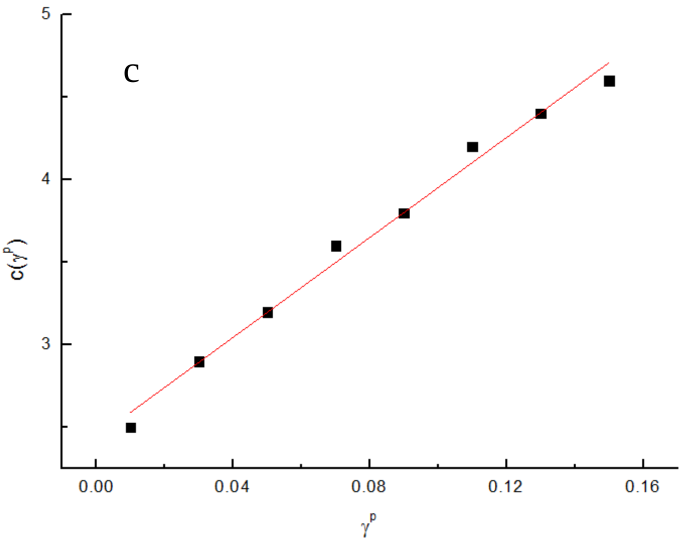

Fig.3.3 Fitting the parameters to obtain the function of $a(\bar{\gamma}^p), b(\bar{\gamma}^p)$ and $c(\bar{\gamma}^p)$.

By fitting the data, $a(\bar{\gamma}^p)$, $b(\bar{\gamma}^p)$ and $c(\bar{\gamma}^p)$ are obtained

$$\begin{cases} a(\bar{\gamma}^p) = -0.0025{\bar{\gamma}^p}^{0.21} \\ b(\bar{\gamma}^p) = 0.82{\bar{\gamma}^p}^{0.099} \\ c(\bar{\gamma}^p) = 30.238\bar{\gamma}^p + 2.4404 \end{cases} \tag{3.15}$$

Combining equation 3.10, 3.14, 3.15, the yield function is

$$F = \bar{\tau} - \left(-0.0025{\bar{\gamma}^p}^{0.21}\right){I_1}^2 - 0.82{\bar{\gamma}^p}^{0.099}I_1 - (30.238\bar{\gamma}^p + 2.4404) \tag{3.16}$$

3.3.2 Dilatancy function (plastic potential function)

Plastic potential function is defines the direction of incremental plastic deformation vector, or the value of dilatancy factor. Plastic volumetric strain is calculated as

$$\varepsilon_v^p = \varepsilon_{ax} + 2\varepsilon_{la} - \frac{K}{3}I_1 \tag{3.17}$$

As stated in chapter 1, point D (in Fig. 2.12~2.17) is the critical point, after which third dilatancy mechanism (microcracks) would take effect and the volume expands exponentially. Fitting the corresponding values of D points with R ^{2}= 0.9877, obtain

$$\sqrt{J_2} - 0.3I_1 = 9.3 \tag{3.18}$$

To simplify the model, the critical point is neglected. In Fig. 3.4, the relationship between dilatancy factor and hydrostatic pressure is linear as $\bar{\gamma}^p$ is unchanged.

$$g = \beta + m(\bar{\gamma}^p)I_1 + n(\bar{\gamma}^p) \tag{3.19}$$

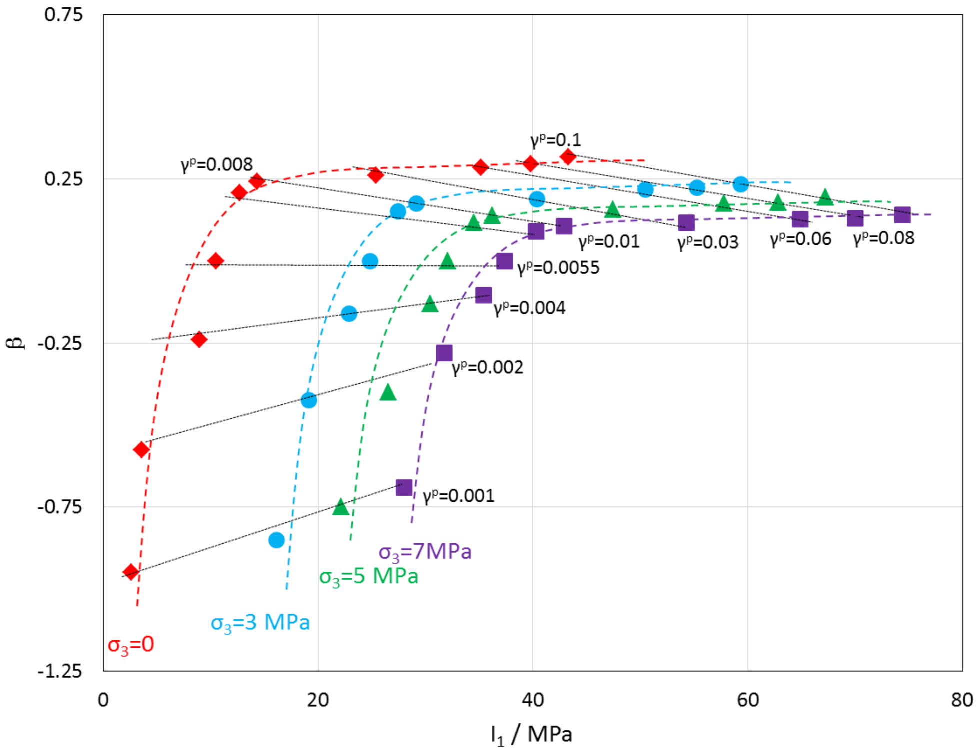

Fig.3.4 Dependence of dilatancy factor on plastic shear strain and hydrostatic pressure.

$m(\bar{\gamma}^p)$ and $n(\bar{\gamma}^p)$ are the function of $\bar{\gamma}^p$, whose taking values are in Table 3.2。

Table3.2 Taking value for the functions $m(\bar{\gamma}^p)$, $n(\bar{\gamma}^p)$

$\bar{\gamma}^p$	$m(\bar{\gamma}^p)$	$m(\bar{\gamma}^p)$
0.1	-0.0109	1.1112
0.08	-0.0107	1.0242
0.06	-0.0104	0.945
0.03	-0.01	0.899
0.01	-0.0096	0.6253
0.009	-0.0084	0.5237
0.0055	0	0
0.004	0.00128	-0.6005

$\bar{\gamma}^p$	$m(\bar{\gamma}^p)$	$m(\bar{\gamma}^p)$
0.002	0.0327	-1.3445
0.001	0.0474	-2.1556

The expressions of $m(\bar{\gamma}^p)$ and $n(\bar{\gamma}^p)$ are obtained by fitting. The fitting results are shown in Fig. 3.5.

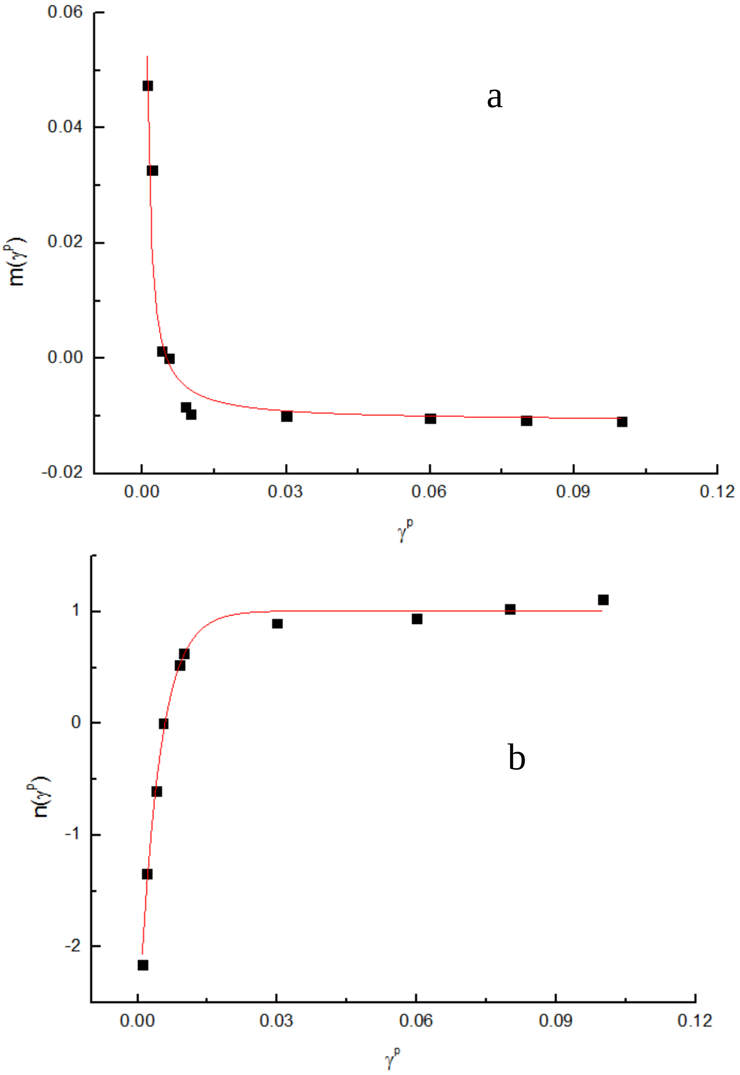

Fig.3.5 Fitting the parameters to obtain the function of $m(\bar{\gamma}^p)$, $n(\bar{\gamma}^p)$.

$m(\bar{\gamma}^p)$ and $n(\bar{\gamma}^p)$ are

$$\begin{cases} m(\bar{\gamma}^p) = -0.0109 + \frac{0.0000536}{\bar{\gamma}^p - 0.000154} \\ n(\bar{\gamma}^p) = 1.12 - \frac{0.00791}{\bar{\gamma}^p + 0.00136} \end{cases} \tag{3.20}$$

Combining equation 3.10, 3.11b，3.19, 3.20, the dilatancy function is obtained

$$g = \beta - \left(-0.0109 + \frac{0.0000536}{\bar{\gamma}^p - 0.000154}\right) I_1 - 1.12 + \frac{0.00791}{\bar{\gamma}^p + 0.00136} \tag{3.21}$$

The black cross in Fig. 3.2 represents the strength under different confining pressure. By fitting, the breaking strength function is obtained

$$F = \bar{\tau} + 0.0006\, {I_1}^2 - 0.5127 I_1 - 4.5 = 0 \tag{3.22}$$

3.4 Comparison of constitutive model to experimental data

Since the parameters are determined by fitting the experimental data, it is meaningless to verify the model by the used experimental data. This section will compare the constitutive model and the measured data in chapter 2 and show the difference.

3.4.1 Yield function

Plot of the yield function (3.16) is shown in Fig. 3.6. This figure intuitively shows the change in yield stress over plastic shear strain. In physics, the model includes the strain hardening.

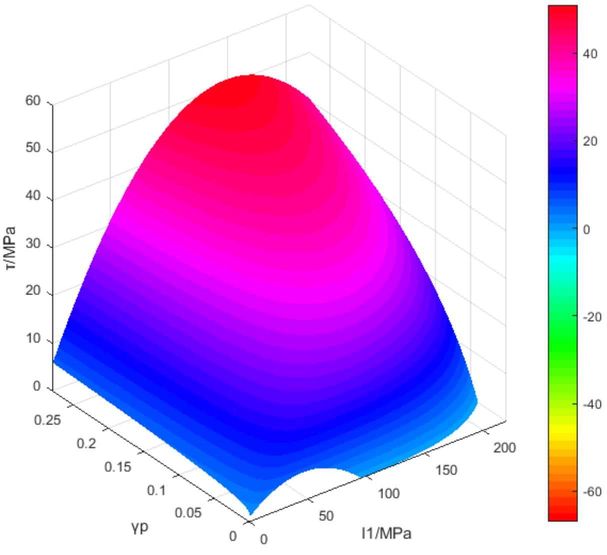

Fig.3.6 Yield Function in stress space.

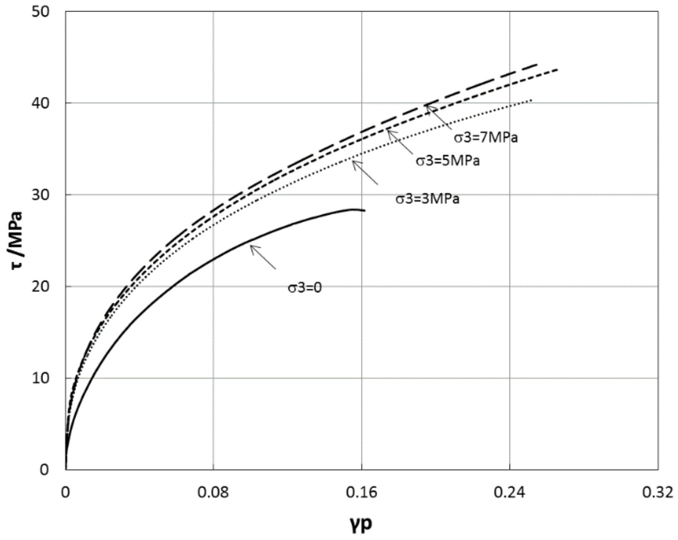

Fig.3.7 Yield Function measured in compression test with different confining pressure.

Within the range of the measuring device, the measured maximal yield stress (Fig. 3.7) are 28.3 MPa ($\bar{\gamma}^p = 0.15, \sigma_3 = 0\text{MPa}$), 39.7MPa ($\bar{\gamma}^p = 0.24, \sigma_3 = 3\text{MPa}$), 42.1MPa ($\bar{\gamma}^p = 0.24, \sigma_3 = 5\text{MPa}$) and 43.3MPa ($\bar{\gamma}^p = 0.24, \sigma_3 = 7\text{MPa}$). Plotting the loading path on the yield surface (Fig. 3.8), the maximal yield stress predicted by model are 26.5MPa, 39.2MPa, 41.9MPa and 42.9MPa respectively. The relative error between the two are 6.4%、1.3%、0.5%, 1.2%。

Uniaxial compression experimental results are easily affected by defects of samples, and have a relatively high random error. The results obtained from model are consistent with those from triaxial compression tests, indicating the model have good quality of describing the yield stress of salt, to some degree.

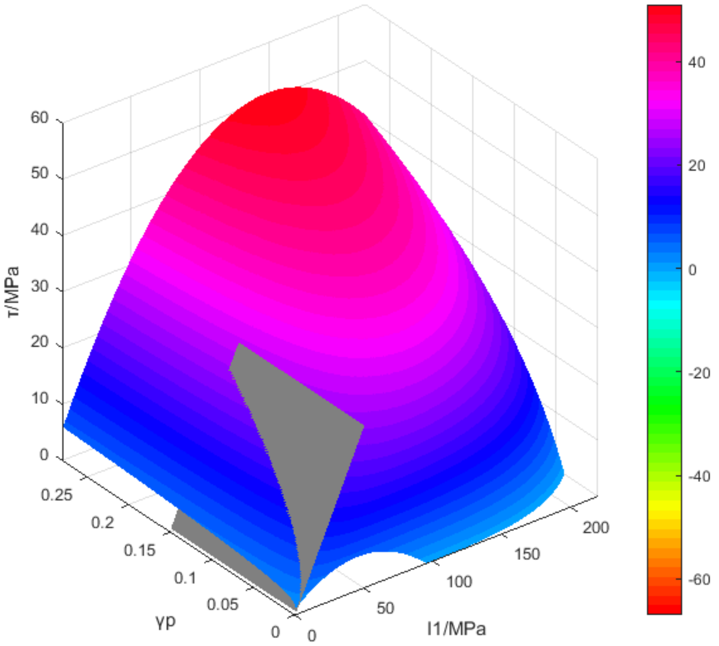

(a) $\sigma_3 = 0\text{MPa}$

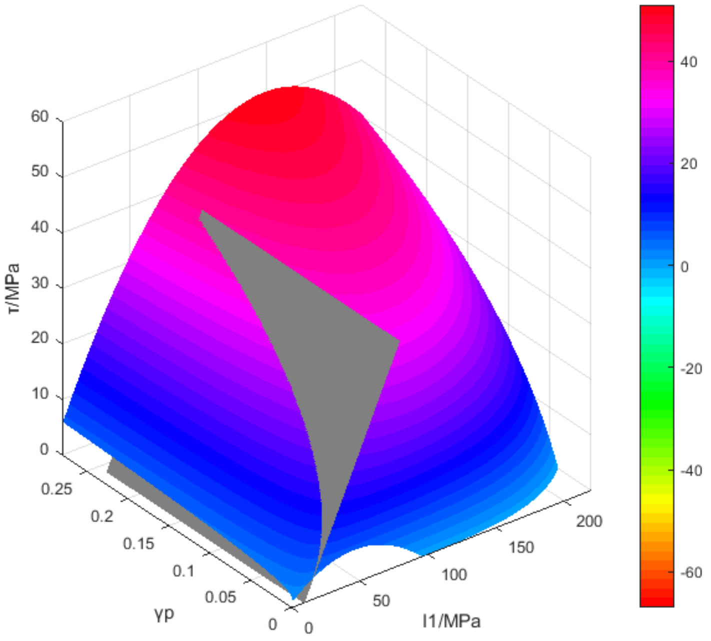

(b) $\sigma_3 = 3\text{MPa}$

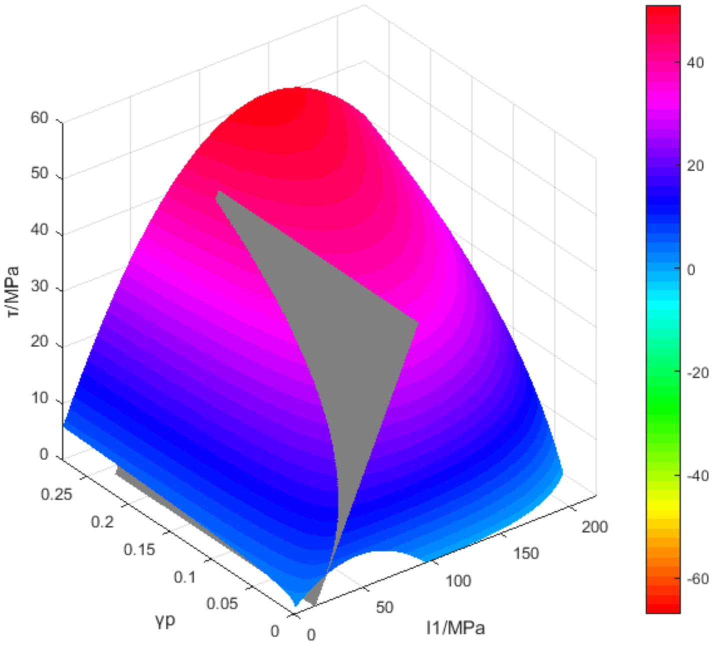

(c) $\sigma_3 = 0\text{MPa}$

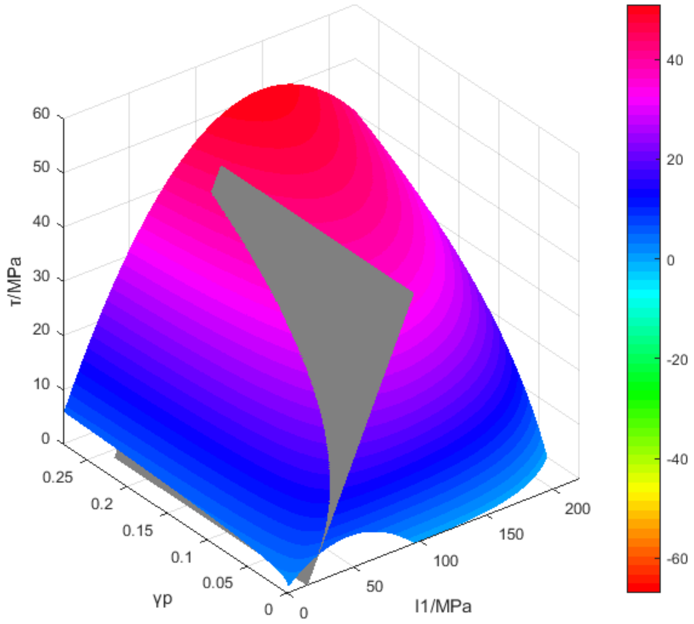

(d) $\sigma_3 = 7\text{MPa}$

Fig.3.8 Yield surface and loading path in stress space.

3.4.2 Dilatancy function

It is shown in section 2.3.2 that the inelastic volumetric strain increases quasi-linear with the axial strain before the critical point (in composite stage and plastic stage), that means the dilatancy factor is constant. The plot of dilatancy function from equation (3.21) is shown in Fig. 3.9. This factor first rapidly increases from negative to positive values and becomes constant. If the hydrostatic pressure is larger, the dilatancy factor is smaller.

Comparing Fig. 3.10 with Fig. 3.4, the dilatancy factor predicted by model are almost the same with that form experimental results. One point need note is that this model could describe three stages before critical point. In the future research, the data after critical point will be added and the model will be improved.

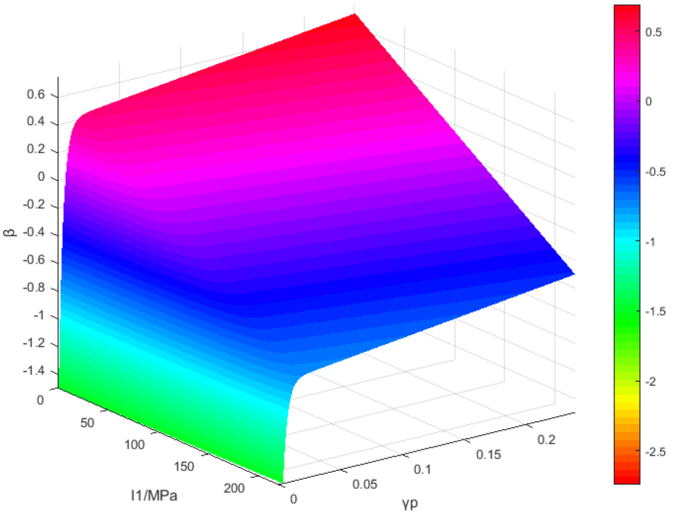

Fig.3.9 Dilatancy factor *vs* plastic shear strain and hydrostatic pressure.

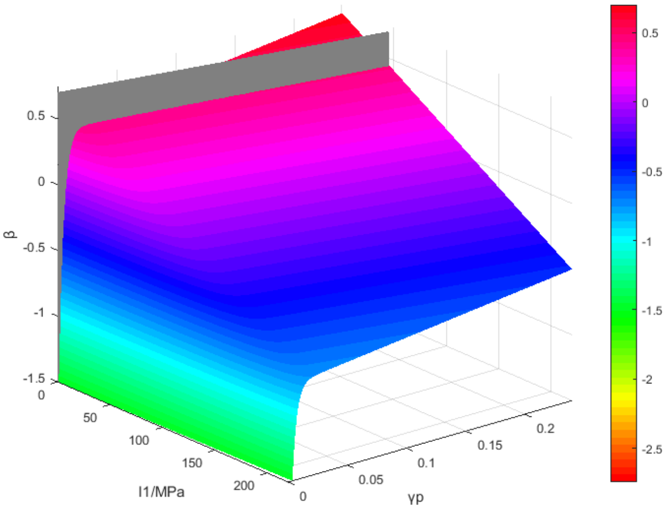

(a) $\sigma_3 = 0\text{MPa}$

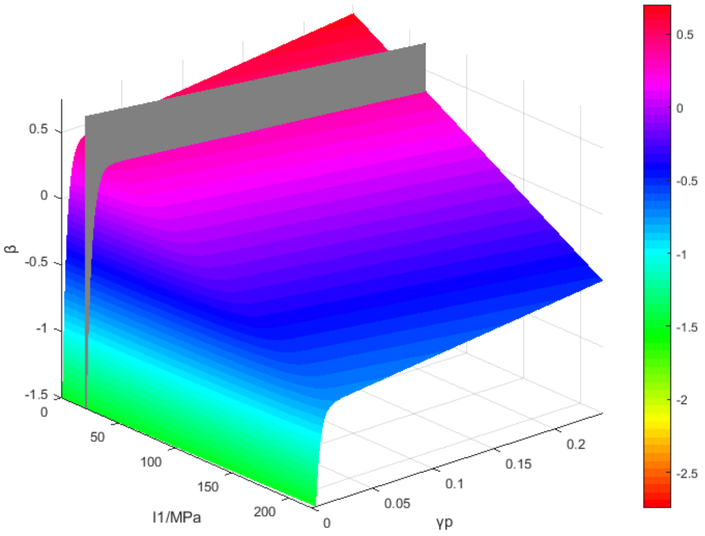

(b) $\sigma_3 = 3\text{MPa}$

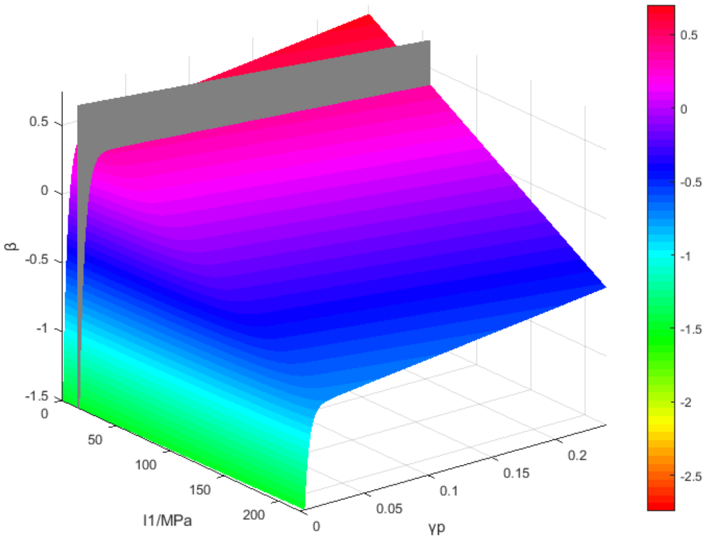

(c) $\sigma_3 = 5\text{MPa}$

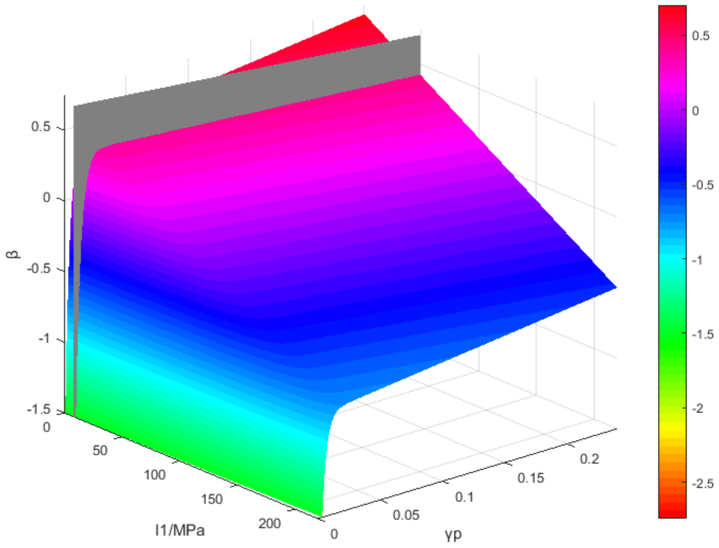

(d) $\sigma_3 = 7\text{MPa}$

Fig.3.10 Dilatancy function and loading path in stress-strain space.

3.5 Chapter summary

This chapter transforms plastic potential function into dilatancy function, simplifying the formulation of plastic constitutive model. Considering the effect of hydrostatic stress and loading history, the yield function F based on the form of quadratic function and dilatancy function bases on the linear function are developed. The consitituve model could describe the strain hardening effect.

$$F = \bar{\tau} - \left(-0.0025{\bar{\gamma}^{p}}^{0.21}\right){I_1}^2 - 0.82{\bar{\gamma}^{p}}^{0.099} I_1 - (30.238\bar{\gamma}^{p} + 2.4404) \quad (3.23a)$$

$$g = \beta - \left(-0.0109 + \frac{0.0000536}{\bar{\gamma}^{p} - 0.000154}\right) I_1 - 1.12 + \frac{0.00791}{\bar{\gamma}^{p} + 0.00136} \quad (3.23b)$$

Based on the experiemental results, the failure criteria for salt was also developed, laying a fundament for furture data simulation.

$$F = \bar{\tau} + 0.0006\,{I_1}^2 - 0.5127 I_1 - 4.5 = 0 \quad (3.23c)$$

4 Conventional fatigue and constitutive model for salt

The basic mechanical properties were investigated previously, providing useful data for the further investigation into the fatigue. This chapter will investigate the conventional fatigue properties of salt with different stress limits, temperature, loading velocity and confining pressure under continuous cyclic loading. Based on these data, the constitutive model will be modified to take into account the fatigue behavior of salt.

4.1 Experimental design

The samples and the device used in the fatigue tests are the same as in the previous experiments. The experimental scheme is the following:

These series of fatigue tests are uniaxial or triaxial cyclic loading tests. Considering the compression strength obtained before, upper and lower stress limits are determined to conduct the fatigue tests. The tests are divided into 4 groups named 1201a group, 1201b group, 1201c group and 1201d group, to investigate the stress effect, loading velocity effect, temperature effect and confining pressure effect, respectively. 1201a group have two subgroups, 1201a1 and 1201a2, for upper stress limit and lower stress limit. All the tests adopt the velocity of 0.2KN/s to load to the target stress, then apply the designed velocity.

1201a1 group tests hold the lower stress limit constant, 9.4MPa, 20% of the uniaxial compression strength; upper stress limit is 95%, 90%, 85%, 80% of the uniaxial compression strength. Room temperature is 25±2℃; Air humidity is 57±5%; Loading velocity is 2KN/s.

1201a2 group tests hold the upper stress limit constant, 90% of the uniaxial compression strength; lower stress limit is 20%, 30%, 40%, 50% of the uniaxial compression strength. Room temperature is 25±2℃; Air humidity is 57±5%; loading velocity is 2KN/s.

1201b group tests hold the upper and lower stress limit constant, 90% and 20% of the uniaxial compression strength, respectively. Room temperature is 25±2℃; Air gumidity is 57±5%; loading velocity is 0.36KN/s, 1KN/s, 3KN/s, 5KN/s, 7KN/s, 10KN/s.

1201c group tests hold the upper and lower stress limit constant, 90% and 20% of the uniaxial compression strength, respectively. Air humidity is 57±5%; loading velocity is 2KN/s; Room temperature is 13，30, 60℃.

1201d group tests are triaxial cyclic loading tests. The confining pressure is 3MPa and 5MPa. Upper and lower stress limit are 90% and 20% of the relevant compression strength. Room temperature is 25±2℃; Air humidity is 57±5%; loading velocity is 2KN/s.

4.2 Fatigue properties under different conditions

4.2.1 Stress limit effect

Stress ratio is the ratio of the stress limit (the maximum stress or minimum) to the strength. The effect of stress limit on the fatigue has been investigated by many authors. Here just briefly verify the effect on salt fatigue. In 1201a1 group, as the upper (stress) limit decreases from 95% to 90%, 85% and 80%, the fatigue life increases from 26 to 68, 205 and 582 (Fig. 4.1), showing that the decreasing upper limit could augment the fatigue life with the lower limit constant.

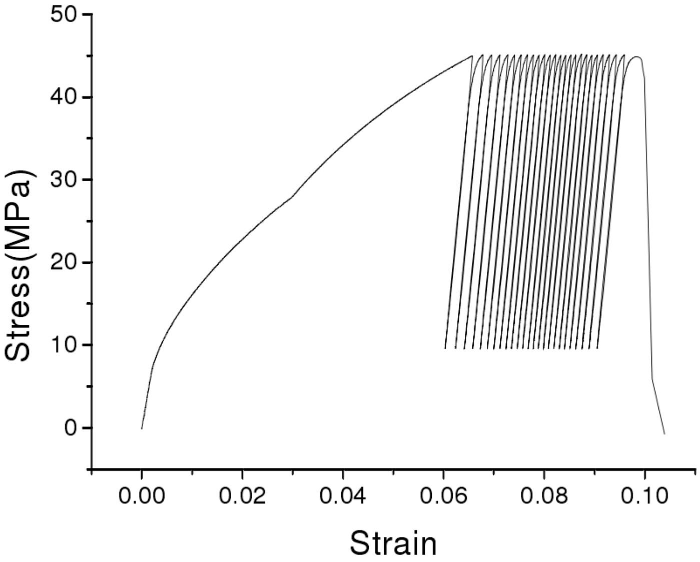

(a) Axial stress *vs* axial strain in cyclic loading test with 20%~95% stress limit

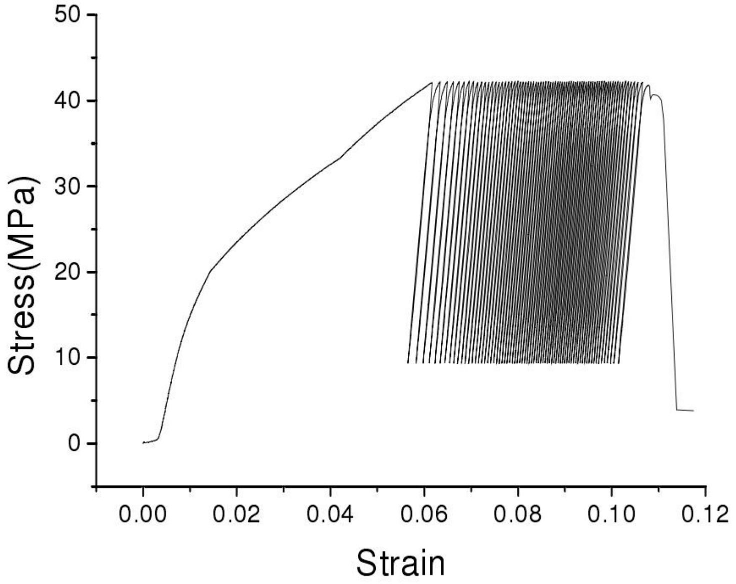

(b) Axial stress *vs* axial strain in cyclic loading test with 20%~90% stress limit

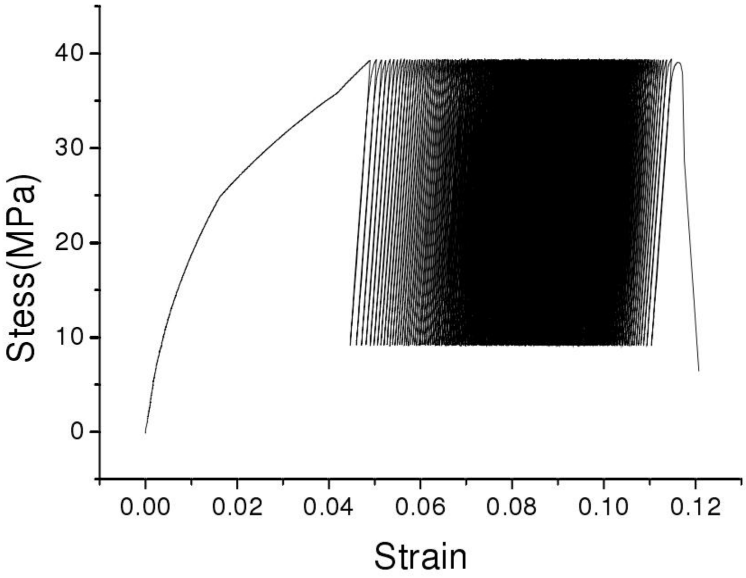

(c) Axial stress *vs* axial strain in cyclic loading test with 20%~85% stress limit

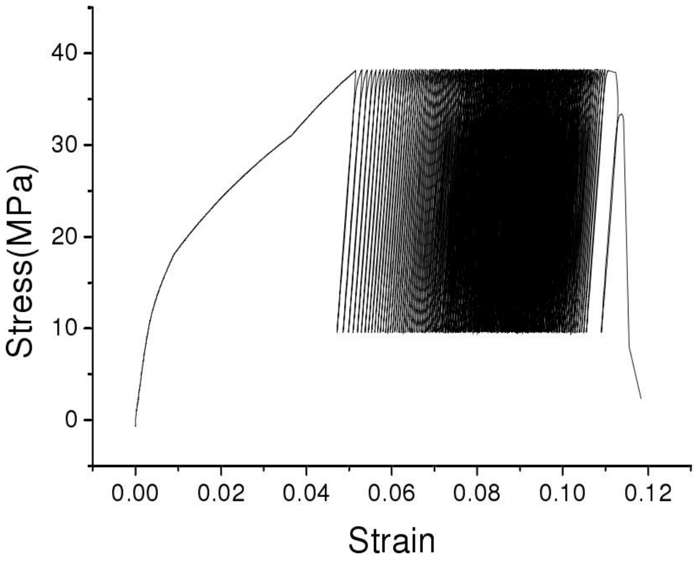

(d) Axial stress *vs* axial strain in cyclic loading test with 20%~80% stress limit.

Fig.4.1 Axial stress *vs* axial strain curves with different upper stress limits.

With the constant upper limit of 90%, the fatigue life changes from 68, to 85, 42 and 374, respectively, as the lower limit increases from 20% to 30%, 40% and 50%. As an overall trend, the fatigue life augments with the lower limit reduction. It can be found from the loading-unloading curves that the yield stress in the reloading process is close to previous upper limit, 3~5 MPa below the upper limit stress. Since the lower limit just changes below the yield stress, the plastic deformation should not show any difference. In my opinion, the fatigue life changes for other than the yield stress reason. In subsequent section, the reason will be revealed.

One point need note is that the total deformation of sample of 1201a2 group is in positive relation with fatigue life. 68 to 11.6%, 85 to 12.3%，42 to 9.1%，374 to 14.1%.

4.2.2 Loading velocity effect

Numerous researches show that loading frequency could enhance the rock sample’s strength, thus augment the fatigue life. However, within our testing range, the loading frequency has no remarkable effect on the salt fatigue. In 1201b group, loading velocity increases from 0.36KN/s to 10KN/s, the fatigue life just fluctuates slightly.

The experimental results are shown in Table 4.1. In this group the fatigue life does not show any obvious and direct dependence on the loading velocity. As a whole trend, experimental time roughly increases with the decreasing loading velocity which due to salt creep .

Table 4.1 Fatigue lives of salt under different loading velocities.

Loading rate (KN/s)	Cycle number	Total strain (%)	Total time (s)
10	32	9.5	2300
7	20	8.8	2000
5	23	10	2300
3	49	9.5	5000
1	23	10.4	5200
0.36	38	12	18000

4.2.3 Temperature effect

Every uniaxial compression test with different temperature is conducted more than three times. The results show that the temperature exerts a notable influence on the salt compression strength. As shown in Fig. 4.2, the strength reduces from 47.1MPa to 40MPa with the temperature increasing from 13℃ to 60℃.

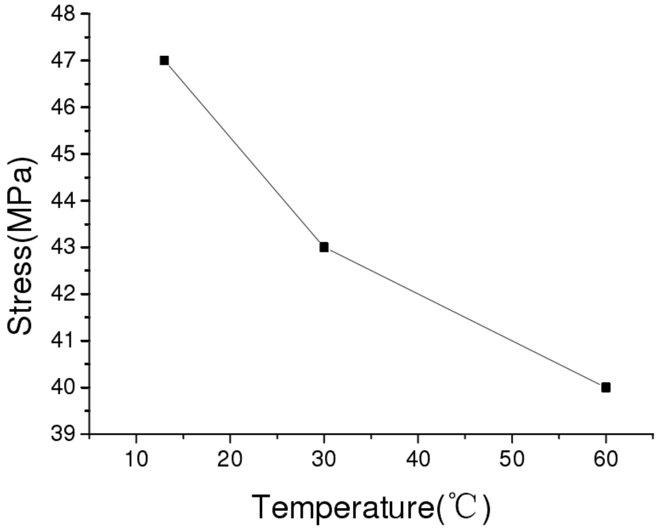

Fig.4.2 Uniaxial compression strength at different temperature.

In 1201cgroup, the upper and lower limits of cyclic load are 90% and 20% of the strength. As the temperature increases, fatigue lives of salt increases as well. At 13℃, 8 cycles are completed. At 30℃ and 60℃, the fatigue lives are 37 and 45 respectively. The main reason why the fatigue life of salt rises is that the viscidity and tenacity enhance with the temperature increase.

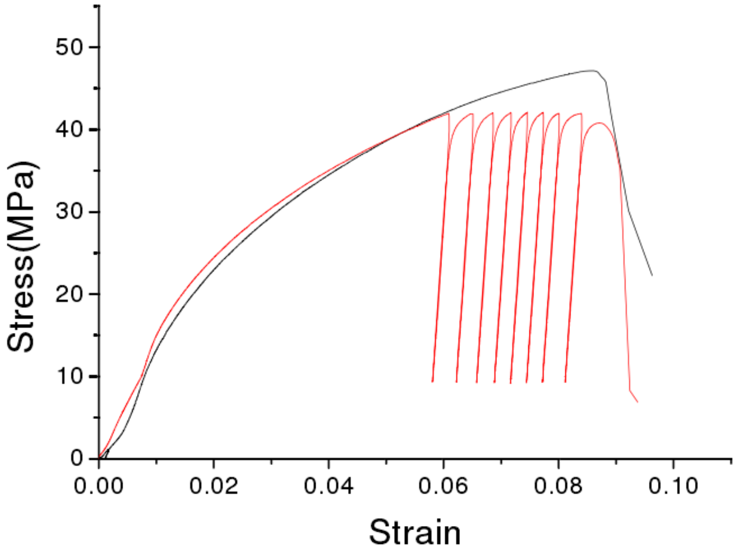

(a) Cyclic loading-unloading test at 13℃

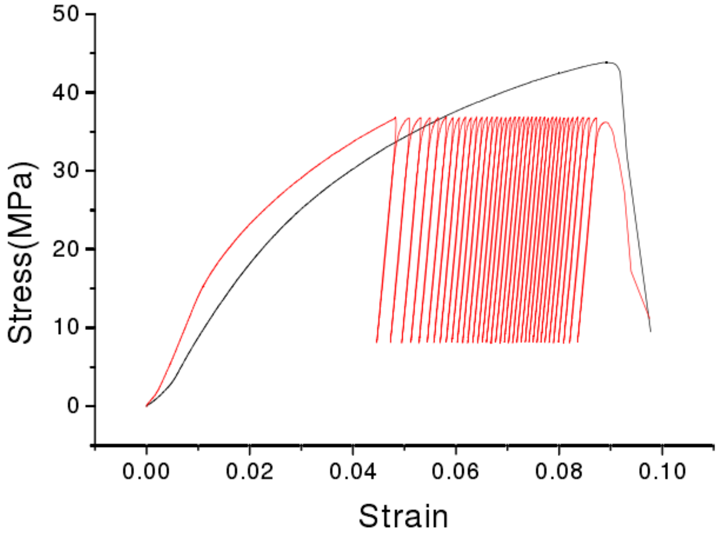

(b) Cyclic loading-unloading test at 30℃

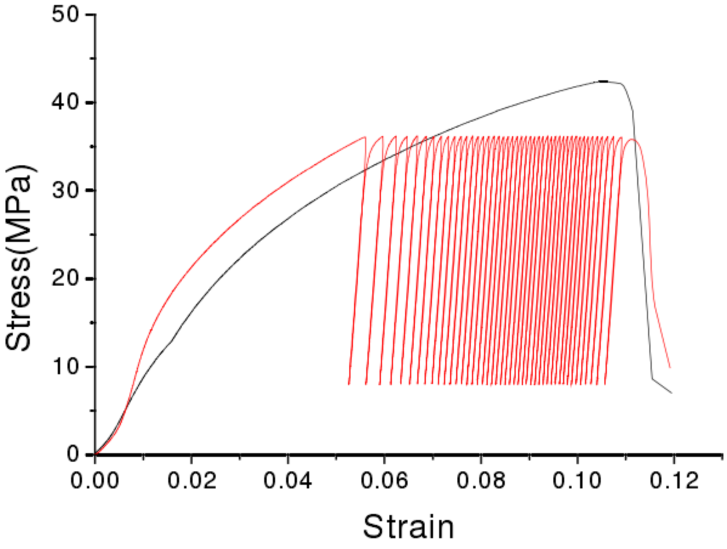

(c) Cyclic loading-unloading test at 60℃

Fig.4.3 Axial stress-axial strain curves from uniaxial compression and fatigue tests at different temperature.

4.2.4 Confining pressure effect

The strength of salt increases with the mean stress or confining pressure. For the salt, the confining pressure enhances the deformability as well. As shown in Fig. 4.4, the compression strength increases from 47.1MPa to 89.3MPa and the total deformation prior the failure increases from 8.92% to 25.3%. However, it is unclear whether the confining pressure could influence the salt fatigue for the same stress ratio, . 1201d group is to work out this.

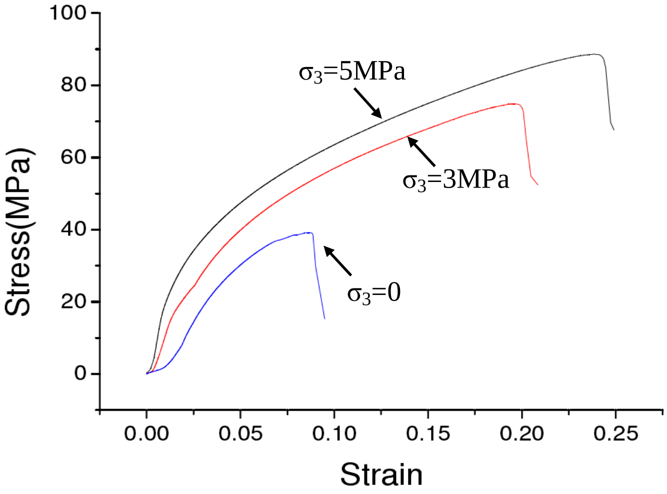

Fig.4.4 Axial stress-axial strain curves from compression test at different confining pressure.

The fatigue life shows a significant enhancement with the confining pressure increase. As the confining pressure rises from 0 to 3MPa and 5MPa, fatigue life augments from 34 to 62 and 103, respectively. Fig. 4.5 combines the relevant compression curve with the cyclic loading curve. It can be found that the fatigue failure point deviates from the compression test further as the confining pressure rises. This is caused by the enhanced rheological property and subdued brittleness.

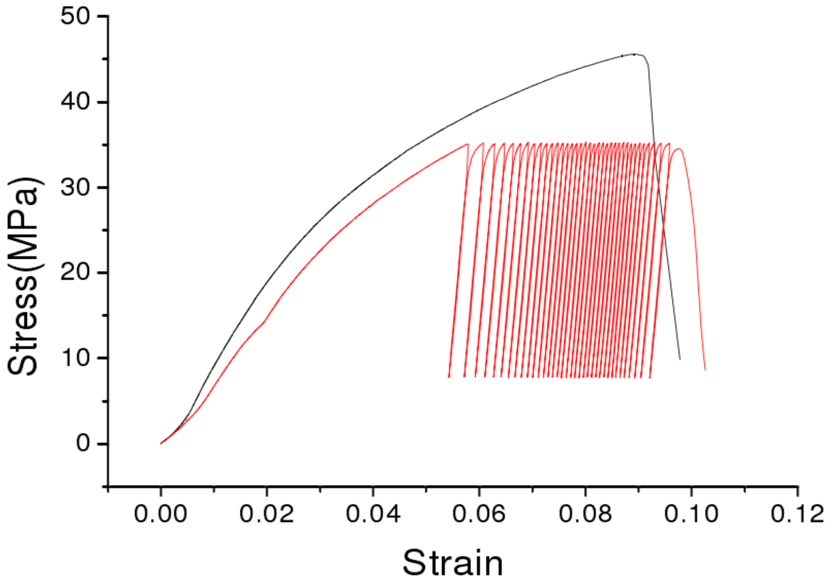

(a) Axial stress vs axial strain in cyclic loading test with 0MPa confining pressure

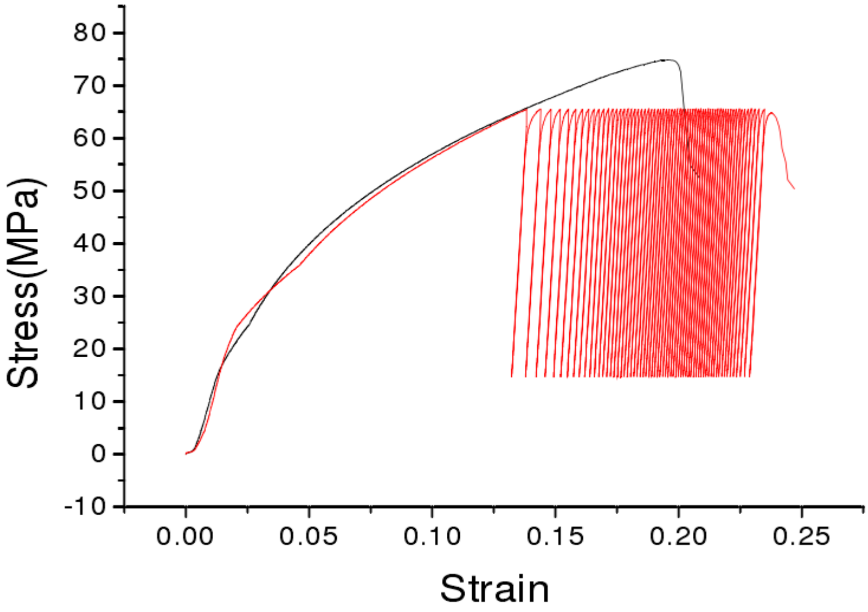

(b) Axial stress vs axial strain in cyclic loading test with 3MPa confining pressure

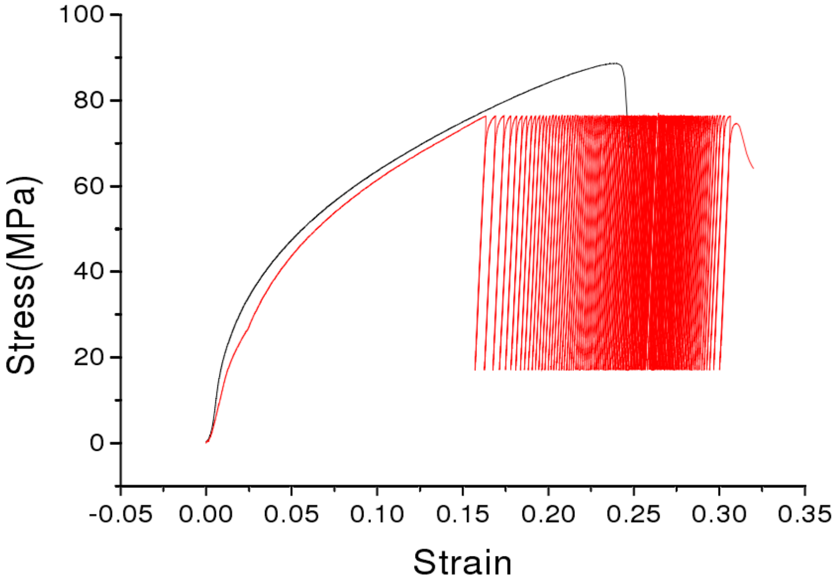

(c) Axial stress *vs* axial strain in cyclic loading test with 5MPa confining pressure

Fig.4.5 Axial stress-axial strain curve from fatigue tests at different confining pressure.

4.3 Fatigue life model based on energy dissipation

The product of stress and time is defined as stress energy E_w, in stress unloading-loading cycle

$$E_w = (T_1 + T_2)\sigma_{min} + \frac{T_1+T_2}{2}\Delta\sigma \tag{4.1}$$

T_1 and T_2 are the loading time and unloading time, σ_{min} is lower stress limit, $\Delta\sigma$ is stress ampulitude. Loading with constant velocity,

$$T_1 = T_2 = \frac{\Delta\sigma}{v} \tag{4.2}$$

Substitute equation (4.2) into equation (4.1),

$$E_w = 2\sigma_{min}\frac{\Delta\sigma}{v} + \frac{(\Delta\sigma)^2}{v} \tag{4.3}$$

There are three stages in fatigue deformation: decelerating deformation stage, uniform deformation stage and accelerating stage. If the stress ratio is smaller, the uniform deformation stage amounts for a greater proportion of total deformation. In uniform deformation stage, every residual strain keeps roughly constant. Supposed that the average strain rate is $\dot{\varepsilon}^p$, plastic work density ΔW^p is

$$\Delta W^p = E_w\dot{\varepsilon}^p \tag{4.4}$$

Through *N-S* curve, it can be found that the relationship between fatigue and plastic work density is

$$N_f(k\Delta W^p)^{\varsigma} = C \tag{4.5}$$

k is viscocity coefficient, ς is material parameters. Mark $Ck^{-\varsigma} = A_n$

$$N_f \Delta W^{p^{\varsigma}} = A_n \tag{4.6}$$

Equation (4.6) is the fatigue life model based on plastic work.

Plastic strain rate is a physical quantity sensitive to stress state. Assuming that the average plastic strain rate is a function of $\dot{\varepsilon}^p$,

$$\dot{\varepsilon}^p = \dot{\varepsilon}^p(R_{max}, R_{min}) \tag{4.7a}$$

Because E_w is determined, ΔW^p is expressed as the function of R_{max}, R_{min}.

$$\Delta W^p = \Delta W^p(R_{max}, R_{min}) \tag{4.7b}$$

By fitting data, ΔW^p could be obtained. As shown in Fig. 4.6, the relationship of fatigue life and upper stress limit is exponential function. Viscocity coefficient of rock usually is 10^{19}~10^{23}Pa.s. Here taking 10^{20}Pa.s for the viscosity coefficient, $C = 11.45 \times 10^{352.2}$, $\varsigma = 17.61$.

$$N_f(kR_{max})^{\varsigma} = C \tag{4.8}$$

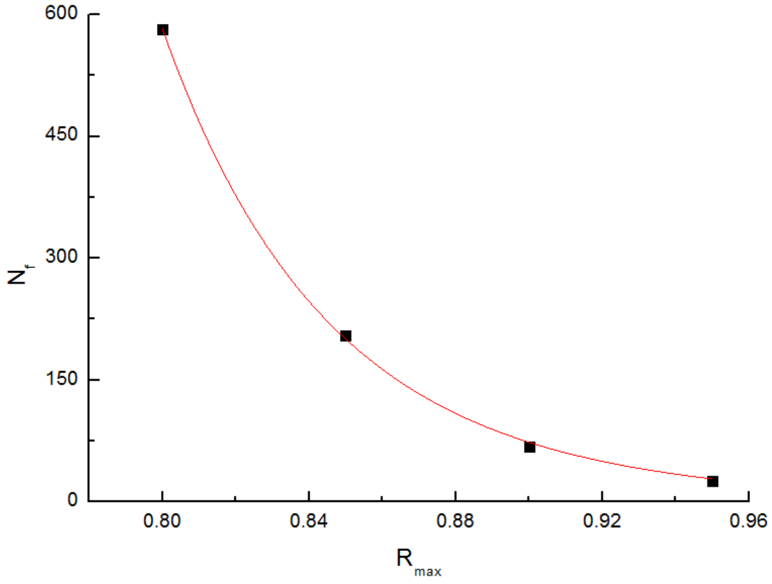

Fig.4.6 N-S curve under different upper limit stress.

In this model, temperature and confining pressure can change the fatigue life through the viscosity coefficient.

4.4 Fatigue constitutive model

4.4.1 Phenomenon of strain hardening and self-weakening

As mentioned in Chapter 2, salt shows strong plastic property and strain hardening phenomenon. The microscopic source of strain hardening is the proliferation and piling up of dislocations. The shear stress is needed to drive the dislocation. If the dislocations are more numerous, the needed for yielding shear stress is larger. Once the dislocations are impeded at the obstacles, the number of piled-up dislocations increases and the shear stress increases.

During cyclic loading, the yield stress in the process of reloading is lower than that before unloading. This phenomenon is temporarily called here as self-weakening. At different confining pressure, 0MPa, 3MPa and 5MPa, the curves of self-weakening are similar with each other (the stress ratio is 20%~90%). In Fig. 4.8, red parts in each subplot representing the plastic phase in the reloading are the same in terms of the shape and trend, different in the scale or dimension. This indicates that the self-weakening is nearly the same with different confining pressure and stress ratio.

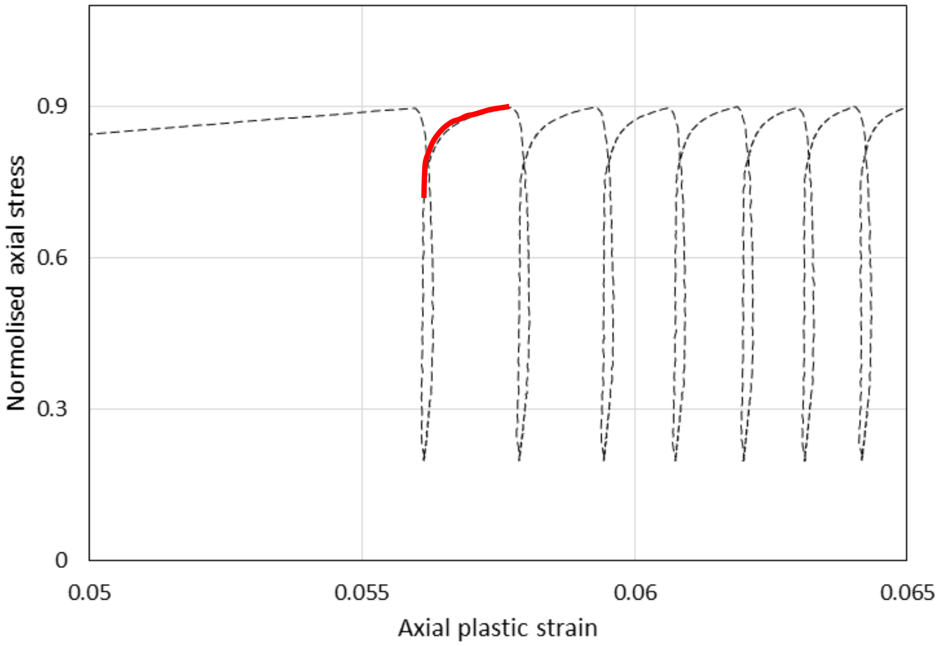

(a) Confining pressure = 0MPa

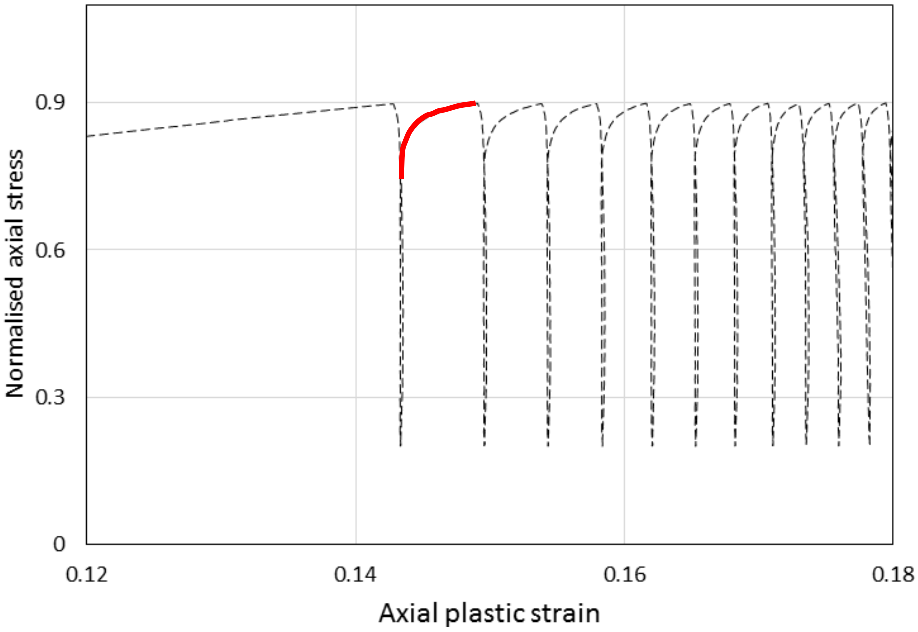

(b) Confining pressure = 3MPa

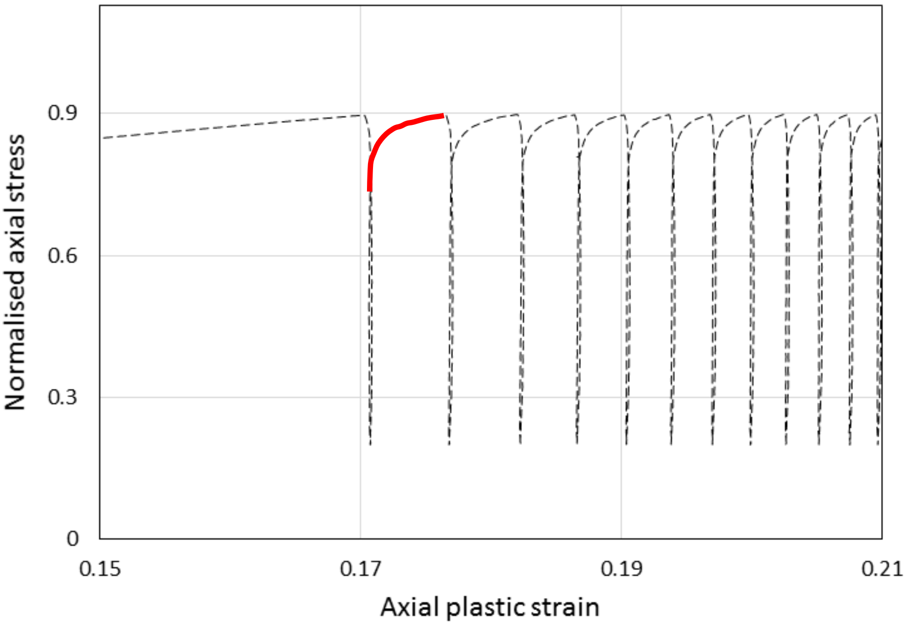

(c) Confining pressure = 5MPa

Fig. 4.7 Axial stress-plastic axial strain curve from compression fatigue tests.

The cause of the self-weakening is: the dislocations disperse under the mutual repulsive force and residual stress, resulting in the dislocation density decrease. Due to the smaller dislocation density, the mutual repulsive force is weaker, the dislocation could move beforehand during reloading, thus the yield comes earlier than before. Therefore the self-weakening happens.

After the stress reaches or exceeds the previous value in the last cycle, the degree of dislocation piling-up would grow up again to the level as before; so does the degree of hardening, which means the stress-strain curve would be the same as before (Fig. 4.8). Fig. 4.8 combines the stress-strain curve from uniaxial compression test (dense dotted line) and from one cycle unloading test (marked 1503 test). The two tests have the same experimental conditions. In the 1503 unloading test, the unloading point is 55% of the strength. During the reloading, the sample yields at the 41% of the strength, “recovery” at 63% of the strength.

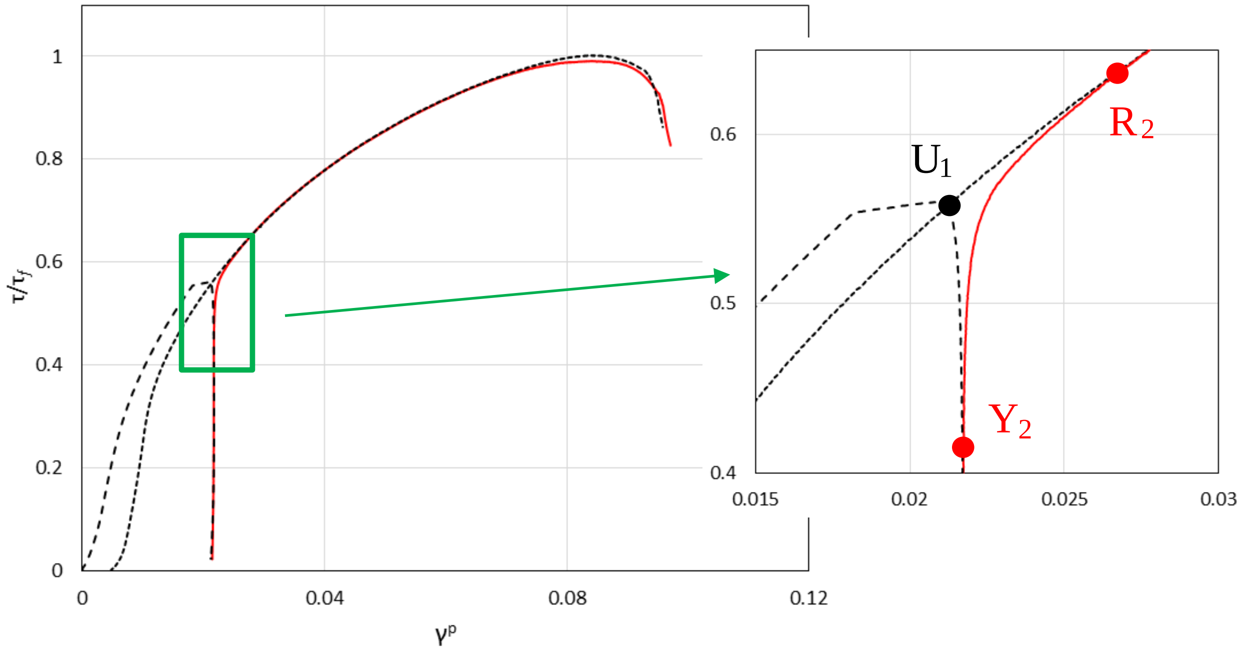

Fig. 4.8 Shear stress-plastic shear strain curve of uniaxial compression test and unloading test.

4.4.2 Yield function in reloading

Weakening coefficient χ_{f_2} is introduces to characterize the difference between the two curves in YR segment in Fig. 4.9, 2 representing the second stress cycle

$$\chi_{f_2} = \frac{\bar{\tau}_0 - \bar{\tau}_1}{\bar{\tau}_f} \tag{4.9}$$

$\bar{\tau}_0$ is the shear stress in reloading; $\bar{\tau}_1$ is the shear stress in uniaxial compression test; $\bar{\tau}_f$ is the shear strength.

χ_{f_2} is a function of the plastic deformation, taking the value between Y_2 and R_2. Ignoring the creep, the plastic deformation corresponding to Y_2 and U_1 should be the same. The plastic deformation corresponding to Y_2 is denoted as $\gamma^p_{(Y_2)}$. The values of χ_{f_2} changes with $\gamma^p_{YR} = \frac{\gamma^p - \gamma^p_{(Y_2)}}{\gamma^p_{(R_2)} - \gamma^p_{(Y_2)}}$, shown in Fig. 4.9

$$\chi_{f_2} = \chi_{f_2}(\gamma_{\mathrm{Y}R}^{p}) \tag{4.10}$$

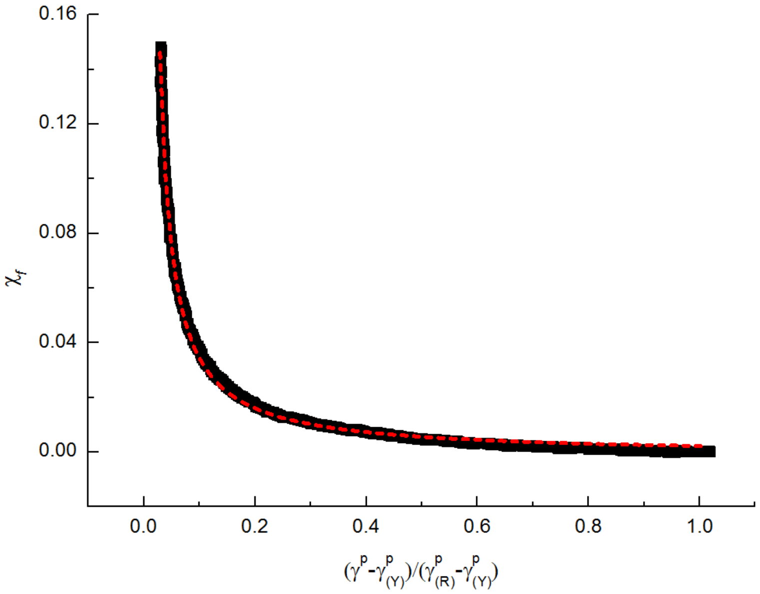

Fig. 4.9 Values taken by weakening parameter χ_{f_2}.

By fitting, χ_{f_2} obtain

$$\chi_{f_2} = -0.0011 + \frac{0.00332}{\gamma_{\mathrm{Y}R}^{p} - 0.00612} \tag{4.11}$$

The yield function in reloading is

$$F_2 = \frac{\bar{\tau}}{1-\chi_{f_2}} - F_1(I_1, \gamma^p) \tag{4.12}$$

4.4.3 Dilatancy function in reloading

Comparing the monotonous compression test and cyclic loading test, the dilatancy factor does not show big difference. In every reloading, the factor fluctuates around a constant level (Fig. 4.10). At first, the fluctuation range is large, then lessen. On the whole, the dilatancy function of constitutive model in reloading can be considered to be the same as for the continuous loading.

However, if we look into more details, it can be found that the dilatancy factor actually is bigger in the beginning and then decreases to a constant. It is interesting that the plastic deformation develops due to the micro-cracking at the beginning of reloading and then due to the dislocations.

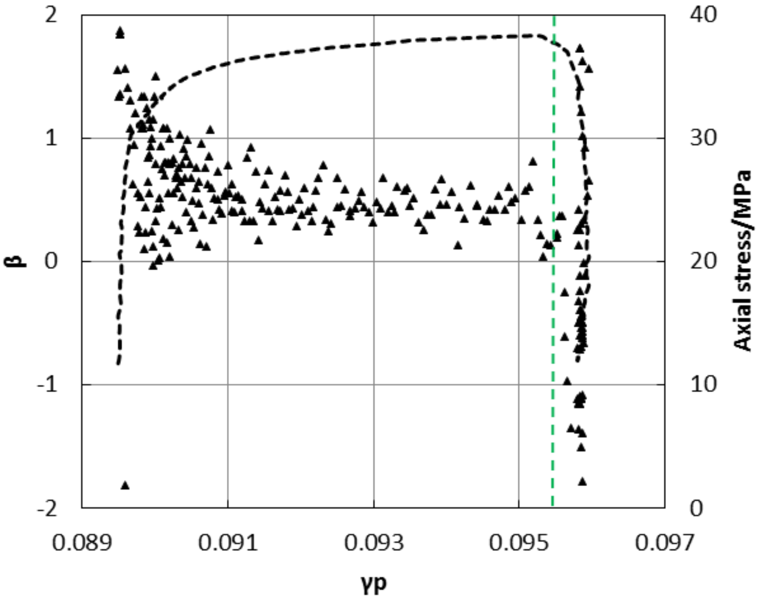

Fig. 4.10 Comparison of dilatancy factor between uniaxial test and fatigue test.

4.4.4 Strengthening coefficient and loosing zone

For the cyclic loading, no matter metal material or geomaterial both use dynamic model to modify the yield function [122-129]. The yield function in third loading could be considered as the translation of that in second loading, and so on. Therefore, the yield function in cyclic loading is

$$F_i = \frac{\bar{\tau}}{1-\chi_{f_i}} + R_f - f\left(I_1, \gamma^p - \sum_{i=2}^{n} \gamma_{(i)}^p\right), i \geq 3 \tag{4.13}$$

$$\chi_{f_i} = -0.0011 + \frac{0.00332}{\gamma_{YR}^p - 0.00612}\ , i \geq 2 \tag{4.14}$$

$\gamma_{(R_i)}^p - \gamma_{(Y_i)}^p$, very important to the modified yield function, could be understood as the influence range of self-weakening and denoted as loosing zone. Its dimension is decided by the residual stress remaining after unloading. By far there is bare relevant research reported. Here, the loosing zone is assumed as a function of the loading history (the residual strain $\Delta\gamma_R^p$) and stress state.

$$\gamma_{YR}^p = \gamma_{YR}^p\left(\bar{\tau}, I_1, t_1, \Delta\gamma_R^p\right) \tag{4.15}$$

Since the stress variation is the same in every cycle, the strengthening coefficient is assumed as the function of loading history.

$$R_f = R_f\left(\Delta\gamma_R^p\right) \tag{4.16}$$

Because of the shortage of data, the process of taking value is simplified. Loosing zone is 0.3 of the maximal residual strain (except the first cycle). Strengthening amount distribute evenly by the residual strain (except the first two cycles).

$$\begin{cases} \gamma^p_{(R_i)} - \gamma^p_{(Y_i)} = 0.3\gamma^p_{(\sigma_{max})} \\ R_f = \dfrac{\sum_{i=4}^{n} \gamma^p_{(i-1)} - (n-2)p}{\sum_{i=3}^{m} \gamma^p_{(i-1)} - (m-2)p} k\sigma_f \end{cases}, i \geq 3 \tag{4.17}$$

Where m is the number of total cycles; n is the number of cycles; σ_f is strength; k is strengthening parameters, percentage of strength; p is the average residual strain (except the first two cycles). Strengthening amount is obtained based on the accumulated residual strain. m is determined by fatigue life model. k approximately takes 0.06.

4.5 Chapter summary

This chapter investigated the conventional fatigue properties of rock salt with different stress ratio, loading velocity, temperature and confining pressure. Experimental results showed that:

Upper limit increase the fatigue life, while lower limit did not have significant impact on the fatigue life.

Loading velocity (with the range of 0.36KN/s~10KN/s) does not affect notably the fatigue life.

The rising temperature (within the range of 13℃~60℃) can lightly increase the fatigue life.

Under the same stress limits, confining pressure significantly raise the fatigue live, because the tenacity is strengthening.

A fatigue life model based on energy dissipation theory is established. Temperature and confining pressure can change the fatigue life through viscosity coefficient. Stress ratio changes the fatigue life by plastic work.

$$N_f \Delta W^{p\varsigma} = A_n \tag{4.18}$$

Through dislocation theory, the variation of dilatancy factor could reflect the development of dislocations and microcracks. In fatigue tests, the dilatancy factor increases with the cycle number, indicating that the contribution of microcracks to dilatancy growth. Inside the cycles, the dilatancy factor is initially big and then decreases (Fig. 4.10), demonstrating that the microcracks grow more in the beginning period.

By introducing the weakening coefficient, the yield function is modified to describe the conventional fatigue of rock salt.

$$F_i = \begin{cases} \bar{\tau} - F_1(I_1, \gamma^p), i = 1 \\ \frac{\bar{\tau}}{1-\chi_{f_2}} - F_1(I_1, \gamma^p), i = 2 \\ \frac{\bar{\tau}}{1-\chi_{f_i}} + R_f - f\left(I_1, \gamma^p - \sum_{i=3}^{n} \gamma_{(i)}^p\right), i \geq 3 \end{cases} \tag{4.19}$$

$$\chi_{f_i} = -0.0011 + \frac{0.00332}{\gamma_{YR}^p - 0.00612}\ , i \geq 2 \tag{4.20}$$

$$g_i = \beta + g_1(I_1, \gamma^p) \tag{4.21}$$

$$\begin{cases} \gamma_{(R_i)}^p - \gamma_{(Y_i)}^p = 0.3\gamma_{(\sigma_{max})}^p, i \geq 2 \\ R_f = \frac{\sum_{i=4}^{n} \gamma_{(i-1)}^p - np}{\sum_{i=3}^{m} \gamma_{(i-1)}^p - mp} k\sigma_f, i \geq 3 \end{cases} \tag{4.22}$$

.

5 Discontinuous fatigue and constitutive model for salt

The previous chapter introduced the conventional fatigue properties for salt. Conventional fatigue means the material is subjected to continuous cyclic load. However, in realitygeomaterials the loading typically is regular, but randomly interrupted an reactivated. For instance, a gas storage group in Jintan, Jiangsu province, China, completes one injection-production cycle each year. The designed gas pressure cycle does not continuously change, but discontinuously changes, Fig. 5.1.

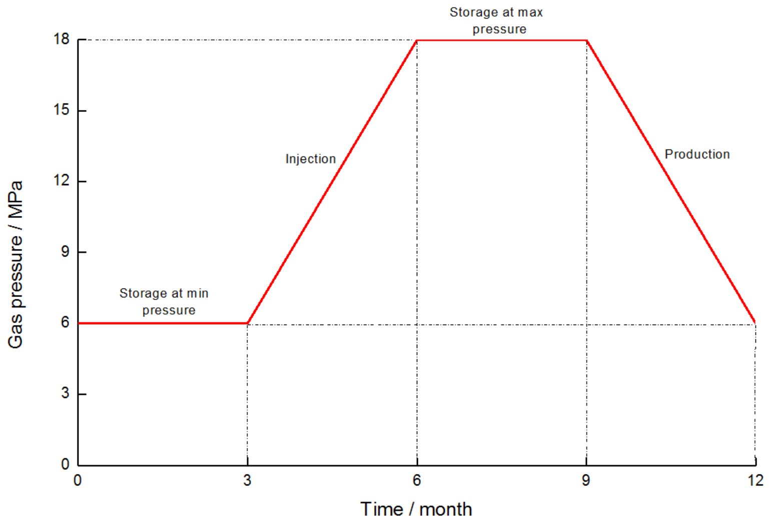

(a)Synchronous adjusting mode

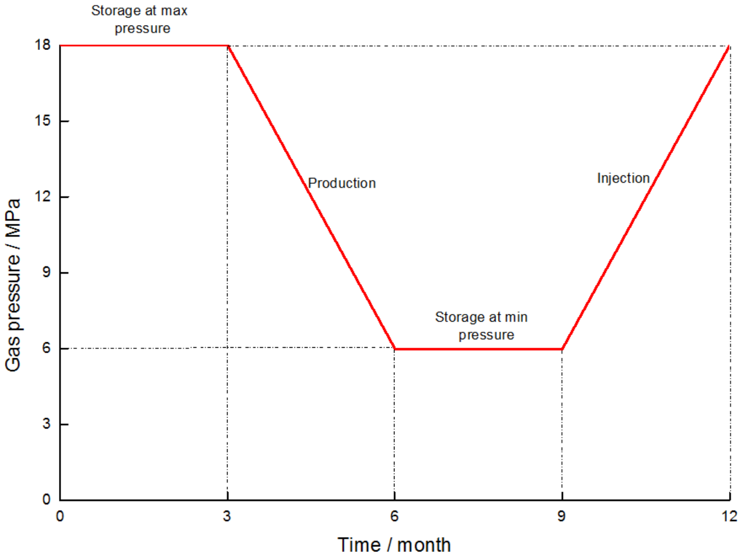

(b)Antisynchronous adjusting mode

Fig.5.1 Designed gas pressure variation in Jintan storage.

For synchronous adjusting mode, the low peak demand is in summer time, the gas is injected to salt caverns, thus the gas pressure increases. At the peak demand in winter, the gas is released to provide energy, thus the gas pressure decreases. In spring and autumn, the gas is in balance of supply and demand, thus the gas pressure keep unchanged. Therefore, this kind of cyclic load is discontinuous.

The similar problem arises in other area of China for using. Fig. 5.2 is the variation of gas consumption: in Apr~Jul and Sep~Oct coefficient of gas consumption is 1. 1 means the balance of supply and demand. The gas pressure keeps constant.

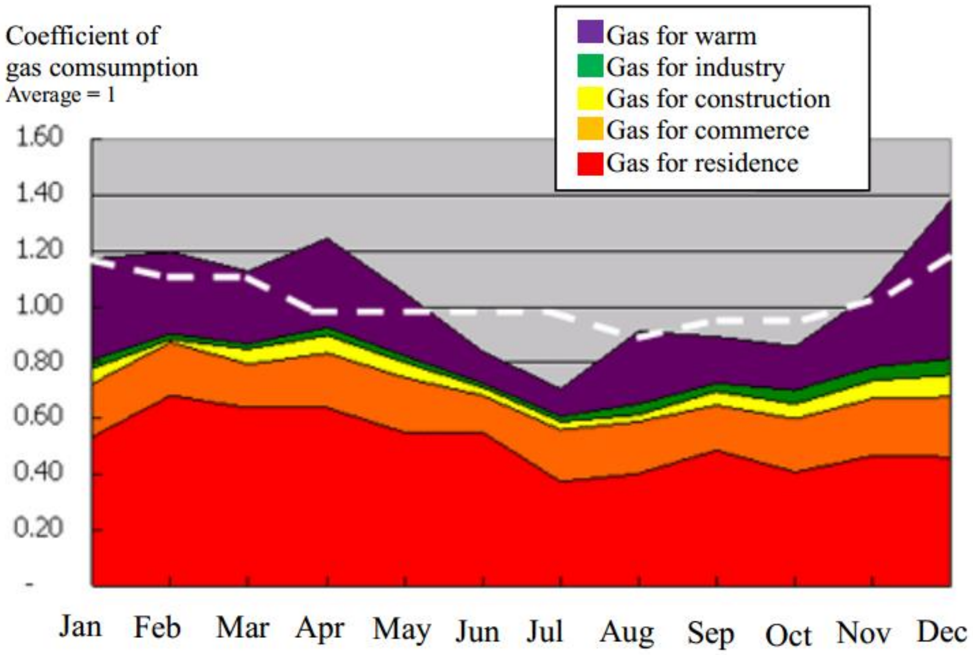

Fig.5.2 Gas consumption for one city in China.

Germany Huntorf plant completes one cycle every day. The underground salt CAES works 10 hours and stop 14 hours. During the period of stop, the air pressure inside CAES is constant. Whether this pressure plateau would exert influence on the fatigue properties is unclear.

5.1 Experimental design

To ensure the comparability of experimental result, the same samples and equipment are used in the following discontinuous cyclic loading tests. Some of the rock salt samples have standard cylindrical shape of 50mm×100mm. The others are cubes with 50mm side length. Tests are performed in unconfined condition under the room temperature 20±3℃. A special design is the loaded sample is encased by a plastic bag (Fig. 5.3) to keep the moisture inside constant.

Fig.5.3 Sample encased in a plastic fresh-keeper bag.

Three groups of discontinuous cyclic loading tests, 1301group, 1401group and 1501group, are conducted to investigate the basic properties of discontinuous fatigue, the effect of time interval and the effect of lower stress limit, respectively.

To eliminate the possibility of creep, the lower stress limit is set at zero in group 1301. Regarding the sensitivity of the loading machine, it is difficult to reach real 0KN, the stress limit is set to 3KN. To control the experimental time within 0.5~2hour, the upper (stress ratio) limit is set to 85%. The loading velocity is 2KN/s. After every two continuous cycles the loading is interrupted during a certain time interval (Fig. 5.4). The cycles before these intervals are denoted as B path, while the after, they are denoted as A path.

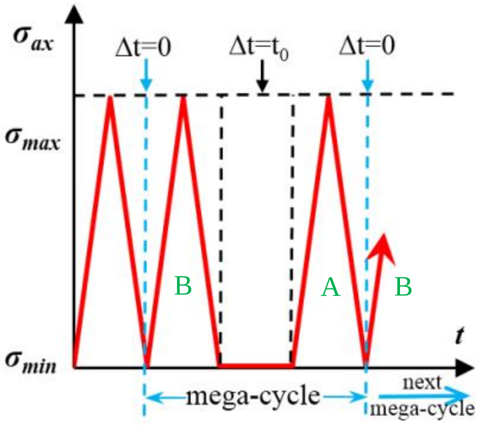

Fig.5.4 Loading path for 1301group tests.

5.2 Essential features

5.2.1 Stress-strain curves

Discontinuous fatigue tests show a distinct difference from the conventional tests. As shown in Fig. 5.5, the fatigue life of the salt samples from conventional fatigue test and 1301group tests are 89, 34, 24, 13, 20, respectively. The fatigue live of salt from 1301group is significantly lower than that from the conventional one under the same conditions.

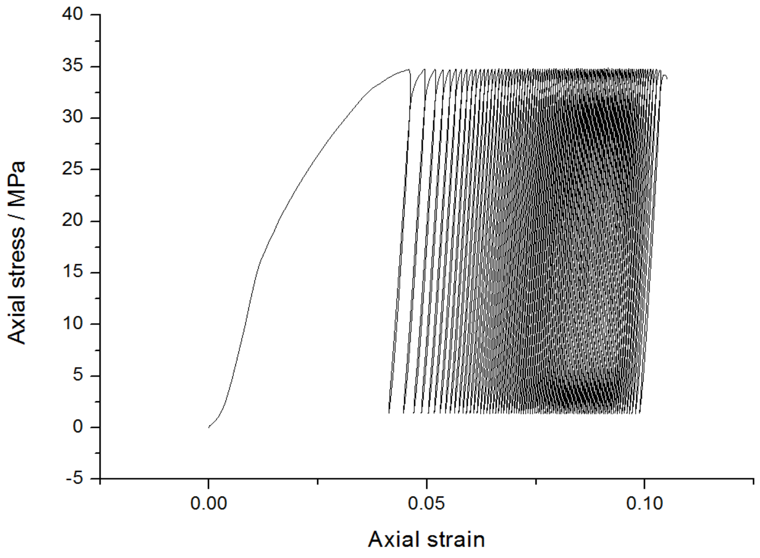

(a) Conventional fatigue test

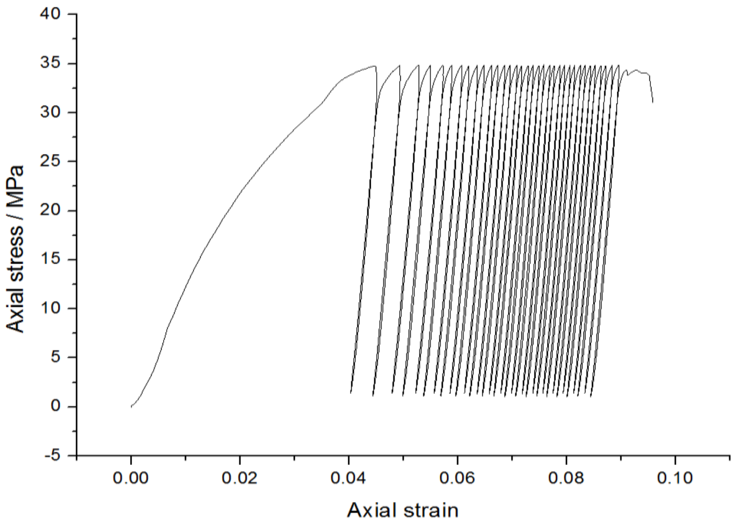

(b) Discontinuons fatigue test (Δt=5min)

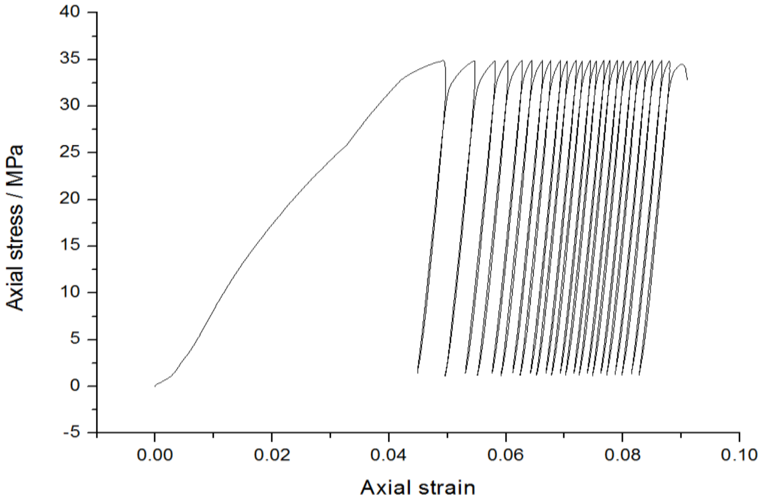

(c) Discontinuons fatigue test (Δt=10min)

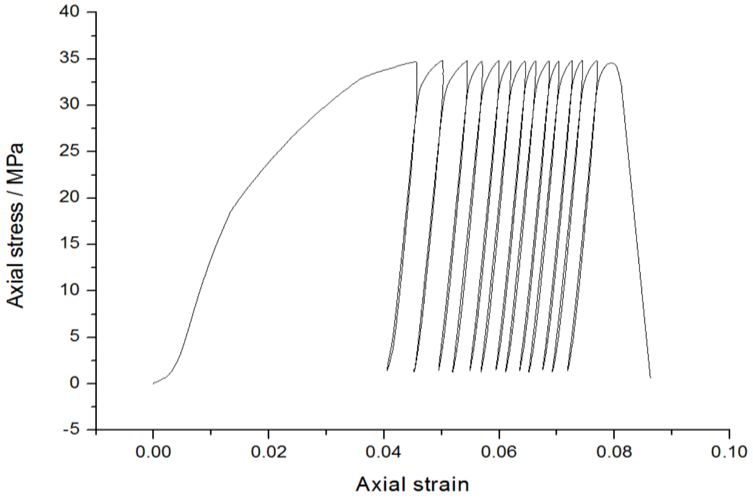

(d) Discontinuons fatigue test (Δt=15min)

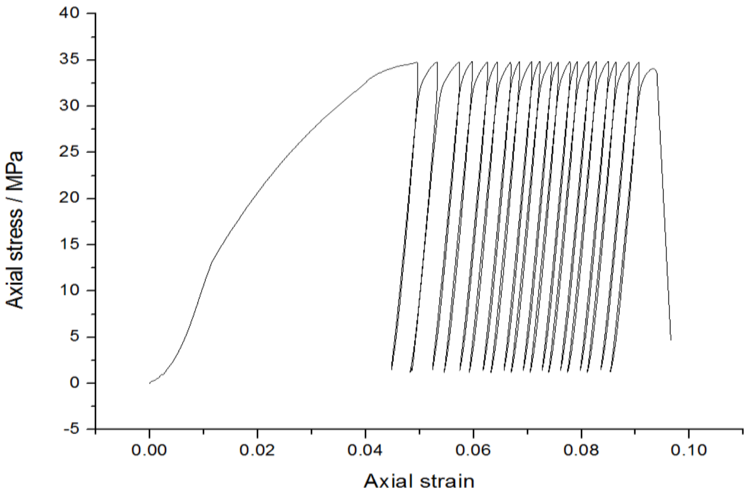

(e) Discontinuons fatigue test (Δt=20min)

Fig.5.5 Axial stress-axial strain plot from conventional fatigue test and 1301.group of discontinuous fatigue tests.

Calculating the total accumulated plastic deformation (except the last uncomplete cycle), this accumulated plastic deformation of the salt samples from 1301group is 7.2%-8.5%, smaller that from conventional fatigue tests, 9.1%-11%.

5.2.2 Residual strains

Every loading generate a certain deformation. While one part of it (elastic deformation) is recovered during the unloading, the other, is not. The remaining part is plastic strain, also called the residual strain $\Delta\varepsilon_{(i)}^{p}$, where *i* represents the cycle number.

Calculating the residual strain in every cycle leads to the understanding of the evolution of plastic damage of salt sample under discontinuous cyclic loading. Fig. 5.6 shows the residual strain evolution with stress cycles. The residual strain firstly reduces, then keeps at a constant and finally increases a little when close to failure. In previous studies, the first stage is called as decelerated deformation phase; the second is uniform deformation phase; the last is accelerated deformation phase [126]. In the aspects of these three phases, 1301group tests show the same features with the conventional.

However, what is the distinct between two types of fatigue tests is that: In 1301group tests, the residual strain from A path is significantly larger than that from B path. Fig 5.7 accumulated the residual strain separately for A path and B path. It can be seen that the accumulating rate against stress cycle from A path is faster than that from B, indicating that the plastic deformation development from A path is promoted during time intervals.

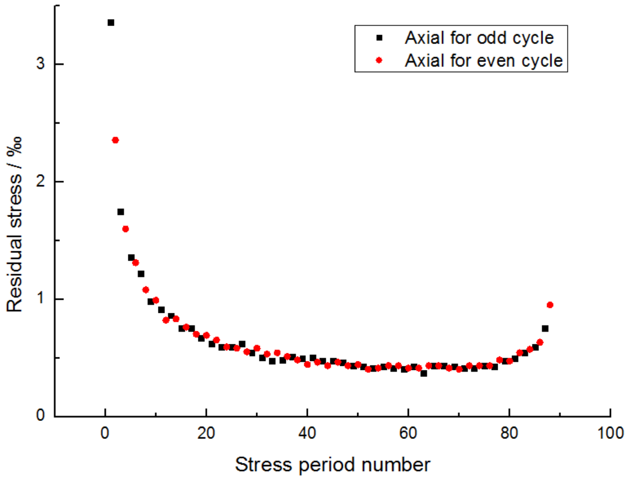

(a) Conventional fatigue test

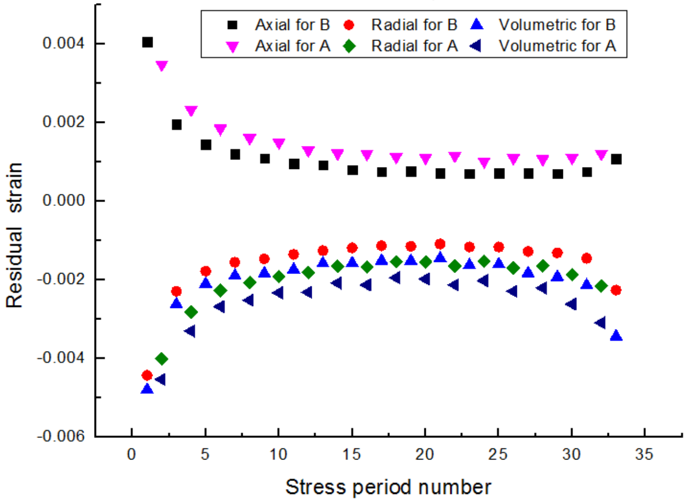

(b) Discontinuons fatigue test (Δt=5min)

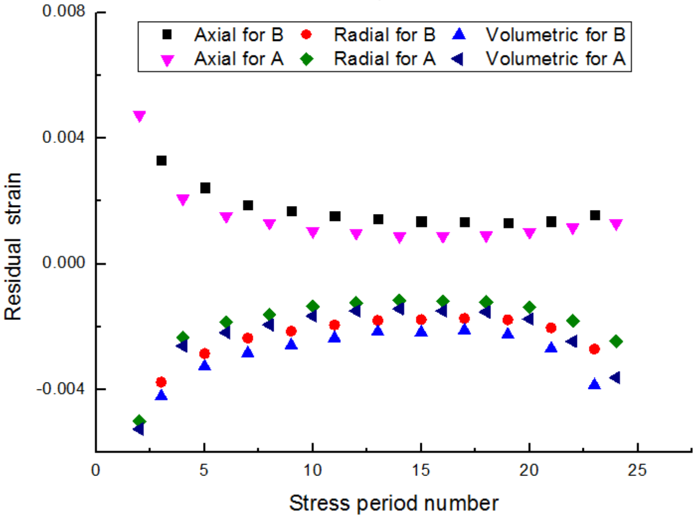

(c) Discontinuons fatigue test (Δt=10min)

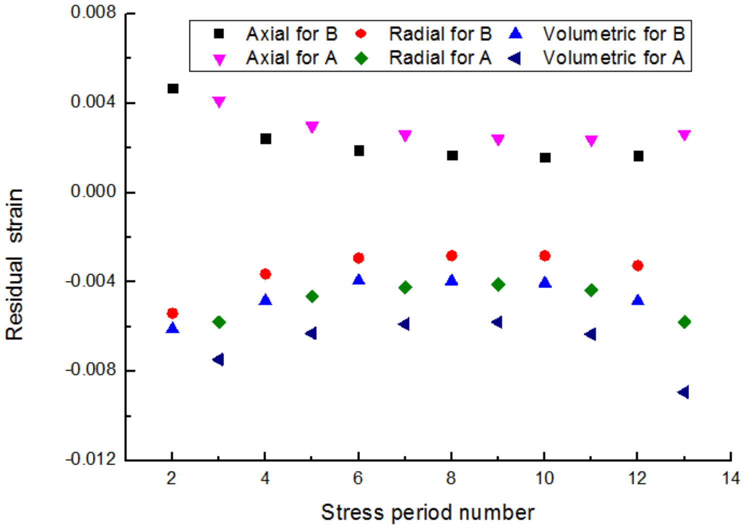

(d) Discontinuons fatigue test (Δt=15min)

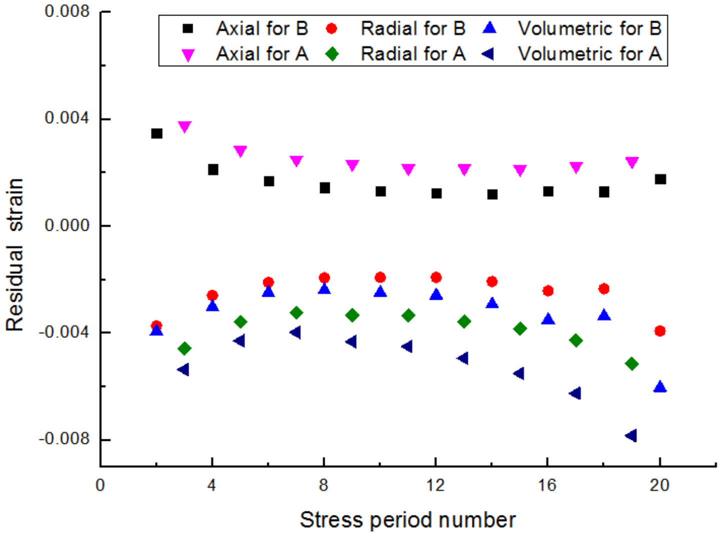

(e) Discontinuons fatigue test (Δt=20min)

Fig.5.6 Evolution of the residual strain with loading cycles from conventional fatigue test and 1301.group of discontinuous fatigue tests.

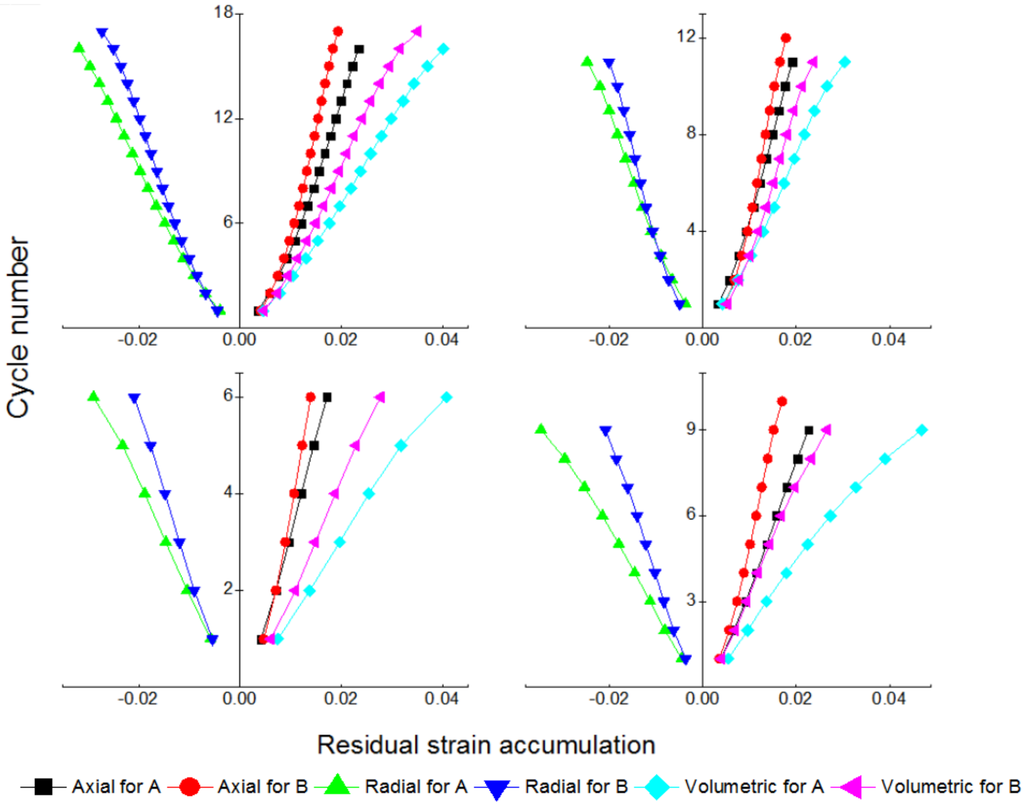

Fig.5.7 Variation of residual strain from 1301.group of discontinuous fatigue tests.

5.2.3 Elastic constants

The elastic modulus is calculated from the slope of the linear segment BC segment is calculated as in Fig. 5.8. In the conventional fatigue tests, the elastic modulus increases with the stress cycles (Fig. 5.9).

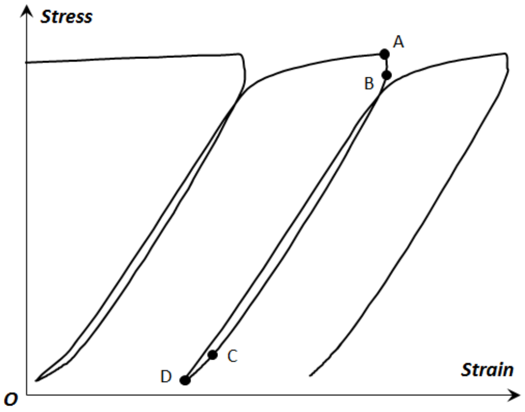

Fig. 5.8 Schematic diagram of the method for calculation of elastic module.

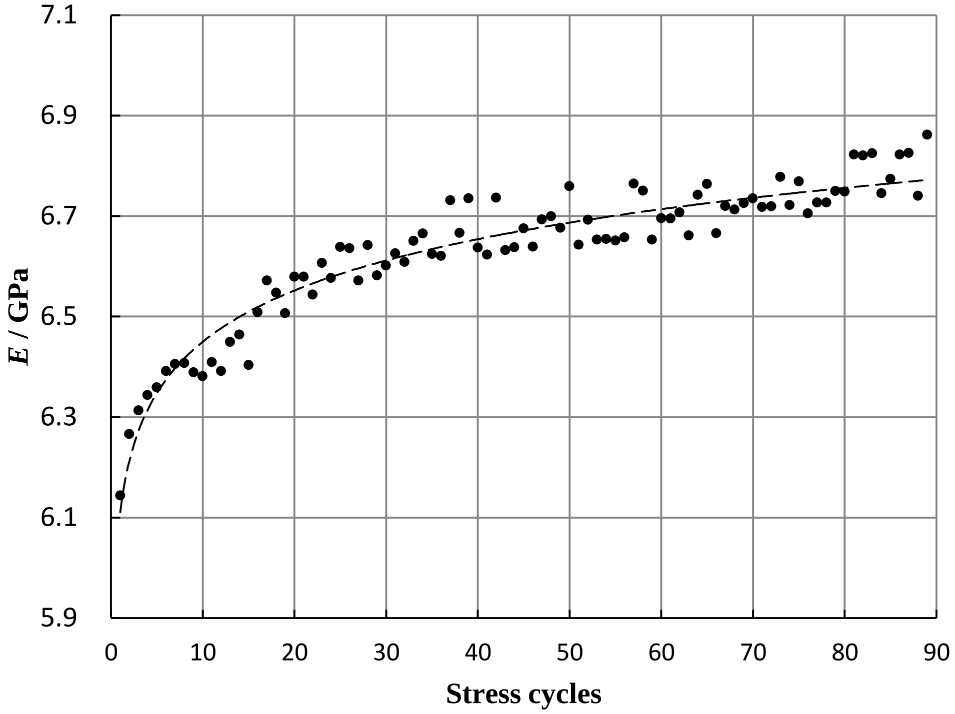

Fig. 5.9 Evolution of elastic modulus in conventional fatigue test.

Salt comprises many crystalline grains. The intact grain could orderly release the elastic strain energy. As the fatigue damage accumulates, the number of the crushed (damaged) grains rises and the incremental elastic strain reduces, leading to the elastic modulus increases. For every loading, the slipping path of dislocation is random. In different path, the intact functionary grain may be different, so the elastic modulus fluctuates lightly. Surely, this fluctuation is also related to the error from the measurement device and data processing.

The calculated elastic modulus for 1301group is shown in Fig. 5.10. The elastic modulus from A path is larger than that from B path, indicating that A path loading could damage more grains, lessening the reversible elastic deformation.

The Poisson’s ratio did not show any significant difference between A and B path. As the whole trend, the Poisson’s ratio increases with cycles, both for conventional fatigue tests and 1301group tests.

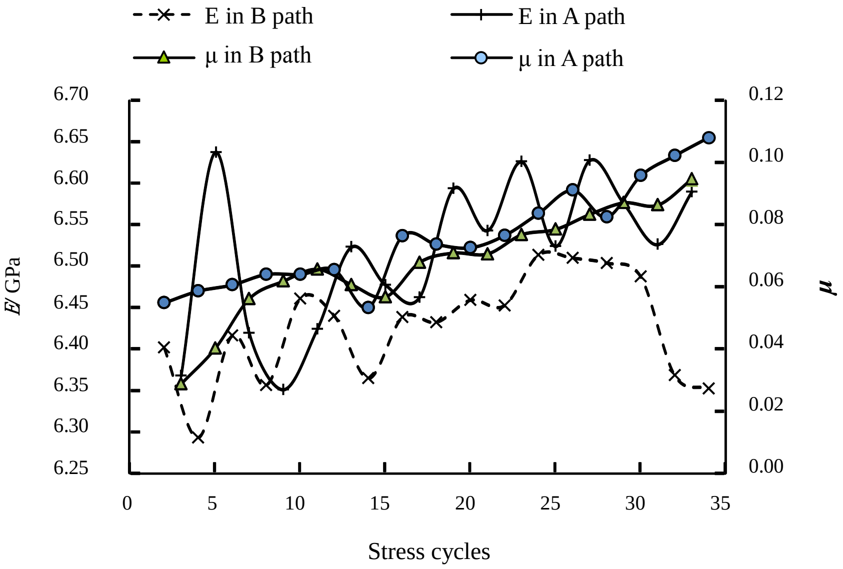

(a) Discontinuons fatigue test (Δt=5min)

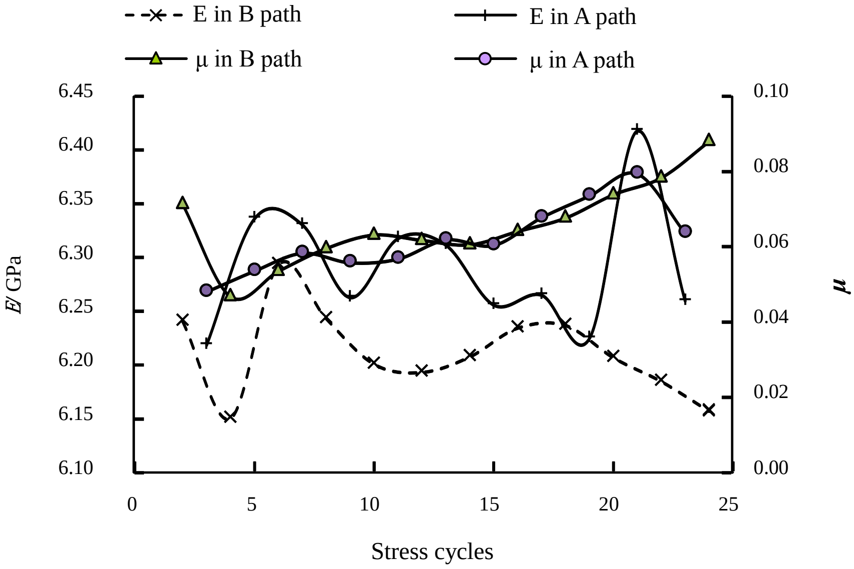

(b) Discontinuons fatigue test (Δt=10min)

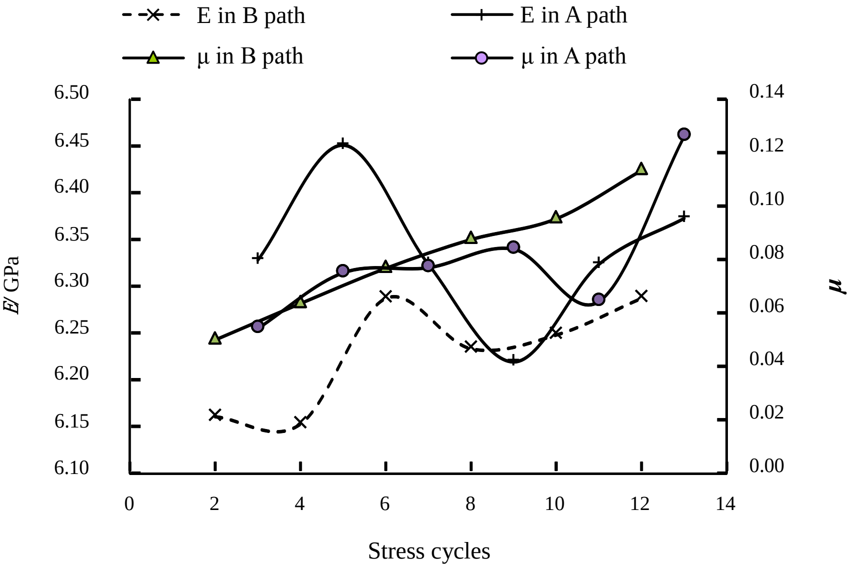

(c) Discontinuons fatigue test (Δt=15min)

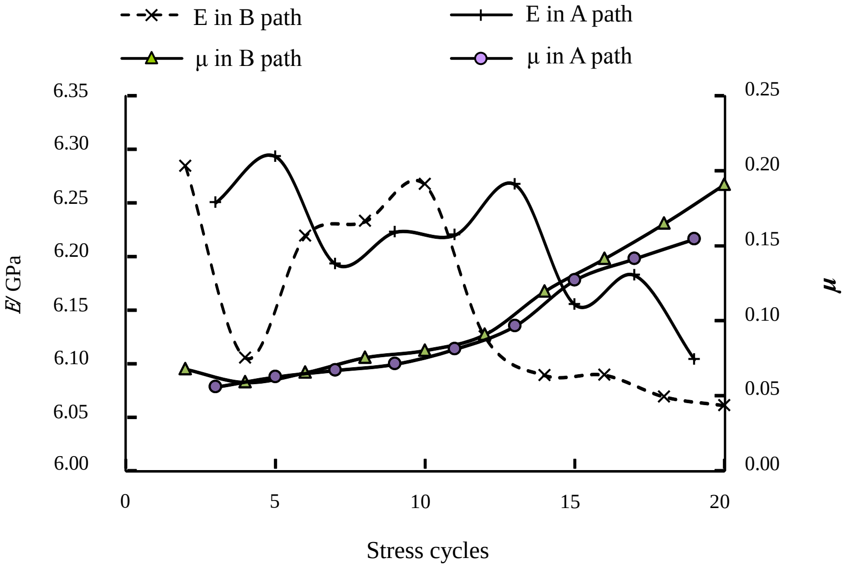

(d) Discontinuons fatigue test (Δt=20min)

Fig. 5.10 Variation of elastic module and Poisson's ratio from the 1301.group of discontinuous fatigue test.

5.2.4 Dilatancy angle

Dilatancy angle reflects the relation between the increment of plastic volumetric deformation and increment of plastic shear deformation. Dilatancy angle is related to the mechanism of plastic deformation: plastic shear strain is due the dislocation slippage before the initiation of microcracking. Volumetric expansion depends on the vacancy and lattice distortion, thus the dilatancy angle (or dilatancy factor) is constant. If microcracks propagate rapidly, the dilatancy is influenced by increase in space of microcracks and the dilatancy angle increases with plastic shear strain.

The average tangent of dilatancy angle in every cycle was calculated. It rises with stress cycle, showing the contribution of microcracks to dilatancy growth. Although the dilatancy angle varies differently between A and B, the developing trends in A path and B path are the same.

5.2.5 Time interval effect

The scattering of experimental results brings much inconvenience to the analysis. To investigate the effect of time interval on the fatigue properties and avoid the discreteness of different samples, the 1501 test is conducted following the loading path in Fig. 5.11.

The stress ratio, loading velocity and temperature applied in 1501 test are the same with 1301group test. Every stress cycle is followed by an interval. The intervals are 0min, 5min, 10min, 15min and 20min, in turn. Every five cycles and relevant interval are considered as a megacycle M$_i$.

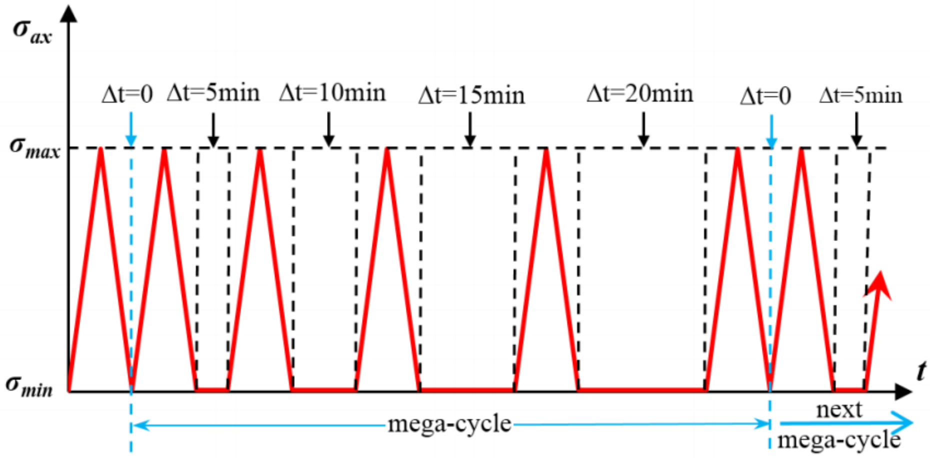

Fig. 5.11 Loading path for 1501 test.

The 1501 test combines the interval effect of 0min, 5min, 10min, 15min and 20min. 38 cycles, 7 mega-cycles were completed. The total accumulated plastic strain is 8.4%, much lower than in the conventional fatigue test. The calculated elastic modulus and residual strain are shown in Fig. 5.12 and 5.13.

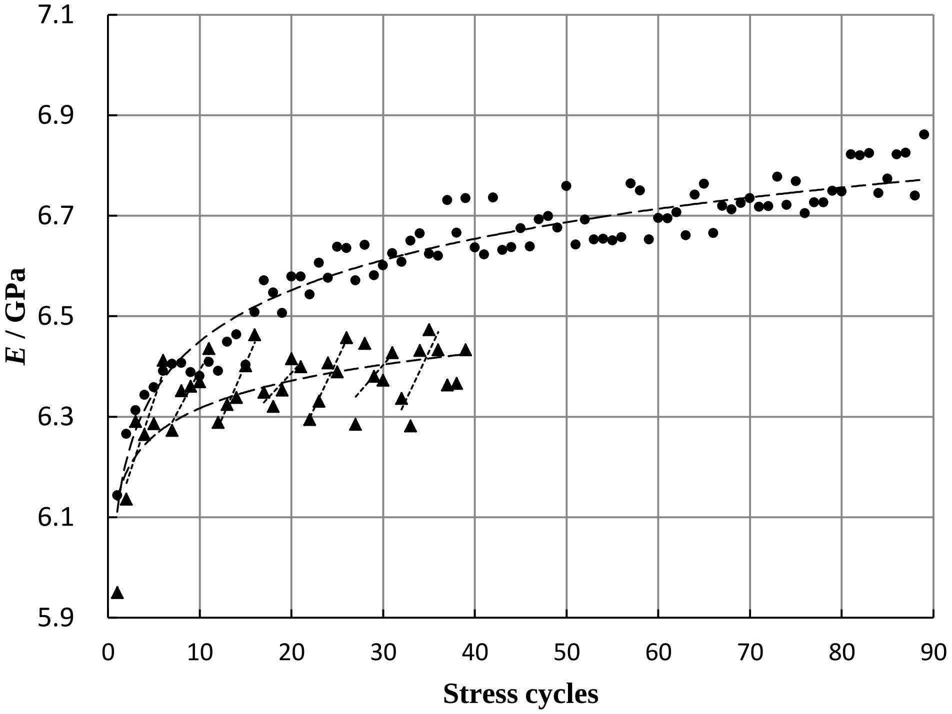

Fig. 5.12 Variation of elastic modulus from 1501 discontinuous fatigue test and conventional fatigue test.

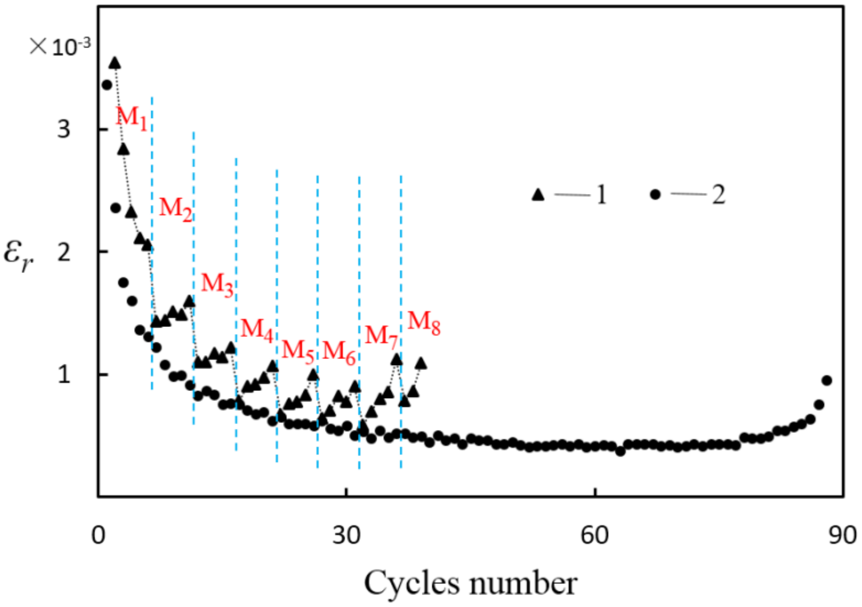

Fig. 5.13 Variation of the residual (axial) strain from the 1501 discontinuous fatigue test (indicated with 1) and conventional fatigue test (indicated with 2).

The tendencies of elastic modulus from two type experiments are the same with a narrow range of error. But the time interval shows the influence on the elastic modulus, which approximately increase within the megacycle.

Except the first megacycle, the residual strain increases within the megacycle as the time interval elongates, indicating the time interval could exert notable influence on the discontinuous fatigue properties of salt.

5.2.6 Rupture form

The rupture shape of salt from discontinuous fatigue and conventional fatigue is similar for uniaxial compression test (Fig. 5.14). The cracked salt samples appear mixed fracturing with split and shear. Two parts form, one fusiform structure inside the sample (A part in Fig. 5.15c) and cylindrical wall outside (B part in Fig. 5.15d). The fusiform structure finally was cut by a thoroughgoing shear crack, divided into two cone parts (as shown in Fig. 5.14c and d).

The fusiform structure forms because of the end friction. When the fusiform structure is compressed and expands around, the B part has to subjected to the squeezing from A part and generates tensile cracks (as shown in Fig. 5.14a and b). CT scanner was applied to scan the intersections of a sample which has complete three cycles with 0~85% stress ratio. A vertical crack was observed in Fig. 5.16b and a crack separating A part and B part was observed in Fig. 5.16a. Judging by the structure, the boundary crack between A and B controls the stability of the sample. SEM is applied to observe the development of boundary cracks. In Fig. 5.17 it is found a crack band and a set of parallel shear cracks. Some of the cracks run along the crystalline boundary, while others, traverse some crystalline grain.

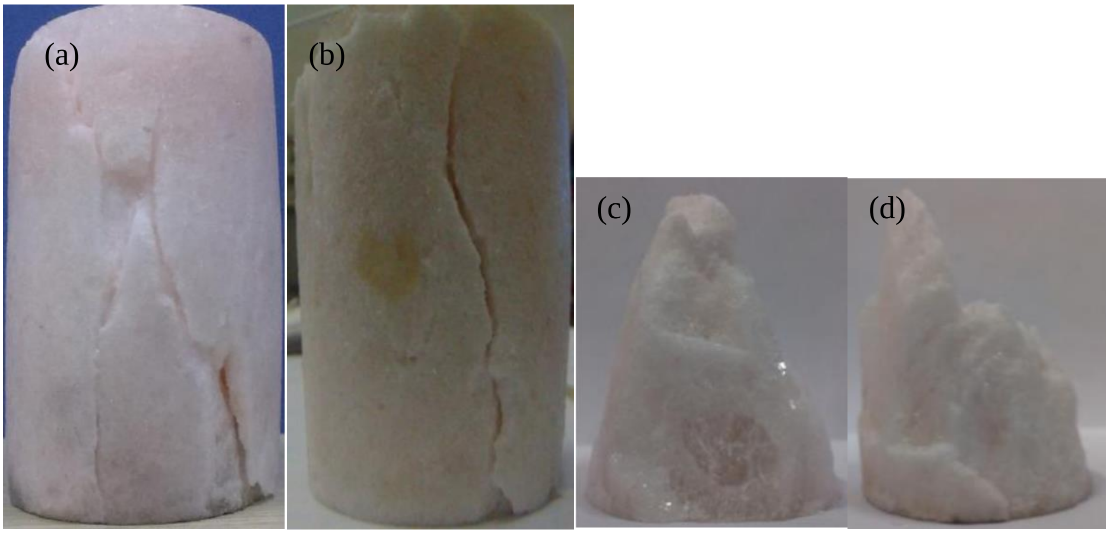

Fig. 5.14 Fractured sample.

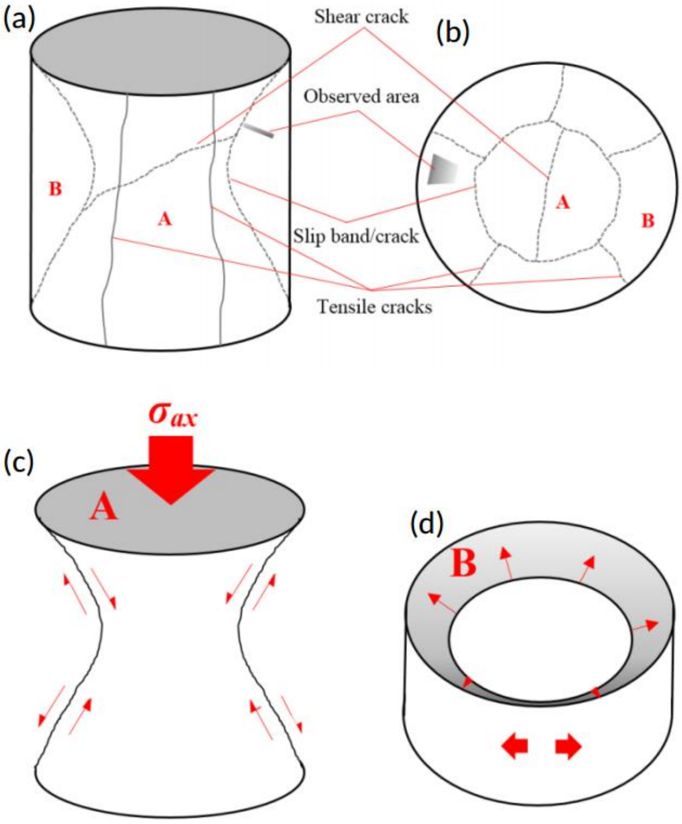

Fig. 5.15 Fractures formed during deformation.

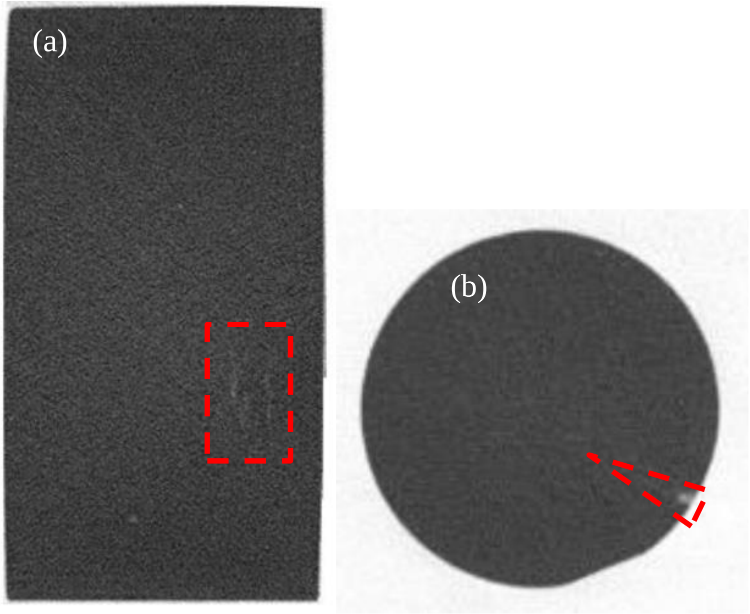

Fig. 5.16 CT images of sample subjected to 3 stress cycles.

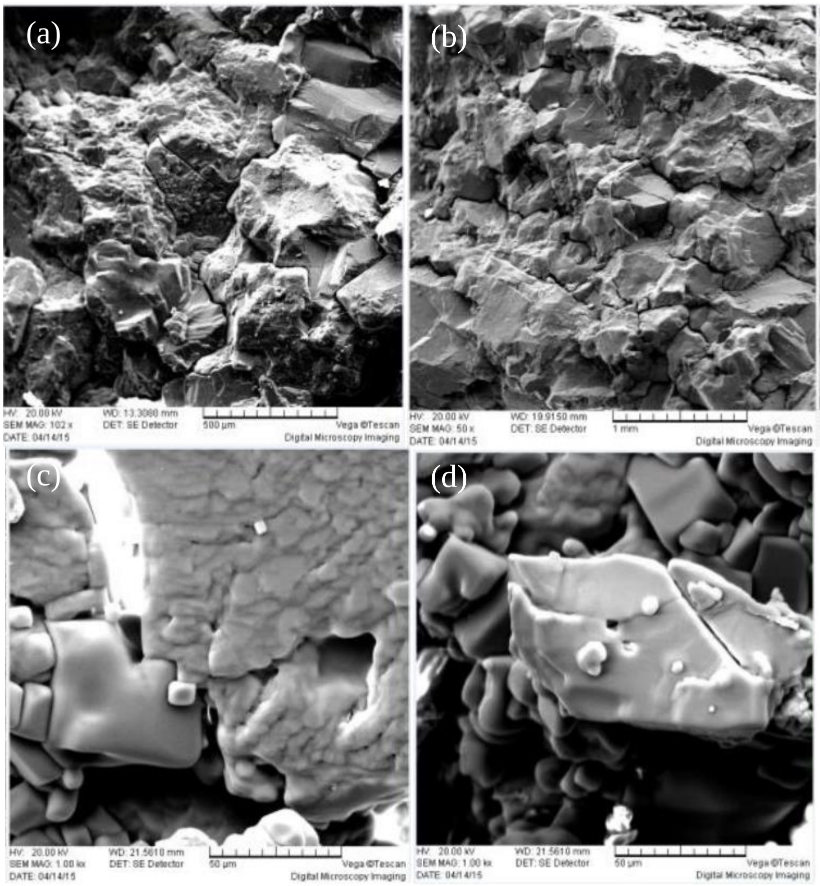

Fig. 5.17 SEM images of fracture surface.

5.3 Long interval effect

The intervals within 20min were investigated. It is found that the time interval continuously affects the fatigue properties of salt. However, the critical threshold is unclear. It is necessary to continue the tests to find out the longest effective interval.

5.3.1 Experiment setup

Two cycles were completed in these tests. Firstly, the samples were loaded to 65% of the compression strength with 2KN/s loading velocity, then unloaded to zero with 5KN/s loading velocity. The second loading continued to failure with 2mm/min velocity (Fig. 5.18). The time interval between two cycles Δt took is $0.5h$, 1h, 2h, 4h, 8h, 4d. During the interval, samples were wrapped in a sealed plastic bag. The sample and loading machine are the same as previously. These tests are denoted as 1401group tests. Every test has been performed twice, numbered as *a* and *b*.

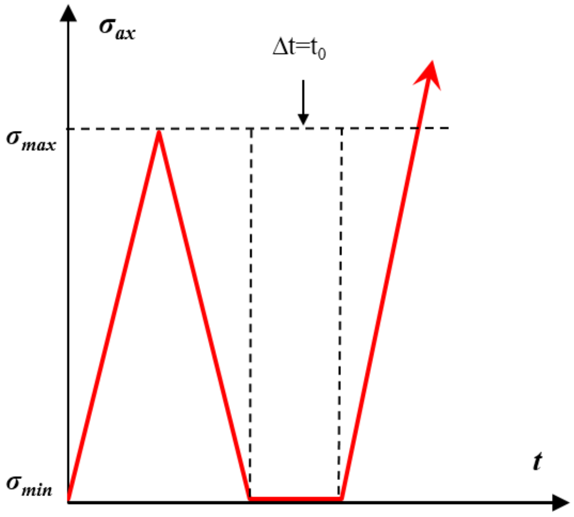

Fig. 5.18 Loading path.

5.3.2 Experimental results

It is found from the tests that the time interval of 4h as the threshold takes effect in the second loading. The effect contains:

① Peak stress of the second loading decreases with the interval (Table 5.1) below 4h, but fluctuates with the interval above 4h. Similarly, the elastic modulus (calculated from linear segments in loading process) decreases notably as the interval is less than 4h, not notably when the interval is larger than 4h.

② The distance between unloading curve and the second loading curve becomes wider as the interval becomes longer. That the compaction stage in second loading becomes longer indicates the porosity increases during the intervals. The yield stress of second loading decreases as is shown in Fig. 5.19.

Table 5.1 Peak stress, peak strain and elastic modulus of the sample in second loading

Sample No.	*a*	*b*
	Peak stress σ_{pk} / peak strain ε_{pk} / elastic modulus E /Possion's rate μ	
Interval Duration	MPa / 100% / GPa / 1	
0.5h	42.46/0.0592/4.202/0.07	41.87/0.0601/3.756/0.05
1h	40.54/0.0514/4.24/0.07	38.68/0.0483/4.286/0.07
2h	39.38/0.0575/3.441/0.09	37.97/0.0524/3.912/0.08
4h	36.97/0.0562/2.563/0.25	37.69/0.0497/3.096/0.21
8h	38.58/0.0664/2.196/0.17	37.11/0.0504/3.531/0.21
4d	36.46/0.0527/3.009/0.27	37.62/0.0537/3.400/0.20

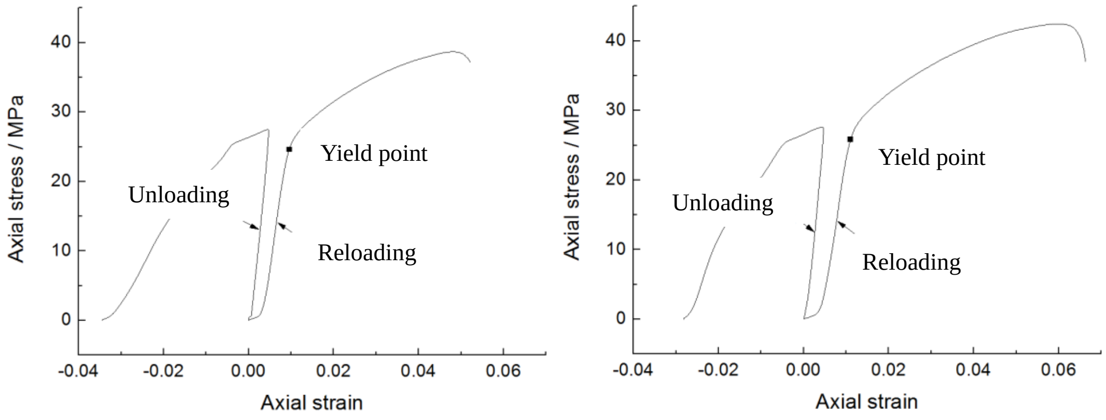

(a) $\Delta t = 0.5h$ (b) $\Delta t = 1h$

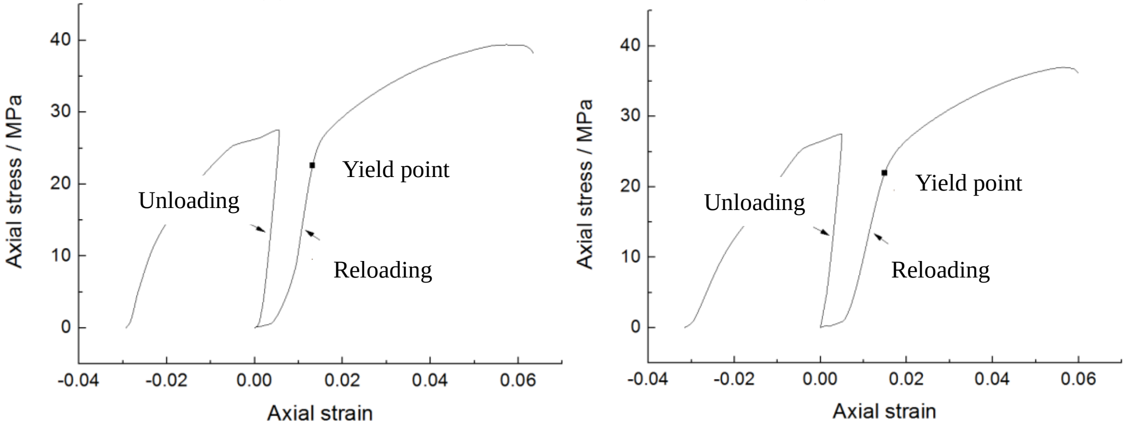

(c) $\Delta t = 2h$ (d) $\Delta t = 4h$

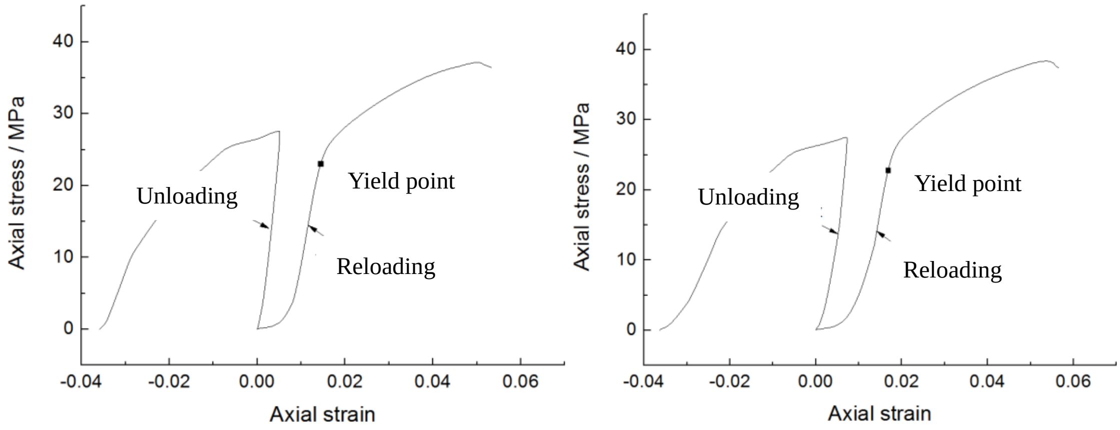

(a) $\Delta t = 8h$ (b) $\Delta t = 4d$

Fig. 5.19 Axial stress-axial strain curve from 1401 group tests.

5.4 Lower limit effect

The previous discontinuous fatigue tests were all conducted with negligible stress in the interval. This section is to investigate whether the non-zero stress interval has the same effect. As stated before, the rupture pattern of the cylindrical compressed sample is complex. To obtain the clear and simple rupture form, this series of discontinuous fatigue tests is conduct in oblique shear mode.

5.4.1Experiemental conditions

The material is the same, but shaped into cube with 50mm side length (Fig. 5.20). The loading machine is the same, but equipped with one shear loading die (Fig. 5.21).

Fig. 5.20 Specimen of cube shape.

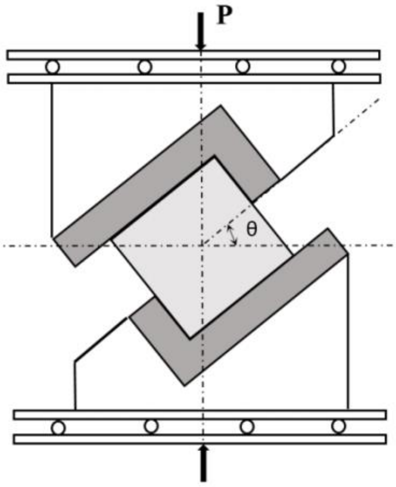

Fig. 5.21 Shear loading die.

In these shear tests, the shear stress is generated the vertical compression applied by the machine. Considering the friction between roller and die, the shear stress along the shear plane τ and normal stress normal to the plane σ are calculated as

$$\begin{cases}\tau = \frac{P}{A}(sin\theta - fcos\theta) \\ \sigma = \frac{P}{A}(cos\theta - fsin\theta)\end{cases} \tag{5.3}$$

Where *P* is the vertical force; *A* is the area of shear fracture surface; θ is the angle between the shear plane and the horizontal plane; *f* is the friction coefficient of the roller die, related to the number and diameter of rollers. In these experiments, the friction coefficient is neglected. Shear strain and normal strain are calculated from the vertical displacements ΔL,

$$\begin{cases}\gamma = \frac{\Delta L}{Lsin\theta} \\ \varepsilon = \frac{\Delta L}{Lcos\theta}\end{cases} \tag{5.4}$$

In this test series, the shear angle is 45° . Lode angle is 44.47° . The shear peak stress is 32.5MPa, when the shear angle is 45° . The corresponding strain is 12.4%. The shear stress-strain curves are shown in Fig. 5.22.

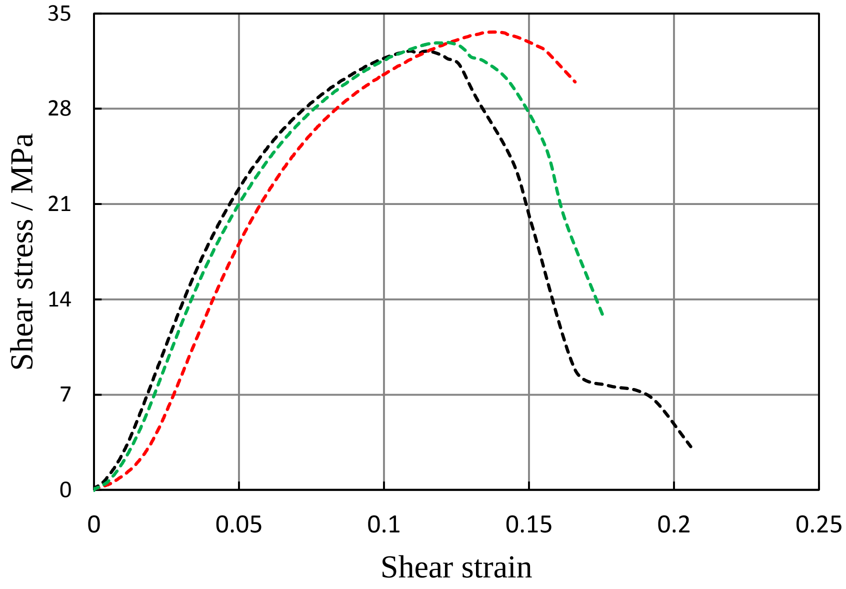

Fig. 5.22 Shear stress-shear strain curve from 45 °-shear tests.

The discontinuous cyclic loading tests with changing lower limit are denoted as group 1503 tests. The upper limit is fixed at 75% of the strength. The lower limit is 5%, 15%, 25%, 35% and 45%. The room temperature is 23±3℃, the air relative moisture is 58~70%. The applied loading path is the same as in 1301group test. Time interval is 120 seconds.

5.4.2 Stress-strain curve

It can be found from the curves in Fig. 5.23 that the time interval still influences the fatigue of salt as the lower limit growth from 5% to 45%. The A path and B paths are indicated on the curves in Fig. 5.23. The space between loading stage line and unloading stage line from A path (red arrows) is wider than that from B path (blue arrows), indicating the residual strain developing in A path is larger than B path. Because the experiment exceeds 12 hours, the discontinuous fatigue tests with the stress of 35%~75% and 45%~75% are aborted.

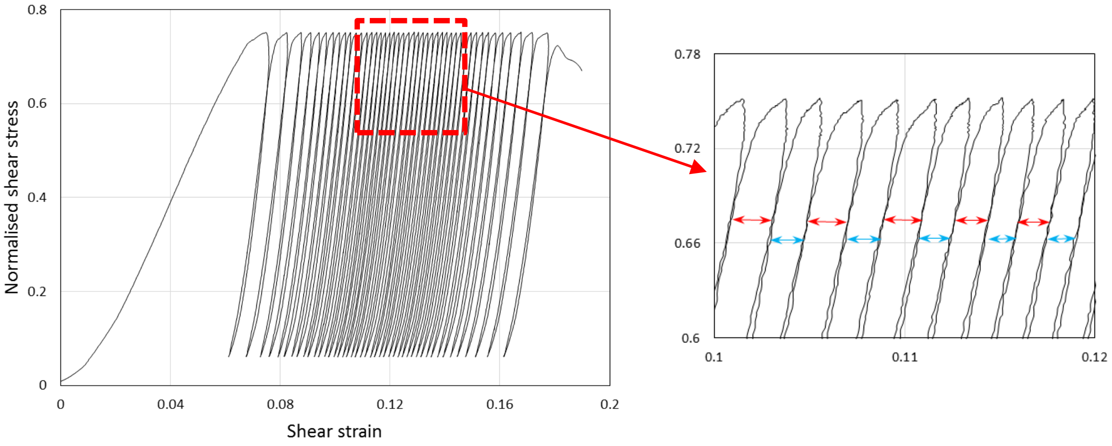

(a) Cyclic loading -unloading test with 5%~75% stress limit

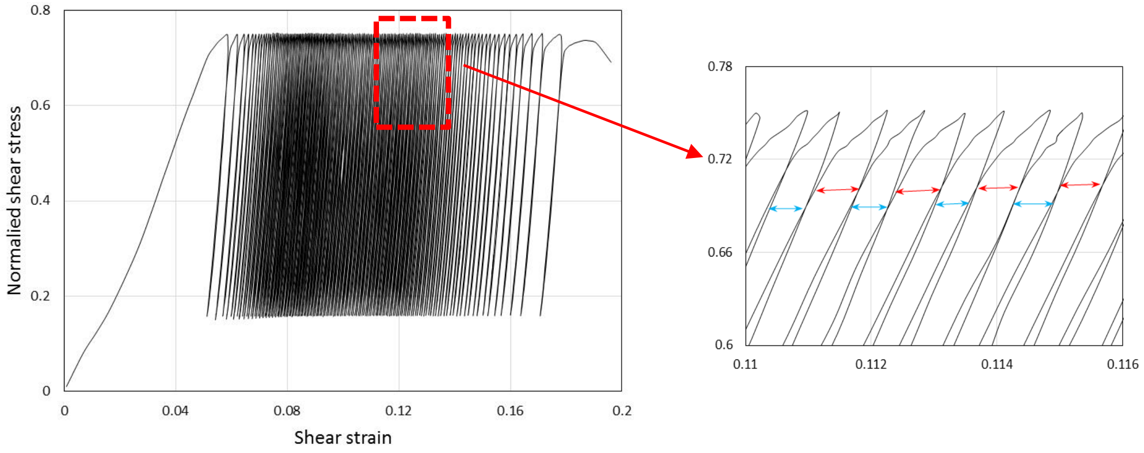

(b) Cyclic loading -unloading test with 15%~75% stress limit

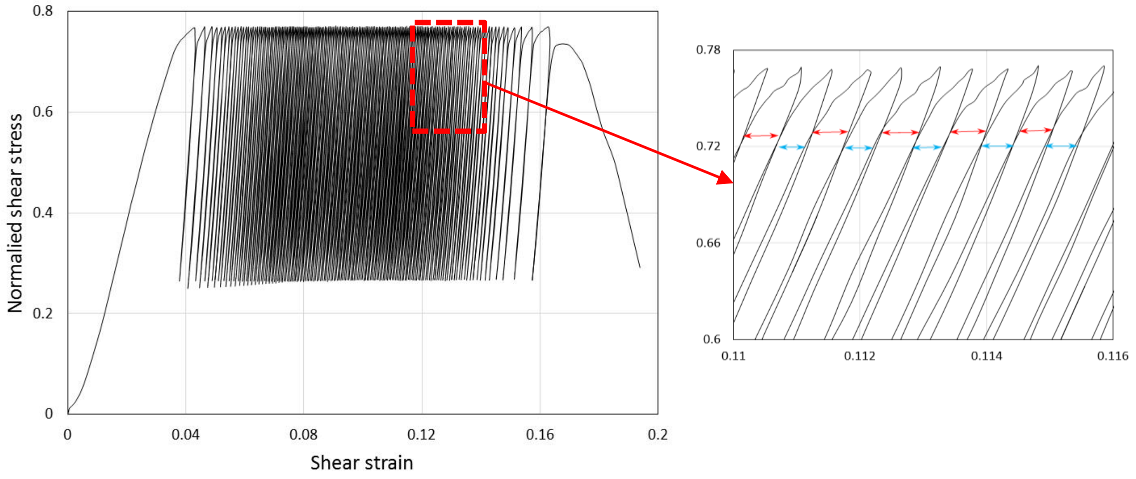

(c) Cyclic loading -unloading test with 25%~75% stress limit

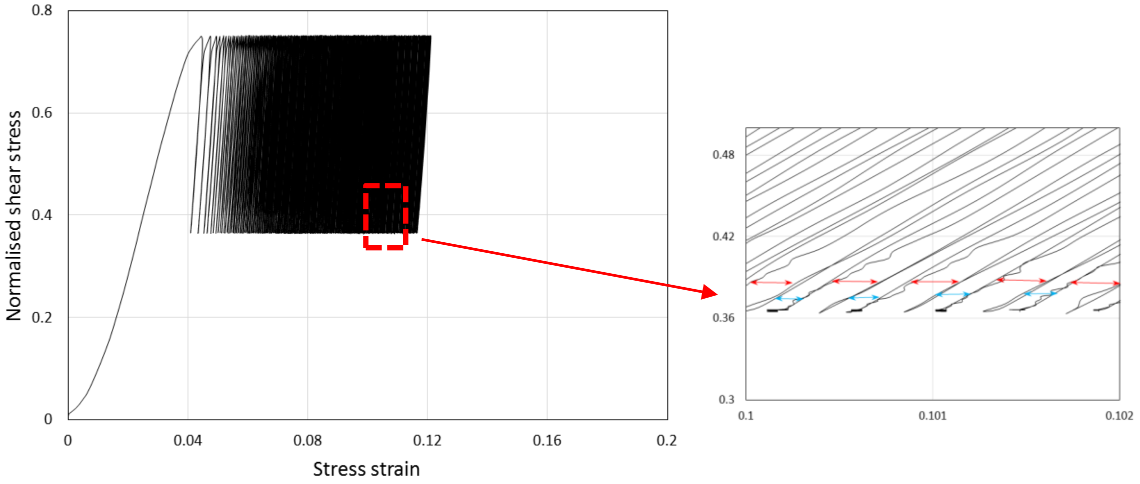

(d) Cyclic loading -unloading test with 35%~75% stress limit

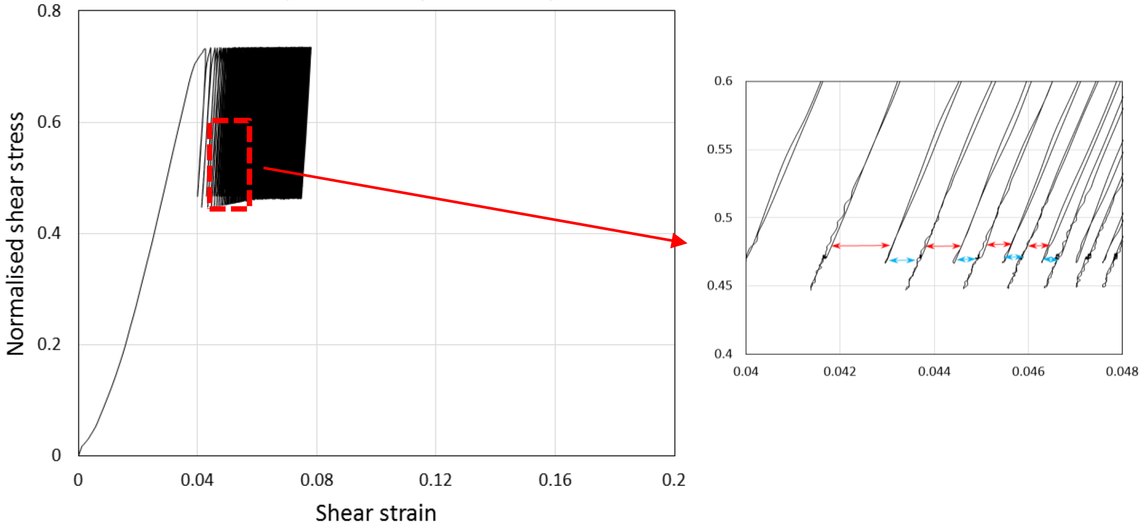

(e) Cyclic loading-unloading test with 45%~75% stress limit

Fig. 5.23 Shear stress-shear strain curves from discontinuous cyclic loading tests.

5.4.3 Fatigue life

The residual strain shows the same evolution as in the previous discontinuous cyclic loading tests (like 1301group tests). This need not be repeated here.

Known from equation (4.8), the fatigue life is more than 5000, as the upper limit is 75%. The statistics show the fatigue life is 43, 130 and 201 as the stress ratio is 5%~75%, 15%~75% and 25%~75% respectively. Rough estimate by accumulated plastic deformation and average residual strain show the fatigue lives are 450 and 1500 for test with stress ratio of 35%~75% and 45%~75%. These values are far lower than the predicted fatigue life.

5.5 Discontinuous fatigue life model.

The 1301 test shows the effect of time interval on discontinuous fatigue and 1503 test shows the laws of the time interval effect. However, both the data quality and quantity of 1301 test are not sufficient. Here the 1502 tests with the same as 1301 tests loading path were conducted to illustrate the relationship between fatigue life and the interval time. The obtained fatigue life is indicated in Table 5.2.

Table 5.2 Fatigue life of sample in 1502.group

Interval (sec)	*0*	*3*	*5*	*20*	*100*	*300*	*600*	*1200*	*2400*
Fatigue life	89	75	52	50	41	34	27	21	18
	88	76	62	48	46	36	33	22	15
	96	70	58	64	47	35	29	26	20
Average	91	74	57	54	45	35	30	23	18
SD (Standard Deviation)	4.36	3.21	5.03	8.72	3.21	1.00	3.06	2.65	2.52

The experimental results show that the fatigue life decreases with interval time. The relationship between the two is shown in Fig. 5.24, a logarithm function.

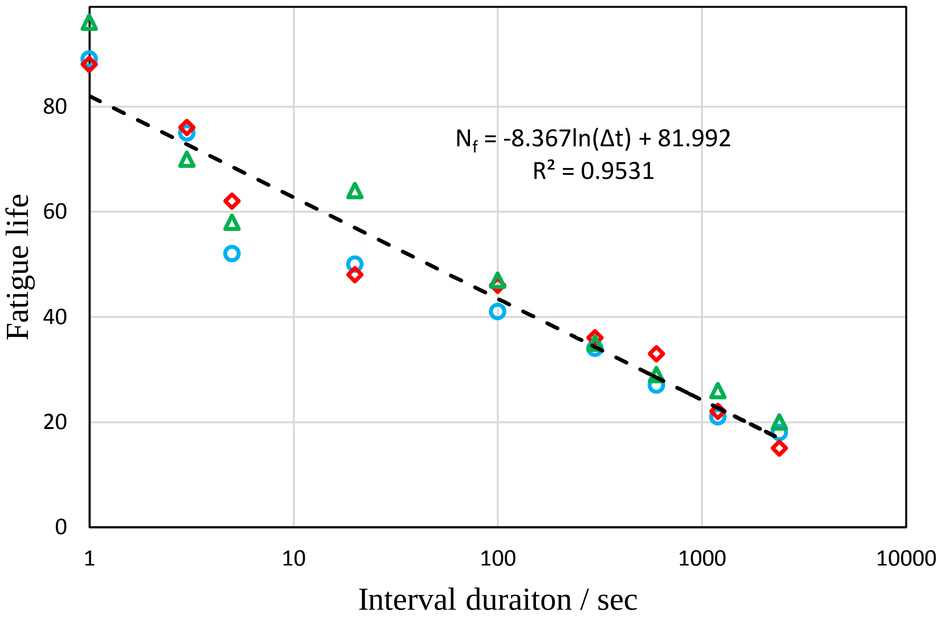

Fig. 5.24 Relationship between interval duration and fatigue life in 1502.group.

The possible empirical relationship between fatigue life and interval time is

$$N_f(t) = B_n(\Delta W^p)\, lg(\Delta t) + A_n N_f(0) \tag{5.1}$$

$N_f(0)$ is the conventional fatigue life; $N_f(t)$ is the discontinuous fatigue life; A_n is the stress weight; B_n is the interval weight. Since the 1502 tests are conducted only with the fix stress limits, A_n and B_n are constant. Substituting equation (4.8) into equation (5.1), $A_n = 4.58$, $B_n = -34.75$, $\varsigma = 17.61$

$$N_f(t) = B_n\, lg(\Delta t) + A_n(R_{max})^{-\varsigma} \tag{5.2}$$

5.6 Discontinuous fatigue constitutive model

The yield stress in A path is lower than normal value in B path, as shown in Fig. 5.25. Interval influence term k_1 is introduced to modify the strengthening coefficient R_f,

$$R_f = \left(\frac{\sum_{i=4}^{n} \gamma_{(i-1)}^{p} - (n-2)p}{\sum_{i=3}^{m} \gamma_{(i-1)}^{p} - (m-2)p} - k_1\right) k\sigma_f, i \geq 3 \tag{5.3}$$

The dilatancy function in discontinuous stress cycles (A cycles) for this case is the same with the normal stress cycles ie B cycles, (Fig. 5.26).

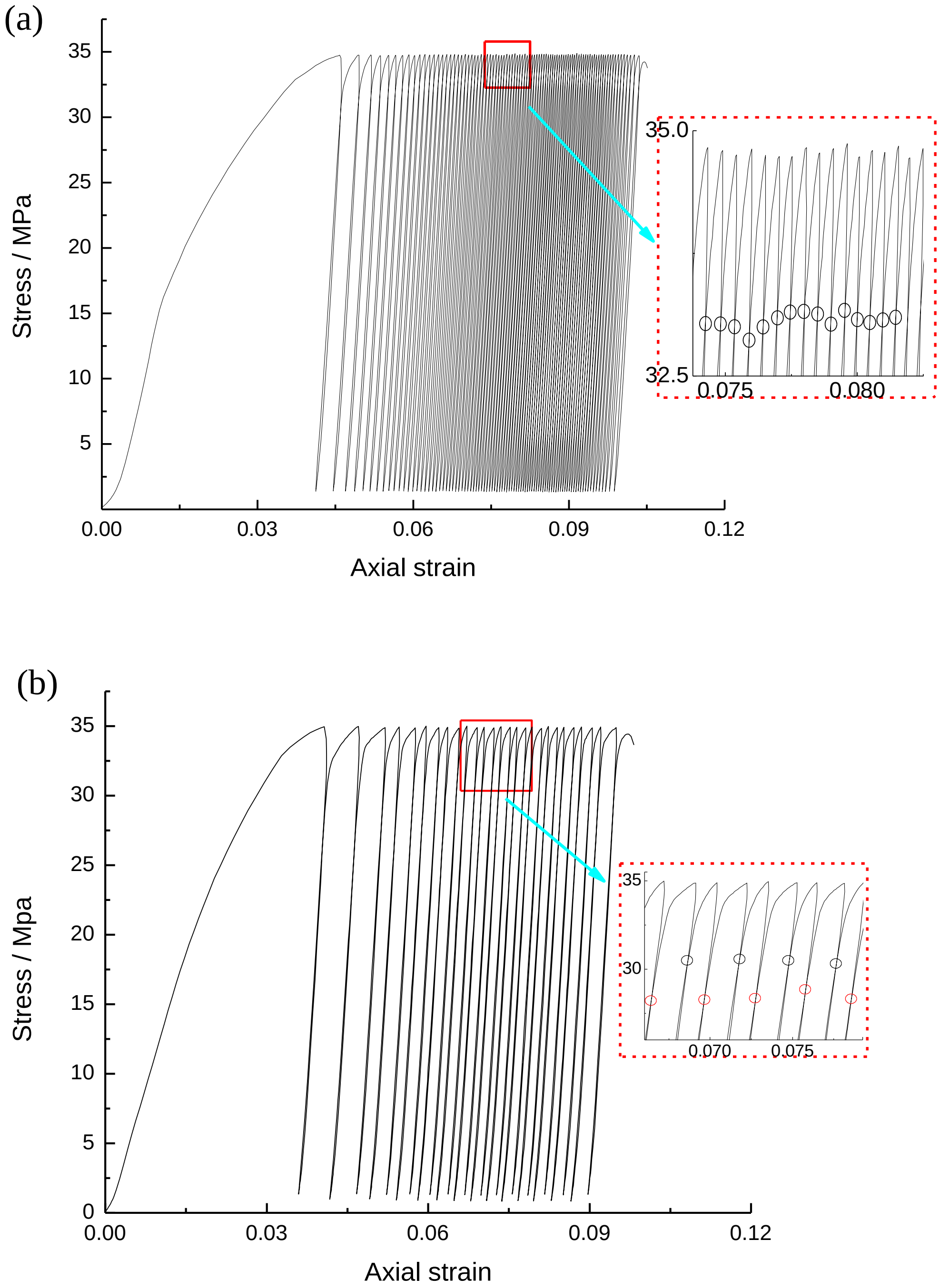

Fig. 5.25 Complete strain-stress curves of fatigue tests (a) without an interval (conventional test) and (b) with an interval of 5min. The selected local regions are enlarged and shown on the right for clarity. The hollow circles are marked as the yield point.

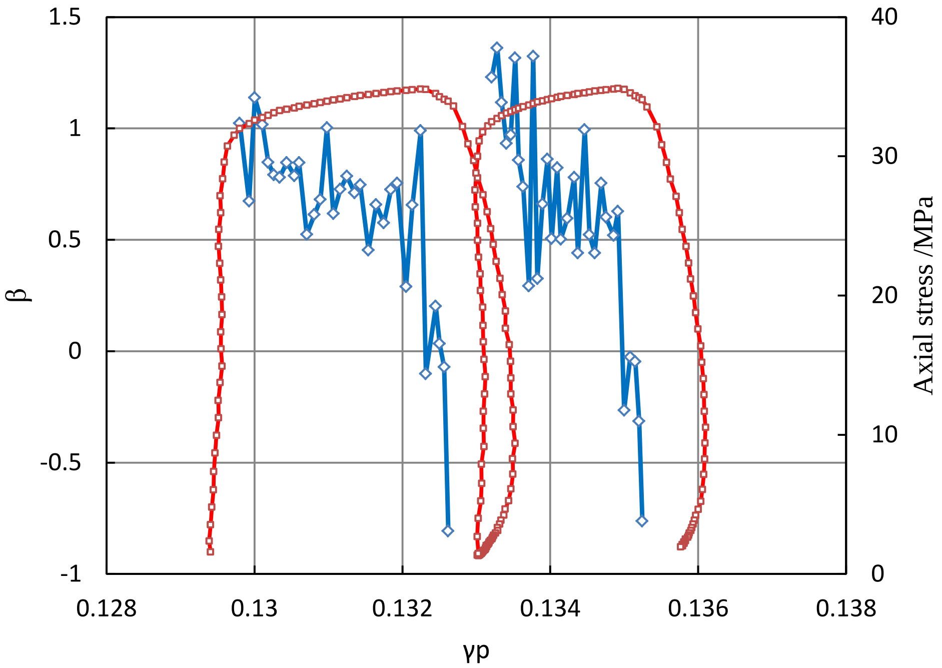

Fig. 5.26 Variation of dilatancy factor for two random cycles in the discontinuous loading test with Δt=5min. the red curve represents the stress variation while the blue broken line represents the dilatnacy factors.

5.7 Cause of discontinuous fatigue

Except for the compaction stage, the plastic deformation derives from two mechanisms: one is dislocation slippage; another is crack growth. Rock salt is a kind of natural complex NaCl crystalline structure, containing a variety of soluble and insoluble impurities. The impurities exist inside the crystal. Some of them are independent crystals, having different size and cleavage.

The impurity and NaCl crystals have different mechanical properties. The difference results in the residual stress between impurities and host material during cyclic loading.

After unloading, the external force is removed. Dislocations disperse under the residual stress. Intervals provide time for the salt to creep under the residual stress and damage the crystal lattice.

During reloading, some dislocations undergo a reverse movement, activating Bauschinger effect facilitating the dislocation slipping. During the intervals, the residual stress also accelerates the cracking. Therefore, in the A path reloading, the yield stress is smaller and plastic deformation is larger.

It is noteworthy that the dislocations and cracks develop to a new state after every cycle. If there is no interval before the cycle, the dislocations and cracks develop normally (like in B path), rather than like in A path.

As stated before, the lower stress ratio should not have influenced the fatigue properties, since the lower stress of different tests in 1201a2 group is adjusted below the yield stress. Here in my opinion the fatigue lives of samples decrease with smaller lower limit because the experimental time spent on the unloading is longer, equivalent to a longer time interval. The same loading velocity is applied in 1201a2 group, increasing the minimum stress means the time spent on the loading/unloading will save. Since the loading starts, less time will be provided for residual stress to damage the salt rock. Therefore, the plastic deformation is less as the minimum stress (or lower stress) increases.

5.8 Chapter summary

This chapter investigated the basic features of discontinuous fatigue, threshold of the time interval and the lower limit effect on the discontinuous fatigue. The results of discontinuous fatigue tests shows:

① Under the same stress and environmental conditions, the plastic strain rate of discontinuous fatigue is faster than that of conventional fatigue.

② Under the same stress and environmental conditions, the fatigue life of discontinuous fatigue is shorter than that of conventional fatigue.

③ Under the same stress and environmental conditions, the longer the time interval, the shorter the fatigue life.

④ The same features were also observed, as the lower limit increases from 5% to 45%.

⑤ The threshold of time interval was determined at 4h. Within 4h, the salt weakens obviously, while beyond 4 hour, the time interval does not affect the result.

⑥ The longer the time interval, the smaller the yield stress in the reloading.

⑦ The cause of the discontinuous fatigue is identified as residual strain and Bauschinger effect.

The discontinuous fatigue constitutive model is developed:

$$F_i = \begin{cases} \bar{\tau} - F_1(I_1, \gamma^p), i = 1 \\ \frac{\bar{\tau}}{1-\chi_{f_2}} - F_1(I_1, \gamma^p), i = 2 \\ \frac{\bar{\tau}}{1-\chi_{f_i}} + R_f - f\left(I_1, \gamma^p - \sum_{i=3}^{n} \gamma_{(i)}^p\right), i \geq 3 \end{cases} \tag{5.4a}$$

$$\chi_{f_i} = -0.0011 + \frac{0.00332}{\gamma_{YR}^p - 0.00612}\ , i \geq 2 \tag{5.4b}$$

$$\begin{cases} \gamma_{(R_i)}^p - \gamma_{(Y_i)}^p = 0.3\gamma_{(\sigma_{max})}^p, i \geq 2 \\ R_f = \left(\frac{\sum_{i=4}^{n} \gamma_{(i-1)}^p - (n-2)p}{\sum_{i=3}^{m} \gamma_{(i-1)}^p - (m-2)p} - k_1\right) k\sigma_f, i \geq 3 \end{cases} \tag{5.4c}$$

$$g_i = \beta + g_1(I_1, \gamma^p) \tag{5.5}$$

6 Evolution of fatigue damage in salt

Acoustic emission (AE) technology is a popular way of detecting fatigue damage. As a nondestructive testing method, this technology is widely used in experimental research and practical engineering. Acoustic emission is the transient elastic wave signal generated within the material due to sudden localized structure changes, for instance, dislocation slippage, microcrack growth. The count, strength, location of AE signal all can help understanding the damage process. During the deformation of crystals, there are various signal sources, as seen in Fig. 6.1.

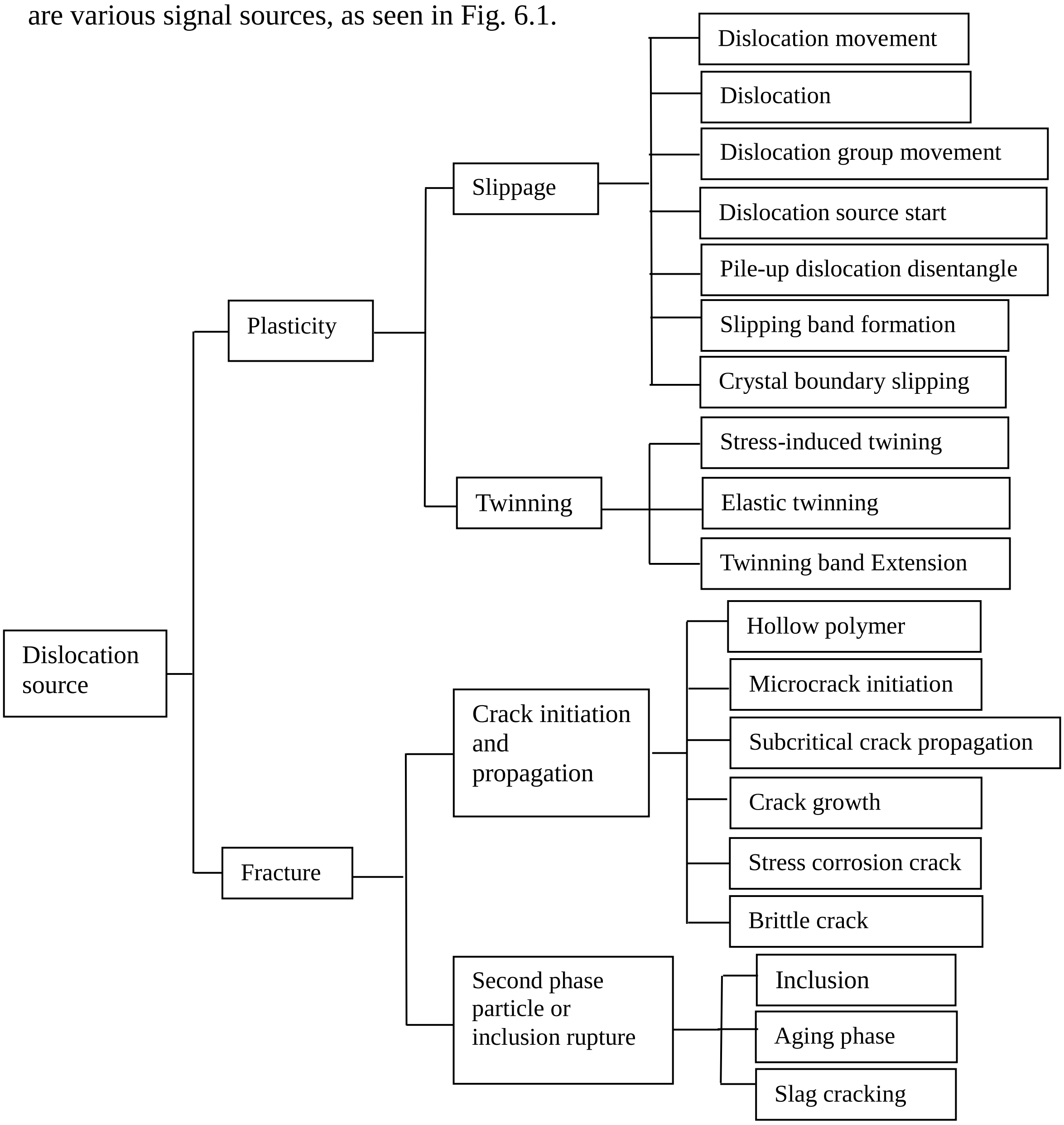

Fig. 6.1 Acoustic emission resources during deformation and rupture of crystals [130,131].

6.1 Experimental conditions

Acoustic emission test analysis system used in our experiments is from PAC (physical acoustic corporation) (Fig. 6.2). Main amplifier is set at 40 dB; the threshold value is set at 45 dB. Resonant frequency of sensor is 20～400kHz; Sampling frequency is 1×10^6 Hz.

AE probe is 8mm diameter resonant piezoelectric AE sensor. 4 probes are positioned on the surface of samples like in Fig. 4.1. To reduce the energy loss of AE signal and noise, the coupling agent spreads on the probe and sample surface.

Fig. 6.2 Acoustic emission monitoring equipment.

6.2 Damage evolution of continuous fatigue

6.2.1 Experimental design

To investigate the effect of upper stress limit, step loading was applied on one sample to detect the AE activities and fatigue damage. Regarding the experimental time, the loading velocity was adjusted to 6KN/s. The first step corresponds to 100 cycles, where the lower stress is set at 4MPa and the upper stress is set at 16MPa. The second step includes another 100 cycles, where the lower stress is unchanged and the upper stress is increased to 24MPa. The third step changes the upper stress to 32 MPa. The test is denoted as 1202 test.

6.2.2 AE experimental result

Fig. 6.3 shows the AE activities in 1202 test. In the first step (4~16MPa), the AE is hardly detectable. In the second step (4~24MPa), a large number of AE signals appear, particularly the most intensive in the first cycle, then decrease to a lower constant level.

In the third step (4~32MPa), the AE signals are more intensive than second step, but appear a similar variation trend. The constant level in the third cycle is higher than that in the second. This demonstrates that the first cycle in every step generates the highest damage to the salt sample. In every cycle, the AE signals grow with the stress at the level of high stress (Fig. 6.4), indicating that the AE signal arises just after the yield.

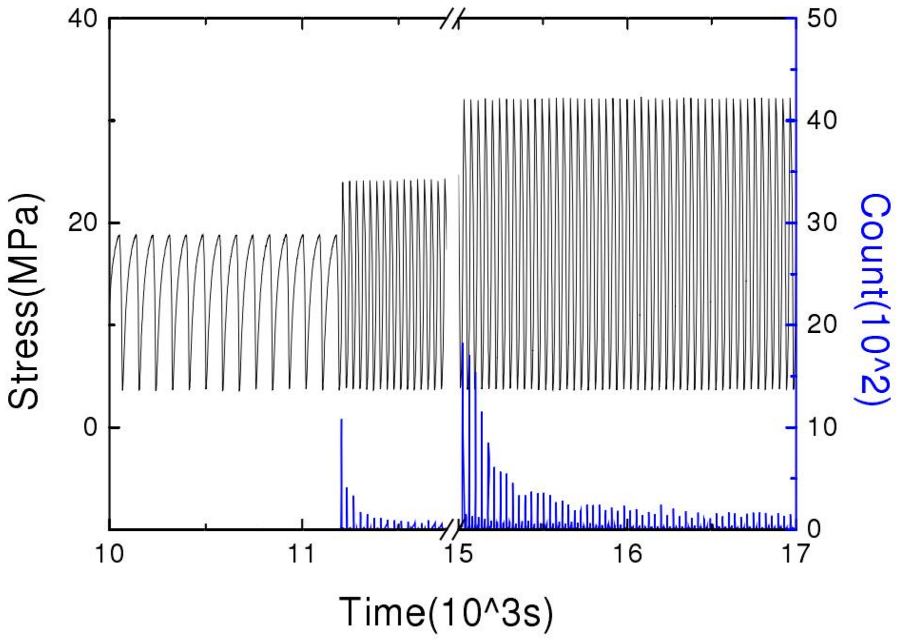

Fig. 6.3 Development of axial stress and AE signal in 1201 test.

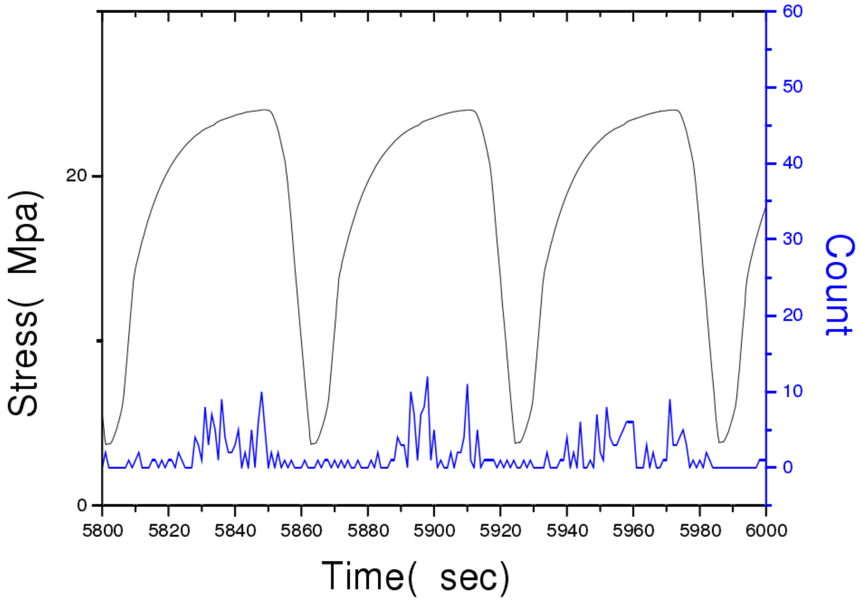

Fig. 6.4 Enlarged plot for the second step loading.

6.3 Damage evolution of discontinuous fatigue

6.3.1 Experimental design

Discontinuous fatigue AE testing was conducted on the 1501 and 1502 tests by applying AE testing devices. The devices are totally the same as in the previous 1202 AE tests. The test scheme and loading path are not repeated again here.

6.3.2 AE experimental results

Fig. 6.5 shows the evolution of some tested parameters of AE signals from 1502 test with 30 sec interval. The three parameters (strain, AE count and AE energy) show similar relationship with each other during the process of fatigue.

As in the 1202 test, massive AE signals are detected in the first stress cycle. In the compaction stage, the relative slippage between walls of compacted pores creates AE signals, forming the main cause of the AE emissions. As the loading continues, dislocation sources are activated and emit dislocations, the cause of the AE activities in plastic stage. In the last one or two cycles, dislocations annihilate and microcracks connect generating AE signals.

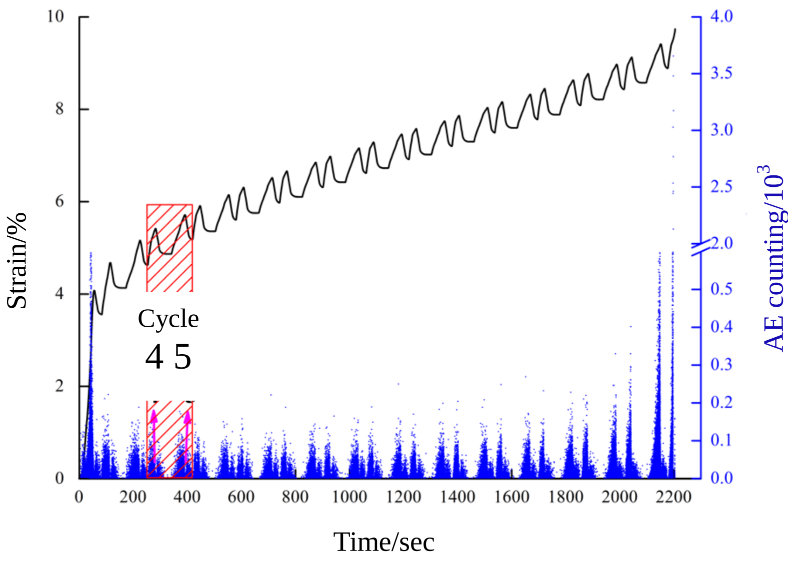

(a) AE counts number

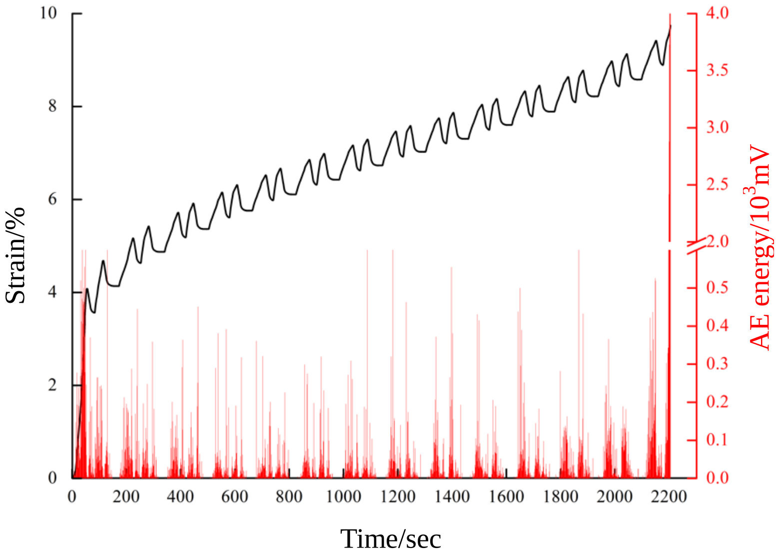

(b) AE energy

Fig. 6.5 AE characteristics of the test (Δt=30 sec) in 1502.group tests

In intermediate stage of test, AE signals develop steadily. There is no doubt that dislocations take part in the generation of AE, while the microcracks initiation at this stage is unclear. By using optical microscope, Most area of the cut surface is found intact by optical microscope observations, but some microcracks with 1~3μm width and 2~5 μm length are also observed (Fig. 6.6).

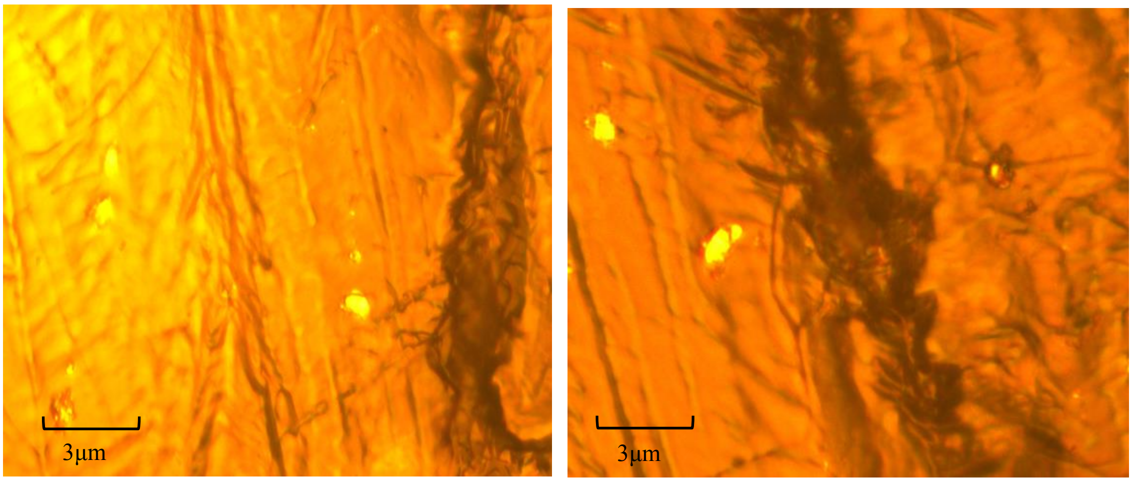

Fig. 6.6 Transection images of salt sample (Δt=30 sec) in 1301 group captured by optical microscope

The intrant time intervals intensify the AE of the following stress cycle. For clear exhibition, the section of Fig. 6.4a from 655sec to 910sec is enlarged. It can be found that in the cycles from A path, AE are more active than from B path. Additionally, there is hardly AE signal detected during the time intervals, indicating the self-adjusting of salt rock is low-intensity and did not make much damage to salt sample themselves.

The AE signals during unloading are caused by salt creep or fluctuation of confining pressure when close to the designed target.

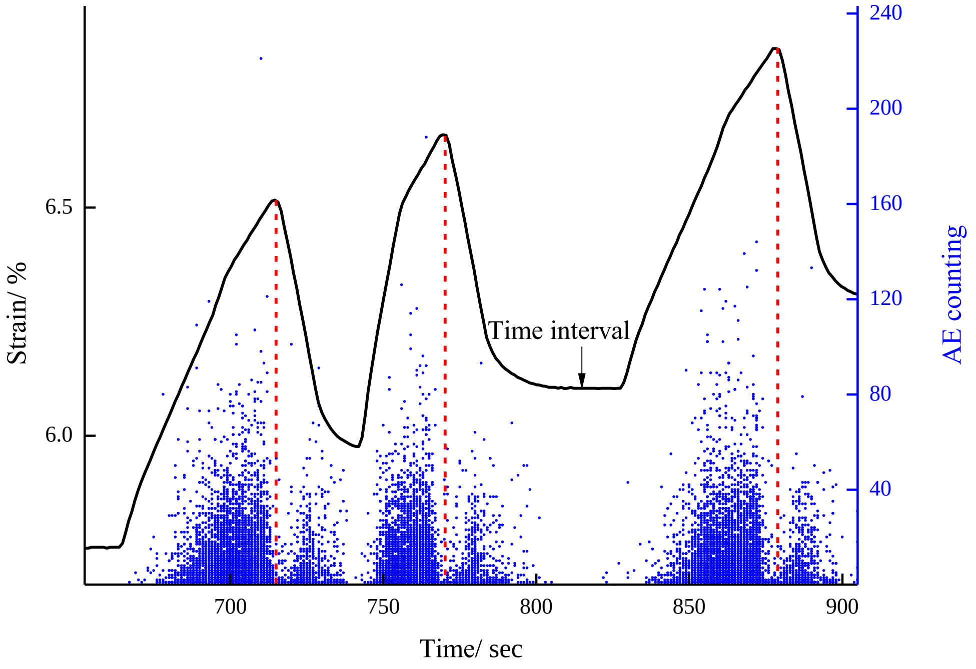

Fig. 6.7 Enlarged zone for figure 6.4a

By comparing the AE results between conventional and discontinuous fatigue tests, it is found that the intensity of AE activities, the residual strain and microcracking intensity are proportional.

Within the mega-cycle of 1501 test, the AE shows the similar tendency with residual strain (Fig. 6.10). Overall, AEs increase with stress cycles while the residual strain develops in a different way similar to that in conventional test. As shown in Fig. 6.8, the AE of discontinuous fatigue (1501) test shows a different tendency from the conventional fatigue test. This indicates that the intensity of AE activity is not directly linked with residual strain, but to microcracking.

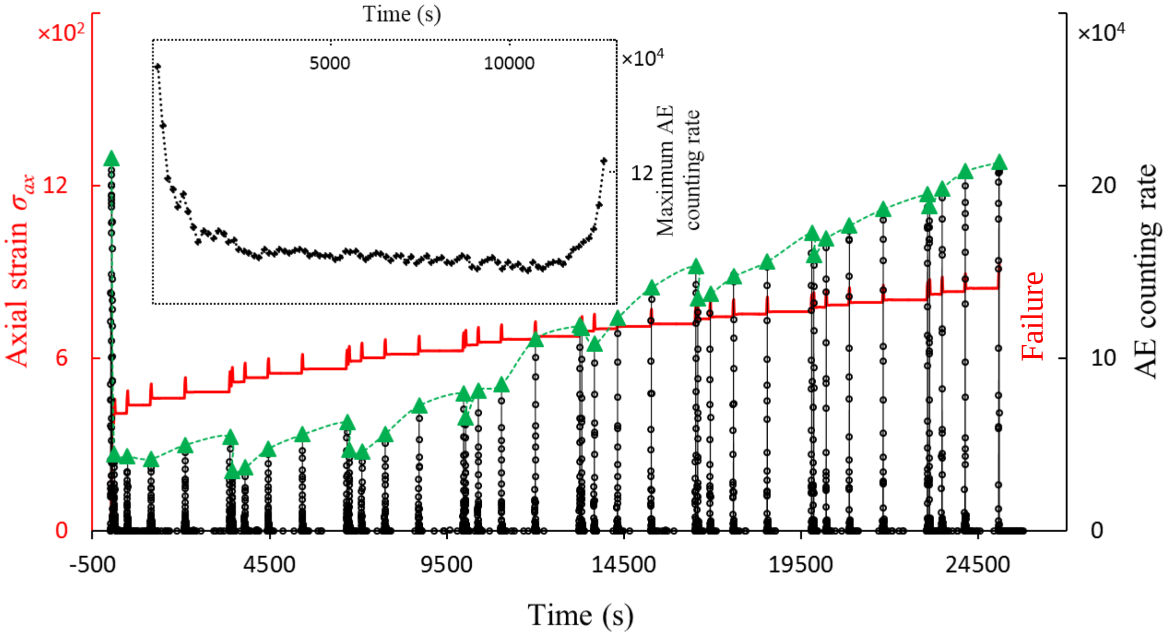

Fig. 6.8 Variation of the counting rate of AEs with time and the corresponding axial strain ε_{ax} in. The maximal counting rate in each cycle is highlighted in green. The plot of the maximal counting rate versus time for conventional fatigue test is shown in the inset.

6.4 Damage inertia in discontinuous fatigue test

Fig. 6.9 shows the residual strain and AE activity in 1301 tests with the intervals of 5sec, 30sec and 60sec. It is known that the cracks propagate and connect rapidly in the last several cycles and the plastic deformation develops rapidly in the first several cycles. In Fig.6.9, AE activity is of low-intensity in the first several cycles, high-intensity in the last several cycles, indicating a strong link to microcracking.

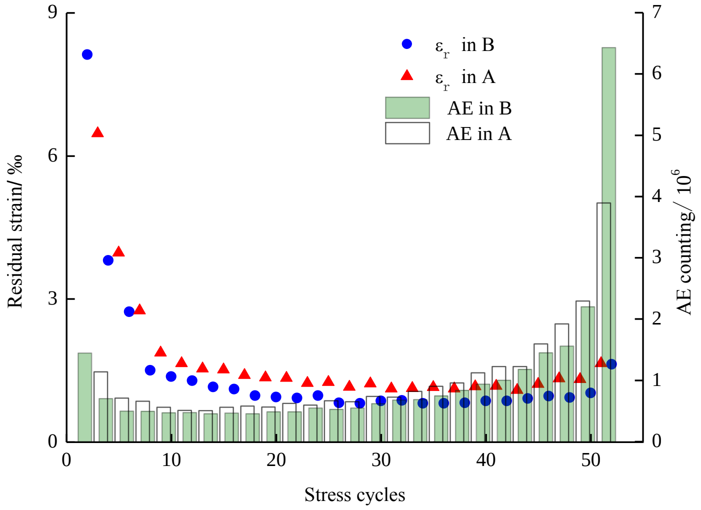

(a) Discontinuous fatigue test (Δt=5sec)

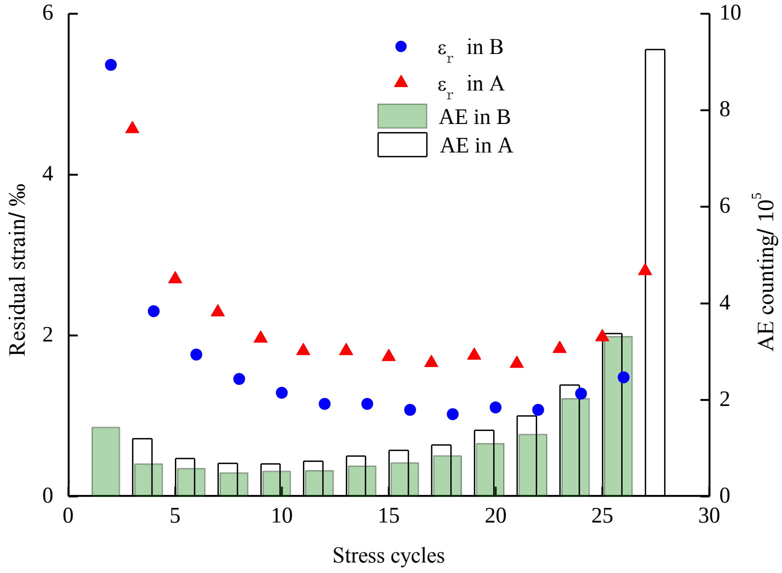

(b) Discontinuous fatigue test (Δt=30sec)

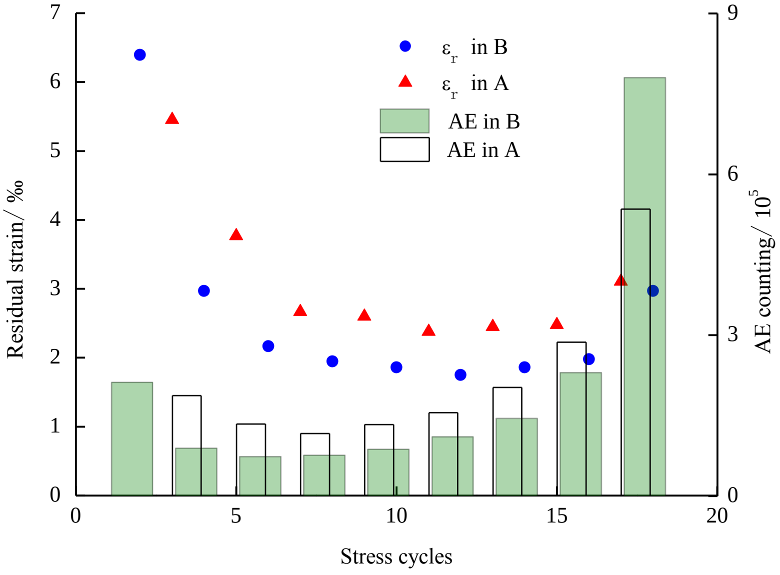

(c) Discontinuous fatigue test (Δt=60sec)

Fig.6.9 Histograms of sum of counts and the values of residual strain during each circle

Fig. 6.10 shows the AE counting rate rises as the time intervals become longer within the mega-cycles. However, the AE counting rate from the cycles following the 0min interval is always higher than that following 5min cycle. We can understand that the cracks develop faster in the cycles following 0min interval than the next cycle while the residual strain develop less than the next cycle.

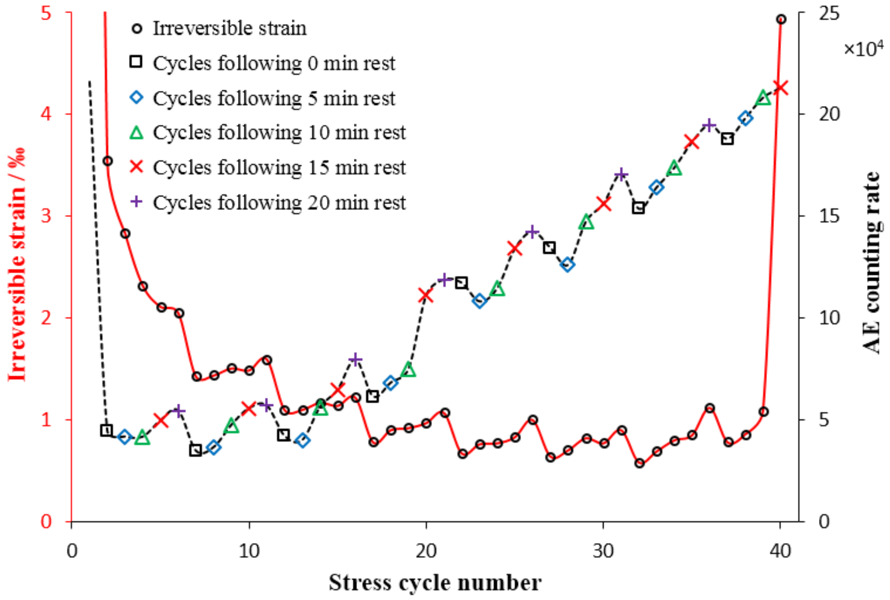

Fig.6.10 Sum of counts during each circle and the curves of residual strain

6.4.1 Damage inertia of salt

The question arises, how the more AE (or microcracks) are generated in the cycles following 0min interval than in the cycles following 5min interval. To address this question, the AE events are divided into two types. The first linked to microcracking, is denoted as C type, which could create less plastic deformation, but more AE events. The other linked to dislocations, is denoted as D type, able to create more plastic deformation, but rare detectable AE events. Dislocations could annihilate to transforming into microcracks. It is understandable that proportion of C-type events is higher in the cycles following 0min interval than the normal value like in the cycles following 5min interval.

What causes this? Time interval could promote the development of dislocations and microcracks. In the cycles following 20min interval, lots of C-type and D-type AE events produced. With the absence of time interval the dislocations newly produce less in the next cycles. However, the dislocations producing in the cycles following 20min interval could transform into microcracks and motivate numerous D-type AE events. Therefore the AE is active in the cycles following 0min interval, but the plastic strain is small. This phenomenon would be called as damage inertia.

6.4.2 Effect of damage inertia

Damage inertia may lead to more C-type damage, meaning the cracks develop more quickly than residual strain. Following the discontinuous cyclic loading path, the sample develops the plastic deformation relatively slowly, therefore the total plastic deformation at failure is smaller than the conventional value (see line 1 and others in Fig. 6.11). As the intervals elongate, the inertia enhances, the total plastic deformation becomes smaller.

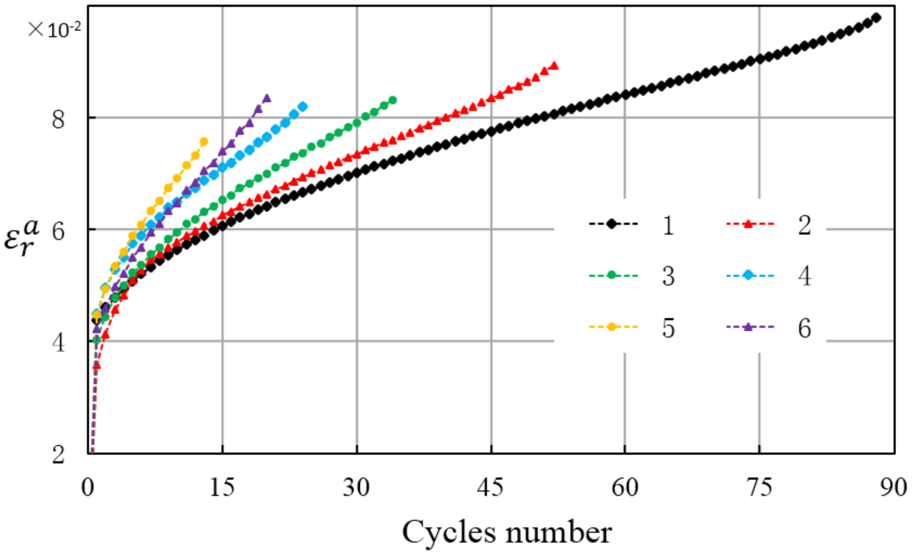

Fig. 6.11 Accumulated residual strain ε_r^a in the tests with loading path 2 for different duration Δt of the intervals. 1, $\Delta t = 0$ min; 2, Δt=0.1 min; 3, Δt=5 min; 4, Δt=10 min; 5, Δt=15 min; 6, Δt=20 min. ε_r^a is a sum of the residual nominal strains.

6.5 Chapter summary

AE testing technology could help to understand the damage evolution of salt in fatigue tests. This chapter compared the AE results between conventional fatigue tests and discontinuous fatigue test, verified the promotion effect of time interval on the damage development and discovered some special characteristics on fatigue damage evolution.

In conventional fatigue tests, AE activities and plastic deformation develop congruently. The higher the upper stress limits, the stronger the AE signals. In discontinuous fatigue tests, AE signals are stronger in A path than those in B path.

Damage inertia is put forward: in the discontinuous fatigue tests, numerous dislocations generating in the previous stress cycles remain, transform into cracks in the next cycle and causing more damages. Because of the effect of damage inertia, the total plastic deformation becomes smaller when the interval time is longer.

7 Conclusions and Prospects

Plastic volumetric expansion of salt is closely related with the permeability, affecting the efficiency of underground cavern storage. The thesis studied the elasoplastic behavior, particularly the dilatancy of salt under discontinuous cyclic loading. From the prospective of dislocation theory, the mechanical performance was explained. By transforming the non-associated flow rule, the constitutive model based on the dilatancy function and yield function was developed.

7.1 Conclusions

① Plastic volumetric strain is caused by three mechanisms: pore reduction, dislocation slippage and microcrack growth. Strain hardening results from the piling up of dislocations and leads to the stress increase. Volumetric expansion is caused by the lattice distortion due to dislocations as well as initiation, growth and connection of microcracks.

② By transforming the plastic potential function, a dilatancy function was developed to characterize the plastic flow direction. Based on the conventional compression tests, an elastoplastic constitutive model (including yield function and dilatancy function) was developed by considering the combined effect of hydrostatic pressure and loading history.

$$\begin{cases} F = \bar{\tau} - a(\bar{\gamma}^p){I_1}^2 - b(\bar{\gamma}^p)I_1 - c(\bar{\gamma}^p) \\ \quad g = \beta + m(\bar{\gamma}^p)I_1 + n(\bar{\gamma}^p) \end{cases} \tag{7.1}$$

③ Conventional fatigue properties of salt were experimentally studied with different stress ratio, loading frequency, temperature and confining pressure. The higher the upper stress ratio and the higher the temperature and the larger the confining pressure, the shorter the fatigue life of salt.

④ Discontinuous fatigue properties were studied.

Time interval promotes the development of plastic deformation of salt.

Time interval reduces the fatigue life of salt.

If the time interval is larger, the plastic deformation (residual strain) in the following cycle is larger and fatigue life of salt is smaller.

If less than 4 hours, the time intervals produce weakening the salt sample; if time interval exceeds 4h, the effect is negligible.

Time interval could lead to the premature failure of salt: the total plastic deformation reduces as the interval time increases.

⑤ Damage inertia was proposed for the discontinuous fatigue. In previous cycle the salt could generates too much dislocation damage, which would transform into more microcrack damage in the next cycle.

⑥ Weakening coefficient was introduced to describe the deformation of yield surface during unloading. Dynamic hardening factor was introduced to describe the movement during cyclic loading.

⑦ Yield surface evolves because of the time interval effect. In the constitutive model; an interval coefficient was introduced into dynamic hardening factor. Dilatancy function was developed to characterize the plastic flow direction. Dilatancy factor in discontinuous cyclic loading develops as in uniaxial compression test.

$$F_i = \begin{cases} \bar{\tau} - F_1(I_1, \gamma^p), i = 1 \\ \frac{\bar{\tau}}{1-\chi_{f_2}} - F_1(I_1, \gamma^p), i = 2 \\ \frac{\bar{\tau}}{1-\chi_{f_i}} + R_f - f\left(I_1, \gamma^p - \sum_{i=3}^{n} \gamma_{(i)}^p\right), i \geq 3 \end{cases} \tag{7.2a}$$

$$R_f = \left(\frac{\sum_{i=4}^{n} \gamma_{(i-1)}^p - (n-2)p}{\sum_{i=3}^{m} \gamma_{(i-1)}^p - (m-2)p} - k_1\right) k \sigma_f, i \geq 3 \tag{7.2b}$$

$$g_i = \beta + g_1(I_1, \gamma^p) \tag{7.3}$$

8) Essential cause of the discontinuous cyclic fatigue is identified as the residual stress, which temporarily or permanently changes the material properties.

7.2 Originalities

① Dislocation theory was adopted to explain the mechanical performance of salt in conventional compression tests, cyclic loading and discontinuous cyclic loading.

② Plastic potential function is replaced by the dilatancy function, sampling the formulation of constitutive model. This model takes into account the hydrostatic pressure and the loading history into account.

③ The discontinuous fatigue tests are conducted and the residual stress was identified as the essential cause of discontinuous fatigue damage.

7.3 Prospects

① Application of the constitutive model: the developed constitutive model can be implemented into the numerical code for calculation (modeling) the plastic deformation, volumetric shrinkage ratio and isolation effect of the underground salt storages under different working conditions.

② Complemented the constitutive model with creep the creep relations.

③ Estimate the dimension of the residual stresses.

④ Conduct the triaxial discontinuous fatigue tests and triaxial extension tests.

Acknowledgement

Every episode a is precious treasure for me.

2007 I left my home and went to Chongqing to start my College life. As a newcomer, I didn’t know anything about the new city but I was greatly helped by my schoolmates and made nice friend with them.

First I would like to thank my two supervisors. During my doctoral study, they gave much valuable suggestions on my life and academic research and helped me to avoid detours. My Chinese supervisor, Prof. Deyi JIANG, is very warmhearted and always held my hand when I was confused or frustrated. He directed the thesis research program and helped me amend the test scheme.

French supervisor is a world distinguished scholar in Geomechanics. He helped me to open my eyes on the international academic circumstance and taught me the rigorous attitude of scholarship. I remember he gave a significant presentation about the accurate constitutive model, which impressed me deeply, for geomaterials in Geomod 2016. Here, thanks so much for his attention to the thesis.

Finally, I sincerely thank my younger colleague Junchao CHEN who helped me in conducting the fatigue experiments and all the experts and professors who have reviewed the papers in their busy schedules.

Jinyang FAN

March 2017 at Chongqing

References

[1] Y. Guo, C. Yang, H. Mao, Mechanical properties of Jintan mine rock salt under complex stress paths, International Journal of Rock Mechanics and Mining Sciences 56 (2012) 54-61.

[2] Y. Li, W. Liu, C. Yang, J.J.K. Daemen, Experimental investigation of mechanical behavior of bedded rock salt containing inclined interlayer, International Journal of Rock Mechanics and Mining Sciences 69 (2014) 39-49.

[3] Y. Li, C. Yang, On fracture saturation in layered rocks, International Journal of Rock Mechanics and Mining Sciences 44(6) (2007) 936-941.

[4] B. Liu, L. Yang, T. Liang, C. Tang, Stress analysis of aspherical coated particle with inner pressure, Nuclear Engineering and Design 251 (2012) 381-384.

[5] W. Liu, Y. Li, C. Yang, J.J.K. Daemen, Y. Yang, G. Zhang, Permeability characteristics of mudstone cap rock and interlayers in bedded salt formations and tightness assessment for underground gas storage caverns, Engineering Geology 193 (2015) 212-223.

[6] T. Wang, C. Yang, H. Ma, J.J.K. Daemen, H. Wu, Safety evaluation of gas storage caverns located close to a tectonic fault, Journal of Natural Gas Science and Engineering 23 (2015) 281-293.

[7] T. Wang, C. Yang, X. Shi, H. Ma, Y. Li, Y. Yang, J.J.K. Daemen, Failure analysis of thick interlayer from leaching of bedded salt caverns, International Journal of Rock Mechanics and Mining Sciences 73 (2015) 175-183.

[8] C. Yang, T. Wang, Y. Li, H. Yang, J. Li, D.a. Qu, B. Xu, Y. Yang, J.J.K. Daemen, Feasibility analysis of using abandoned salt caverns for large-scale underground energy storage in China, Applied Energy 137 (2015) 467-481.

[9] C. Li, Y. Liu, G. Li, J. Li, D. Zhu, W. Jia, G. Li, Y. Zhi, X. Zhai, Evaluation of wind energy resource and wind turbine characteristics at two locations in China, Technology in Society 47 (2016) 121-128.

[10] T. Wang, G. Wu, J. Chen, P. Cui, Z. Chen, Y. Yan, Y. Zhang, M. Li, D. Niu, B. Li, H. Chen, Integration of solar technology to modern greenhouse in China: Current status, challenges and prospect, Renewable and Sustainable Energy Reviews 70 (2017) 1178-1188.

[11] X.J. Yang, H. Hu, T. Tan, J. Li, China's renewable energy goals by 2050, Environmental Development 20 (2016) 83-90.

[12] Y. Li, D. Nie, X. Zhao, Y. Li, Market structure and performance: An empirical study of the

Chinese solar cell industry, Renewable and Sustainable Energy Reviews 70 (2017) 78-82.

[13] X. Zhang, C. Ma, X. Song, Y. Zhou, W. Chen, The impacts of wind technology advancement on future global energy, Applied Energy 184 (2016) 1033-1037.

[14] T.A.C. Maia, J.E.M. Barros, B.J. Cardoso Filho, M.P. Porto, Experimental performance of a low cost micro-CAES generation system, Applied Energy 182 (2016) 358-364.

[15] C. Guo, L. Pan, K. Zhang, C.M. Oldenburg, C. Li, Y. Li, Comparison of compressed air energy storage process in aquifers and caverns based on the Huntorf CAES plant, Applied Energy 181 (2016) 342-356.

[16] E.A. Bouman, M.M. Øberg, E.G. Hertwich, Environmental impacts of balancing offshore wind power with compressed air energy storage (CAES), Energy 95 (2016) 91-98.

[17] A. Sciacovelli, Y. Li, H. Chen, Y. Wu, J. Wang, S. Garvey, Y. Ding, Dynamic simulation of Adiabatic Compressed Air Energy Storage (A-CAES) plant with integrated thermal storage – Link between components performance and plant performance, Applied Energy 185, Part 1 (2017) 16-28.

[18] C. Xia, Y. Zhou, S. Zhou, P. Zhang, F. Wang, A simplified and unified analytical solution for temperature and pressure variations in compressed air energy storage caverns, Renewable Energy 74 (2015) 718-726.

[19] M. Raju, S. Kumar Khaitan, Modeling and simulation of compressed air storage in caverns: A case study of the Huntorf plant, Applied Energy 89(1) (2012) 474-481.

[20] M. Budt, D. Wolf, R. Span, J. Yan, A review on compressed air energy storage: Basic principles, past milestones and recent developments, Applied Energy 170 (2016) 250-268.

[21] J. Fan, J. Chen, D. Jiang, A. Chemenda, J. Chen, J. Ambre, Discontinuous cyclic loading tests of salt with acoustic emission monitoring, International Journal of Fatigue 94(1) (2017) 140-144.

[22] J. Fan, J. Chen, D. Jiang, S. Ren, J. Wu, Fatigue properties of rock salt subjected to interval cyclic pressure, International Journal of Fatigue 90 (2016) 109-115.

[23] D. Jiang, J. Fan, J. Chen, L. Li, Y. Cui, A mechanism of fatigue in salt under discontinuous cycle loading, International Journal of Rock Mechanics and Mining Sciences 86 (2016) 255-260.

[24] D. Jiang, J. Fan, J. Chen, l. Li, S. Ren, Research on compression-shear fatigue properties and dislocation damage of salt rock, Chinese Journal of Rock Mechanics and Engineering 34(05) (2015) 895-906.

[25] I. Lillemäe, S. Liinalampi, H. Remes, A. Itävuo, A. Niemelä, Fatigue strength of thin laser-hybrid welded full-scale deck structure, International Journal of Fatigue 95 (2017)

282-292.

[26] Z.J. Zhang, J.C. Pang, Z.F. Zhang, Optimizing the fatigue strength of ultrafine-grained Cu-Zn alloys, Materials Science and Engineering: A 666 (2016) 305-313.

[27] N. Erarslan, Microstructural investigation of subcritical crack propagation and Fracture Process Zone (FPZ) by the reduction of rock fracture toughness under cyclic loading, Engineering Geology 208 (2016) 181-190.

[28] B. Sun, L. Yang, W. Bai, Q. Liu, X. Xu, Experimental investigation on porosity reduction of a coarsely crushed rock layer subject to vertically cyclic loading, Cold Regions Science and Technology 104–105 (2014) 88-96.

[29] A. Pouya, C. Zhu, C. Arson, Micro–macro approach of salt viscous fatigue under cyclic loading, Mechanics of Materials 93 (2016) 13-31.

[30] D. Song, E. Wang, J. Liu, Relationship between EMR and dissipated energy of coal rock mass during cyclic loading process, Safety Science 50(4) (2012) 751-760.

[31] E. Liu, S. He, Effects of cyclic dynamic loading on the mechanical properties of intact rock samples under confining pressure conditions, Engineering Geology 125 (2012) 81-91.

[32] L.M. Brown, P.L. Pratt, Strain ageing in CdCl2-doped rock salt, Philosophical Magazine A 8(89) (1963) 717-734.

[33] D.M. Cruden, The static fatigue of brittle rock under uniaxial compression, International Journal of Rock Mechanics and Mining Sciences & Geomechanics Abstracts 11(2) (1974) 67-73.

[34] B.C. Haimson, Mechanical behaviour of rock under cyclic loading 9F, 1T, 11R. Proc. 3rd Congress ISRM, Denver, 1974, 1974, pp. 373-378.

[35] F. APPEL, Snoek rearrangement during strain aging in Calcium-doped NaCl crystals, Materials Science and Engineering: A 50 (1980) 199-204.

[36] E.O. M., J. Soullard, C. Zaldo, F. Agulló-lópez, Hardening of NaCl single crystals induced by Eu obstacles, Philosophical Magazine A 50(3) (1985) 425-440.

[37] X. Niu, T. Luo, J. Lu, Y. Xiang, Dislocation climb models from atomistic scheme to dislocation dynamics, Journal of the Mechanics and Physics of Solids 99 (2017) 242-258.

[38] M. Stricker, D. Weygand, P. Gumbsch, Irreversibility of dislocation motion under cyclic loading due to strain gradients, Scripta Materialia 129 (2017) 69-73.

[39] P. Zhang, J.-g. Xu, N. Li, Fatigue properties analysis of cracked rock based on fracture evolution process, Journal of Central South University of Technology 15(1) 95-99.

[40] D.L. Chopp, N. Sukumar, Fatigue crack propagation of multiple coplanar cracks with the coupled extended finite element/fast marching method, International Journal of Engineering

Science 41(8) (2003) 845-869.

[41] M. Stolarska, D.L. Chopp, Modeling thermal fatigue cracking in integrated circuits by level sets and the extended finite element method, International Journal of Engineering Science 41(20) (2003) 2381-2410.

[42] M.-C. Eppes, A. Willis, J. Molaro, S. Abernathy, B. Zhou, Cracks in Martian boulders exhibit preferred orientations that point to solar-induced thermal stress, Nature Communications 6 (2015) 6712.

[43] K.C. Le, V.N. Tran, Stress and dislocation distributions near a crack tip in ductile single crystals, International Journal of Engineering Science 102 (2016) 4-11.

[44] K. Sharma, T.Q. Bui, R.R. Bhargava, T. Yu, J. Lei, S. Hirose, Numerical studies of an array of equidistant semi-permeable inclined cracks in 2-D piezoelectric strip using distributed dislocation method, International Journal of Solids and Structures 80 (2016) 137-145.

[45] C. Fu, H. Ye, X. Jin, D. Yan, N. Jin, Z. Peng, Chloride penetration into concrete damaged by uniaxial tensile fatigue loading, Construction and Building Materials 125 (2016) 714-723.

[46] X. Chen, J. Bu, X. Fan, J. Lu, L. Xu, Effect of loading frequency and stress level on low cycle fatigue behavior of plain concrete in direct tension, Construction and Building Materials 133 (2017) 367-375.

[47] J.-T. Zhu, X.-L. Wang, X.-D. Kang, K. Li, Analysis of interfacial bonding characteristics of CFRP-concrete under fatigue loading, Construction and Building Materials 126 (2016) 823-833.

[48] W. Dong, Z. Wu, X. Zhou, N. Wang, G. Kastiukas, An experimental study on crack propagation at rock-concrete interface using digital image correlation technique, Engineering Fracture Mechanics 171 (2017) 50-63.

[49] M.N. Bagde, V. Petroš, Fatigue properties of intact sandstone samples subjected to dynamic uniaxial cyclical loading, International Journal of Rock Mechanics and Mining Sciences 42(2) (2005) 237-250.

[50] S.K. Singh, Relationship among fatigue strength, mean grain size and compressive strength of a rock, Rock Mechanics and Rock Engineering 21(4) (1988) 271-276.

[51] M. Singh, Applicability of a Constitutive Model to Jointed Block Mass, Rock Mechanics and Rock Engineering 33(2) (2000) 141-147.

[52] R. Song, B. Yue-ming, Z. Jing-Peng, J. De-yi, Y. Chun-he, Experimental investigation of the fatigue properties of salt rock, International Journal of Rock Mechanics and Mining Sciences 64 (2013) 68-72.

[53] A. Momeni, M. Karakus, G.R. Khanlari, M. Heidari, Effects of cyclic loading on the

mechanical properties of a granite, International Journal of Rock Mechanics and Mining Sciences 77 (2015) 89-96.

[54] Y.-L. Chen, J. Ni, W. Shao, R. Azzam, Experimental study on the influence of temperature on the mechanical properties of granite under uni-axial compression and fatigue loading, International Journal of Rock Mechanics and Mining Sciences 56 (2012) 62-66.

[55] H.R. Nejati, A. Ghazvinian, Brittleness Effect on Rock Fatigue Damage Evolution, Rock Mechanics and Rock Engineering 47(5) (2014) 1839-1848.

[56] M. Migliazza, A.M. Ferrero, A. Spagnoli, Experimental investigation on crack propagation in Carrara marble subjected to cyclic loads, International Journal of Rock Mechanics and Mining Sciences 48(6) (2011) 1038-1044.

[57] A.M. Ferrero, M. Migliazza, A. Spagnoli, Theoretical modelling of bowing in cracked marble slabs under cyclic thermal loading, Construction and Building Materials 23(6) (2009) 2151-2159.

[58] A.M. Ferrero, M.R. Migliazza, Theoretical and numerical study on uniaxial compressive behaviour of marl, Mechanics of Materials 41(5) (2009) 561-572.

[59] J.-L. Le, J. Manning, J.F. Labuz, Scaling of fatigue crack growth in rock, International Journal of Rock Mechanics and Mining Sciences 72 (2014) 71-79.

[60] Y. Liu, F. Dai, T. Zhao, N.-w. Xu, Numerical Investigation of the Dynamic Properties of Intermittent Jointed Rock Models Subjected to Cyclic Uniaxial Compression, Rock Mechanics and Rock Engineering (2016) 1-24.

[61] N. Erarslan, D.J. Williams, The damage mechanism of rock fatigue and its relationship to the fracture toughness of rocks, International Journal of Rock Mechanics and Mining Sciences 56 (2012) 15-26.

[62] N. Erarslan, D.J. Williams, Mechanism of rock fatigue damage in terms of fracturing modes, International Journal of Fatigue 43 (2012) 76-89.

[63] J. Xiao, D. Ding, G. Xu, F. Jiang, Waveform effect on quasi-dynamic loading condition and the mechanical properties of brittle materials, International Journal of Rock Mechanics and Mining Sciences 45(4) (2008) 621-626.

[64] Z. Wang, S. Li, L. Qiao, Q. Zhang, Finite element analysis of the hydro-mechanical behavior of an underground crude oil storage facility in granite subject to cyclic loading during operation, International Journal of Rock Mechanics and Mining Sciences 73 (2015) 70-81.

[65] Z. Wang, S. Li, L. Qiao, J. Zhao, Fatigue Behavior of Granite Subjected to Cyclic Loading Under Triaxial Compression Condition, Rock Mechanics and Rock Engineering 46(6) (2013) 1603-1615.

[66] N. Gatelier, F. Pellet, B. Loret, Mechanical damage of an anisotropic porous rock in cyclic triaxial tests, International Journal of Rock Mechanics and Mining Sciences 39(3) (2002) 335-354.

[67] V. Gischig, G. Preisig, E. Eberhardt, Numerical Investigation of Seismically Induced Rock Mass Fatigue as a Mechanism Contributing to the Progressive Failure of Deep-Seated Landslides, Rock Mechanics and Rock Engineering 49(6) (2016) 2457-2478.

[68] G. Preisig, E. Eberhardt, M. Smithyman, A. Preh, L. Bonzanigo, Hydromechanical Rock Mass Fatigue in Deep-Seated Landslides Accompanying Seasonal Variations in Pore Pressures, Rock Mechanics and Rock Engineering 49(6) (2016) 2333-2351.

[69] X. Luo, N. Jiang, M. Wang, Y. Xu, Response of Leptynite Subjected to Repeated Impact Loading, Rock Mechanics and Rock Engineering 49(10) (2016) 4137-4141.

[70] T. Lenoir, M. Preteseille, S. Ricordel, Contribution of the fiber reinforcement on the fatigue behavior of two cement-modified soils, International Journal of Fatigue 93, Part 1 (2016) 71-81.

[71] M. Preteseille, T. Lenoir, Structural test at the laboratory scale for the utilization of stabilized fine-grained soils in the subgrades of High Speed Rail infrastructures: Experimental aspects, International Journal of Fatigue 82, Part 3 (2016) 505-513.

[72] M. Preteseille, T. Lenoir, Mechanical Fatigue of a Stabilized/Treated Soil Tested with Uniaxial and Biaxial Flexural Tests, Transportation Research Procedia 14 (2016) 1923-1929.

[73] M. Preteseille, T. Lenoir, Mechanical fatigue behavior in treated/stabilized soils subjected to a uniaxial flexural test, International Journal of Fatigue 77 (2015) 41-49.

[74] M. Preteseille, T. Lenoir, P. Hornych, Sustainable upgrading of fine-grained soils present in the right-of-way of High Speed Rail projects, Construction and Building Materials 44 (2013) 48-53.

[75] M. Preteseille, T. Lenoir, E. Gennesseaux, P. Hornych, Structural test at the laboratory scale for the utilization of stabilized fine-grained soils in the subgrades of High Speed Rail infrastructures: Analytical and numerical aspects, Construction and Building Materials 61 (2014) 164-171.

[76] A.S. Voznesenskii, M.N. Krasilov, Y.O. Kutkin, M.N. Tavostin, Y.V. Osipov, Features of interrelations between acoustic quality factor and strength of rock salt during fatigue cyclic loadings, International Journal of Fatigue 97 (2017) 70-78.

[77] A.S. Voznesenskii, Y.O. Kutkin, M.N. Krasilov, A.A. Komissarov, The influence of the stress state type and scale factor on the relationship between the acoustic quality factor and the residual strength of gypsum rocks in fatigue tests, International Journal of Fatigue 84 (2016)

53-58.

[78] A.S. Voznesenskii, Y.O. Kutkin, M.N. Krasilov, A.A. Komissarov, Predicting fatigue strength of rocks by its interrelation with the acoustic quality factor, International Journal of Fatigue 77 (2015) 194-198.

[79] G.D. Nguyen, C.T. Nguyen, H.H. Bui, V.P. Nguyen, Constitutive modelling of compaction localisation in porous sandstones, International Journal of Rock Mechanics and Mining Sciences 83 (2016) 57-72.

[80] X.S. Liu, J.G. Ning, Y.L. Tan, Q.H. Gu, Damage constitutive model based on energy dissipation for intact rock subjected to cyclic loading, International Journal of Rock Mechanics and Mining Sciences 85 (2016) 27-32.

[81] A. Amorosi, S. Aversa, D. Boldini, A. Laera, M. Valerio Nicotera, Application of a new constitutive model to the analysis of plate load tests in a pyroclastic rock, International Journal of Rock Mechanics and Mining Sciences 78 (2015) 271-282.

[82] A.I. Chemenda, Three-dimensional numerical modeling of hydrostatic tests of porous rocks in a triaxial cell, International Journal of Rock Mechanics and Mining Sciences 76 (2015) 33-43.

[83] A.I. Chemenda, D. Mas, Dependence of rock properties on the Lode angle: Experimental data, constitutive model, and bifurcation analysis, Journal of the Mechanics and Physics of Solids 96 (2016) 477-496.

[84] D. Mas, A.I. Chemenda, An experimentally constrained constitutive model for geomaterials with simple friction–dilatancy relation in brittle to ductile domains, International Journal of Rock Mechanics and Mining Sciences 77 (2015) 257-264.

[85] O. Pourhosseini, M. Shabanimashcool, Development of an elasto-plastic constitutive model for intact rocks, International Journal of Rock Mechanics and Mining Sciences 66 (2014) 1-12.

[86] M.T. Zandarin, E. Alonso, S. Olivella, A constitutive law for rock joints considering the effects of suction and roughness on strength parameters, International Journal of Rock Mechanics and Mining Sciences 60 (2013) 333-344.

[87] H.W. Zhou, C.P. Wang, B.B. Han, Z.Q. Duan, A creep constitutive model for salt rock based on fractional derivatives, International Journal of Rock Mechanics and Mining Sciences 48(1) (2011) 116-121.

[88] V. Navarro, J. Alonso, B. Calvo, J. Sánchez, A constitutive model for porous rock including effects of bond strength degradation and partial saturation, International Journal of Rock Mechanics and Mining Sciences 47(8) (2010) 1330-1338.

[89] C.Y. Zhou, F.X. Zhu, An elasto-plastic damage constitutive model with double yield surfaces for saturated soft rock, International Journal of Rock Mechanics and Mining Sciences 47(3)

(2010) 385-395.

[90] T. Saksala, A. Ibrahimbegovic, Anisotropic viscodamage–viscoplastic consistency constitutive model with a parabolic cap for rocks with brittle and ductile behaviour, International Journal of Rock Mechanics and Mining Sciences 70 (2014) 460-473.

[91] G. Grasselli, P. Egger, Constitutive law for the shear strength of rock joints based on three-dimensional surface parameters, International Journal of Rock Mechanics and Mining Sciences 40(1) (2003) 25-40.

[92] M.C. Weng, F.S. Jeng, Y.M. Hsieh, T.H. Huang, A simple model for stress-induced anisotropic softening of weak sandstones, International Journal of Rock Mechanics and Mining Sciences 45(2) (2008) 155-166.

[93] M.C. Weng, L.S. Tsai, Y.M. Hsieh, F.S. Jeng, An associated elastic–viscoplastic constitutive model for sandstone involving shear-induced volumetric deformation, International Journal of Rock Mechanics and Mining Sciences 47(8) (2010) 1263-1273.

[94] M.C. Weng, L.S. Tsai, C.Y. Liao, F.S. Jeng, Numerical modeling of tunnel excavation in weak sandstone using a time-dependent anisotropic degradation model, Tunnelling and Underground Space Technology 25(4) (2010) 397-406.

[95] M.C. Weng, S.H. Tung, M.H. Shih, Microscopic characteristics of problematic tertiary sandstone as revealed by grain-wide local deformation, International Journal of Rock Mechanics and Mining Sciences 46(7) (2009) 1243-1251.

[96] Z. Zhang, K. Huang, A simple J-integral governed bilinear constitutive relation for simulating fracture propagation in quasi-brittle material, International Journal of Rock Mechanics and Mining Sciences 48(2) (2011) 294-304.

[97] M. Haupt, A constitutive law for rock salt based on creep and relaxation tests, Rock Mechanics and Rock Engineering 24(4) (1991) 179-206.

[98] Z. Zhou, X. Li, Z. Ye, K. Liu, Obtaining Constitutive Relationship for Rate-Dependent Rock in SHPB Tests, Rock Mechanics and Rock Engineering 43(6) (2010) 697-706.

[99] H. Roshan, M. Oeser, A Non-Isothermal Constitutive Model for Chemically Active Elastoplastic Rocks, Rock Mechanics and Rock Engineering 45(3) (2012) 361-374.

[100] Q. Lei, J.-P. Latham, J. Xiang, Implementation of an Empirical Joint Constitutive Model into Finite-Discrete Element Analysis of the Geomechanical Behaviour of Fractured Rocks, Rock Mechanics and Rock Engineering (2016) 1-18.

[101] S.Y. Xie, J.F. Shao, An Experimental Study and Constitutive Modeling of Saturated Porous Rocks, Rock Mechanics and Rock Engineering 48(1) (2015) 223-234.

[102] K. Khaledi, E. Mahmoudi, M. Datcheva, T. Schanz, Stability and serviceability of

underground energy storage caverns in rock salt subjected to mechanical cyclic loading, International Journal of Rock Mechanics and Mining Sciences 86 (2016) 115-131.

[103] L. Blanco-Martín, J. Rutqvist, J.T. Birkholzer, Extension of TOUGH-FLAC to the finite strain framework, Computers & Geosciences.

[104] M. Mánica, E. Ovando, E. Botero, Assessment of damping models in FLAC, Computers and Geotechnics 59 (2014) 12-20.

[105] Y. Yu, I.P. Damians, R.J. Bathurst, Influence of choice of FLAC and PLAXIS interface models on reinforced soil–structure interactions, Computers and Geotechnics 65 (2015) 164-174.

[106] J. Rutqvist, Y. Ijiri, H. Yamamoto, Implementation of the Barcelona Basic Model into TOUGH–FLAC for simulations of the geomechanical behavior of unsaturated soils, Computers & Geosciences 37(6) (2011) 751-762.

[107] H.N. Wang, G.S. Zeng, S. Utili, M.J. Jiang, L. Wu, Analytical solutions of stresses and displacements for deeply buried twin tunnels in viscoelastic rock, International Journal of Rock Mechanics and Mining Sciences 93 (2017) 13-29.

[108] W. Zhang, B. Dai, Z. Liu, C. Zhou, Modeling discontinuous rock mass based on smoothed finite element method, Computers and Geotechnics 79 (2016) 22-30.

[109] V. Bonilla–Sierra, L. Scholtès, F.V. Donzé, M. Elmouttie, DEM analysis of rock bridges and the contribution to rock slope stability in the case of translational sliding failures, International Journal of Rock Mechanics and Mining Sciences 80 (2015) 67-78.

[110] S. Assefa, A. Graziani, A. Lembo-Fazio, A slope movement in a complex rock formation: Deformation measurements and DEM modelling, Engineering Geology.

[111] E. Mohtarami, A. Baghbanan, M. Eftekhari, H. Hashemolhosseini, Investigating of chemical effects on rock fracturing using extended finite element method, Theoretical and Applied Fracture Mechanics.

[112] C. Yan, H. Zheng, A coupled thermo-mechanical model based on the combined finite-discrete element method for simulating thermal cracking of rock, International Journal of Rock Mechanics and Mining Sciences 91 (2017) 170-178.

[113] M. Madadi, M. Saadatfar, A finite-element study of the influence of grain contacts on the elastic properties of unconsolidated sandstones, International Journal of Rock Mechanics and Mining Sciences 93 (2017) 226-233.

[114] S. Fang, L. Cheng, L.F. Ayala, A Coupled Boundary Element and Finite Element Method for the Analysis of Flow Through Fractured Porous Media, Journal of Petroleum Science and Engineering.

[115] Q.-S. Bai, S.-H. Tu, C. Zhang, DEM investigation of the fracture mechanism of rock disc containing hole(s) and its influence on tensile strength, Theoretical and Applied Fracture Mechanics 86, Part B (2016) 197-216.

[116] M. Jiang, T. Jiang, G.B. Crosta, Z. Shi, H. Chen, N. Zhang, Modeling failure of jointed rock slope with two main joint sets using a novel DEM bond contact model, Engineering Geology 193 (2015) 79-96.

[117] L.-j. Ma, X.-y. Liu, M.-y. Wang, H.-f. Xu, R.-p. Hua, P.-x. Fan, S.-r. Jiang, G.-a. Wang, Q.-k. Yi, Experimental investigation of the mechanical properties of rock salt under triaxial cyclic loading, International Journal of Rock Mechanics and Mining Sciences 62 (2013) 34-41.

[118] S. Miao, M.L. Wang, H.L. Schreyer, Constitutive Models for Healing of Materials with Application to Compaction of Crushed Rock Salt, Journal of Engineering Mechanics 121(10) (1995) 1122-1129.

[119] G. Sciarra, F. dell'Isola, K. Hutter, Dilatational and Compacting Behavior around a Cylindrical Cavern Leached Out in a Solid–Fluid Elastic Rock Salt, International Journal of Geomechanics 5(3) (2005) 233-243.

[120] L. Wei, C. Jie, J. Deyi, S. Xilin, L. Yinping, J.J.K. Daemen, Y. Chunhe, Tightness and suitability evaluation of abandoned salt caverns served as hydrocarbon energies storage under adverse geological conditions (AGC), Applied Energy 178 (2016) 703-720.

[121] V. Taupin, S. Berbenni, C. Fressengeas, O. Bouaziz, On particle size effects: An internal length mean field approach using field dislocation mechanics, Acta Materialia 58(16) (2010) 5532-5544.

[122] M.A. Omari, I. Sevostianov, Estimation of changes in the mechanical properties of stainless steel subjected to fatigue loading via electrical resistance monitoring, International Journal of Engineering Science 65 (2013) 40-48.

[123] S.M. Mousavi, M. Lazar, Distributed dislocation technique for cracks based on non-singular dislocations in nonlocal elasticity of Helmholtz type, Engineering Fracture Mechanics 136 (2015) 79-95.

[124] C. Zhou, C. Reichhardt, C.J. Olson Reichhardt, I.J. Beyerlein, Dynamic Phases, Pinning, and Pattern Formation for Driven Dislocation Assemblies, Scientific Reports 5 (2015) 8000.

[125] M. Abdel-Karim, Modified kinematic hardening rules for simulations of ratchetting, International Journal of Plasticity 25(8) (2009) 1560-1587.

[126] M. Abdel-Karim, An evaluation for several kinematic hardening rules on prediction of multiaxial stress-controlled ratchetting, International Journal of Plasticity 26(5) (2010) 711-730.

[127] K. Chung, T. Park, Consistency condition of isotropic–kinematic hardening of anisotropic

yield functions with full isotropic hardening under monotonously proportional loading, International Journal of Plasticity 45 (2013) 61-84.

[128] L. Xu, X. Nie, J. Fan, M. Tao, R. Ding, Cyclic hardening and softening behavior of the low yield point steel BLY160: Experimental response and constitutive modeling, International Journal of Plasticity 78 (2016) 44-63.

[129] D. Barbera, H. Chen, Y. Liu, Creep-fatigue behaviour of aluminum alloy-based metal matrix composite, International Journal of Pressure Vessels and Piping 139-140(3-4) (2016) 159-172.

[130] Kong X, Wang E, Hu S, Shen R, Li X, Zhan T Fractal characteristics and acoustic emission of coal containing methane in triaxial compression failure. Journal of Applied Geophysics. 124(2016): 139-147.

[131] Su F-q, Itakura K-i, Deguchi G, Ohga K Monitoring of coal fracturing in underground coal gasification by acoustic emission techniques. Applied Energy. 189(2017): 142-156.

Appendix

A. Publications

[1] Jinyang Fan, Jie Chen*, Deyi Jiang, Song Ren, Jianxun Wu, Fatigue properties of rock salt subjected to interval cyclic pressure, International Journal of Fatigue, 2016, 90 (9) 109-115.

[2] Deyi Jiang, Jinyang Fan *, Jie Chen, Lin Li, Yao Cui, A mechanism of fatigue in salt under discontinuous cycle loading, International Journal of Rock Mechanics and Mining Sciences, 2016, 86(7): 255.260

[3] Jinyang Fan, Jie Chen*, Deyi Jiang, Song Ren, Junchaochen, Discontinuous cyclic loading test with acoustic emssion monitoring, International Journal of Fatigue, 2017, 91 (1) 140-144

[4] Chen, Jie*; Du, Chao; Deyi Jiang; Jinyang Fan; He, Yi; The mechanical properties of rock salt under cyclic loading-unloading experiments. Geomechanics and Engineering; 2016, 10:3, pp.325.334.

B. Scientific research projects

[1] Study on the mechanism of the construction of [1] energy underground reservoir group and the state key basic research and development plan (973 program, 2009CB724606)，2009.01~2013.12. (Participant)

[2] Multi-layer salt karst cavity construction phase and flow field interaction mechanism research, national natural science foundation project (51074198)，2011.01~2013.12. (Participant)

[3] Study on the interaction mechanism between interlayer and flow field during the construction of multi-layer hydrocarbon reservoir, Basic scientific research program for central university (CDJXS11241182)，2011.03~2012.03. (Participant)

[4] Fatigue life model of salt rock under discontinuous cyclic loading, Chongqing University Postgraduate Innovation Project. CYB16029, 2016.06~2017.06. (Host)

C. Scholarships

[1] 2016 The first prize for science and technology of the ministry of education of the People's Republic of China (no.11)

[2] 2009 National encouragement scholarship.

[3] 2012 National scholarship for postgraduate students.

[4] 2014 National scholarship for postgraduate PhD student.

[5] 2012 Ecelent graduate student at chongqing university in 2012.

[6] 2014, chongqing university, "ten talents at the university" .

D. Practical projects

[1] Convergence deformation and surface settlement mornitoring for Chongqing metro line 1, Yang-lie segment tunnel and station (on-site responsibility);

[2] Convergence deformation and surface settlement monitoring for the Jiefang-bei underground ring road in Chongqing (on-site responsibility);

[3] Slop monitoring and embarkment settlement detection for the special highway of motorway (participant);

[4] Fundation monitoring for the LFC project (participant)；